High Resolution Cardiac Magnetic Resonance Elastography:

From Phantom to Mouse Heart

BY

Yifei Liu
B.S., Donghua University, Shanghai, China, 2002
M.S., University of Illinois at Chicago, Chicago, 2010

THESIS

Submitted as partial fulfillment of the requirements
for the degree of Doctor of Philosophy in Mechanical Engineering
in the Graduate College of the
University of Illinois at Chicago, 2015

Chicago, Illinois

Defense Committee:

Thomas J. Royston, Chair and Advisor
E. Douglas Lewandowski, Center for Cardiovascular Research
Richard L. Magin, Bioengineering Department
Dieter Klatt, Bioengineering Department
Michael Scott, Mechanical and Industrial Engineering

To My beloved mother
To my late father and sister

ACKNOWLEDGMENTS

Over the past five years of my Ph.D. study, I have received numerous support and encouragement from a lot of people. First and foremost, I would like to express my deepest gratitude to my advisor, Dr. Thomas J. Royston, for his mentoring and guidance. His encouragement and support helped me accomplish every stage of the dissertation process. I was also fortunate to have Dr. Richard L. Magin as a professor and committee member who introduced me to the magic world of MRI. And a deepest appreciation to Dr. Dieter Klatt for his valuable insights and instructive comments in my MR Elastography research. I'm particularly grateful to Dr. E. Douglas Lewandowski for his support and guidance in my research of implementation of MRE on the mouse heart. His advice from the perspective of a cardiovascular disease research scientist helped me, a student majoring in mechanical engineering, to better understand the heart and to achieve the goal of cardiac MRE implementation efficiently. I also want to acknowledge the other committee member of my dissertation, Dr. Michael J. Scott, for his help in these years.

Also, I would like to extend my gratitude to Dr. Robert Kleps and Dr. Weiguo Li for their assistance with the MR scanner for my experiments, to Eric Schmidt and David Mecha for realizing my experiment setup designs. And my sincere appreciation to Dr. Temel K. Yasar, who did innumerable contributions to the implementation of MRE at UIC, and to Dr. Ziying Yin who helped me so much in the practice of MR Imaging.

I would like to give my special thanks to my colleagues, Steven Kearney, Altaf Khan, Zoujun Dai, Ying Peng, Spencer Brinker, Allen Ye, Benjamin Schwartz, Brian Henry, Harish R. Palnitkar, and others, for their invaluable help, ideas, and friendship.

Finally, I want to thank my family, to my late father and my late sister whose optimism in fighting with diseases encouraged me to devote myself in researches that benefits the improvement of medicine from a mechanical engineer's angle; to my dear mother for her endless love, patience

and support which helped me overcome all the difficulties in my life, especially in the past seven years of graduate study.

YL

In this dissertation, portions of Chapter 3 have been published previously in IOP Publishing (doi:10.1088/0031-9155/59/24/7717). A portion of Chapter 4 has been published previously in ASME publications (doi:10.1115/IMECE2013-63355). Portions of Chapter 6 are under review in John Wiley and Sons publications.

TABLE OF CONTENTS (continued)

CHAPTER PAGE

TABLE OF CONTENTS (continued)

TABLE OF CONTENTS (continued)

LIST OF TABLES

LIST OF FIGURES

LIST OF FIGURES (continued)

LIST OF FIGURES (continued)

LIST OF FIGURES (continued)

LIST OF FIGURES (continued)

LIST OF ABBREVIATIONS

AAR	Area At Risk
AIC	Akaike Information Criterion
ACC	Animal Care Committee
AIDE	Algebraic Inversion of Differential Equation
AON	Area Of Necrosis
CVD	CardioVascular Disease
DI	Direct Inversion
ED	End of Diastole
ES	End of Systole
FA	Flip Angle
FE	Finite Element
FFT	Fast Fourier Transform
FID	Free Induction Decay
FOV	Field Of View
LFE	Local Frequency Estimation
LV	Left Ventricle
MEG	Motion-Encoding Gradient
MI	Myocardium Infarction
MR	Magnetic Resonance
MRE	Magnetic Resonance Elastography
MRI	Magnetic Resonance Imaging
MSG	Motion-Sensitizing Gradient
RF	Radio Frequency
ROI	Region Of Interest

LIST OF ABBREVIATIONS (continued)

SE	Spin Echo
SDP	Selective spectral Displacement Projection
SLIM	SampLe Interval Modulation
SNR	Signal-to-Noise Ratio
TE	Echo Time
TR	Repetition Time
TTC	TriphenylteTrazolium Chloride
ULTIMAte	Unified Sampling Time Interval Modulation
μMRE	Microscopic scale Magnetic Resonance Elastography
WAV	Wave Amplitude Variance

SUMMARY

First proposed in 1995, magnetic resonance elastography (MRE) has attracted more and more attention with its capability of estimating soft tissue stiffness non-invasively. In addition to the FDA-certified application for hepatic disease diagnosis, MRE has been studied in multiple organs as a potential new biomarker in various disease diagnoses, especially in recent years. Beside the application to disease diagnosis, MRE has also been utilized in monitoring the development of engineered tissue and in more fundamental studies of tissue viscoelasticity.

This dissertation aims to advance the application of high field MRE on complex anatomical structures, beginning with phantom studies progressing to, arguably, the most complex application yet attempted, cardiac MRE *in vivo* on a mouse model to assess myocardial stiffness in healthy and pathological subjects. Prior to attempting in vivo cardiac MRE on the mouse model, several pilot studies were conducted on phantom models to advance the technique.

A wideband phantom study was conducted to improve viscoelastic model identification. In order to better understand mechanical wave motion in geometry similar to the left ventricle, MRE experiments on a liquid-filled spherical shell phantom embedded in a soft tissue mimicking material were also conducted. Computational finite element simulations on a three dimensional model of a mouse with different actuation methods were also performed to improve understanding of how mechanical waves propagate into the complicated geometry of the mouse body, and how the tissue responds under different actuation approaches. An *in vivo* mouse cardiac MRE technique was then developed and tested on a healthy mouse model. This technique is able to track expected stiffness changes in the myocardium as a function of the cardiac cycle. And the results showed the feasibility of this implementation of in vivo cardiac MRE on mice. A follow-up study of applying the cardiac MRE on a Myocardial Infarcted (MI) mouse model was then conducted to assess the ability to noninvasively quantify expected changes in the myocardial mechanical properties of these animals, relative to the healthy cases.

1. INTRODUCTION

1.1 Background and Motivation

Small animal models, such as the mouse, are widely involved in biomedical research. As a common mechanical property, shear stiffness is however not that easy to estimate in most of these models because of their nearly incompressible feature (very high bulk versus shear mechanical properties) and their small dimension. With a high field MR scanner and a powerful gradient, high resolution MRE at the microscopic scale (μMRE) can be achieved so that small dimensional objects can be studied [1]. Therefore, high resolution MRE provides a promising method to assess the stiffness in small animal models, and offers more possibilities in theoretical study and pathology research.

1.1.1. Magnetic Resonance Elastography as a Diagnostic Tool

Stiffness change in an organ is correlated with severity of disease in many cases. For instance, benign lesions tend to be stiffer than normal breast tissue but softer than cancerous tumors [2]. The elasticity of the soft tissue can be quantitatively imaged by measuring the tissue response under applied stress. Elasticity imaging methods includes optical, mechanical, ultrasound and MRI. One of the early works in elastic imaging is to use visible light to measure mechanical wave propagation and thus determine the tissue viscoelasticity [3]. Ultrasound imaging has been widely used in elasticity imaging, and the term "elastography", describing the elasticity imaging, was first used in 1991 in relation to ultrasound elastography [4]. The MRI technique has been implemented to measure tissue motion since the 1980's; one early implementation is to use MR tagging to assess cardiac function [5, 6]. Another MR technique based on synchronized actuation and motion encoding gradients (MEG) was proposed [7] and developed as a new technique named MR Elastography (MRE) [8] in 1995. MRE uses harmonic vibration as actuation, and a phase-contrast MRI technique to map and measure the strain pattern of a tissue-like material under the harmonic

vibration spatially, and obtains a stiffness map from this displacement pattern with a suitable inversion algorithm [9]. Tissue stiffness can be estimated by the local frequency estimation (LFE) method by measuring the wave length from the wave pattern [10]. By adjusting the phase difference between the mechanical actuation and the MEG, the full harmonic motion can be sampled and reconstructed, and the viscoelastic properties can be estimated by using the direct inversion algorithm [9, 11]. MRE has been used for clinical research on various organs and disease diagnoses, such as hepatic diseases [12, 13], breast cancer [14], skeletal muscle [15, 16], brain [17-19], lung [20, 21], the eye globe [22, 23], and heart [24, 25], etc.

1.1.2. Stiffness of Left Ventricle in Heart Failure:

Unlike other organs, the heart is unique because it beats all the time to pump blood through the circulatory system. The operative filling pressure and volume of the heart chamber change during each cardiac cycle causing stiffness changes in the heart wall, correspondingly. The mechanical properties of the heart are a significant factor in the contractility of the heart. Chamber stiffness and myocardial stiffness are two mechanical properties relevant to the systolic and diastolic function. Chamber stiffness is the behavior of the chamber, which is the diastolic property of a ventricle defining distensibility characteristics of a chamber, and is unrelated to the wall thickness. Myocardial stiffness, on the other hand, is the behavior of the muscle in the chamber walls and is an intrinsic property of the myocardium, which can be estimated by myocardial stress-strain properties. [26, 27]. Chamber stiffness has been shown to be related to the myocardial stiffness and the ratio of V/V_w, where V is chamber volume and V_w is the left ventricle wall volume [28, 29]. It is widely accepted that, during the progression of cardiomyopathies to overt heart failure, increased stiffness of the left ventricle (LV) wall is a contributing factor to the abnormal function associated with both impaired systolic and diastolic function, including cardiac fibrosis [30], steatosis [31], and altered sarcomere activity and tension [32, 33].

The primary method to evaluate the chamber stiffness as well as assessment of left ventricular systolic and diastolic pump properties *in vivo* is to estimate the diastolic pressure-volume relation with an invasive method of pressure-volume (P-V) analysis [29, 34]. Another widely utilized non-invasive method in estimating the cardiac function is to use the MR tagging technique, which tracks the motion of the heart and examines the left ventricle contractility by measuring the strain during the cardiac cycle [5, 35, 36]. A novel *ex vivo* method using atomic force microscopy nanoindentation was also proposed in recent years [31].

1.1.3. Cardiac Imaging

There are several non-invasive cardiac imaging techniques in diagnostic purposes, includes coronary catheterization, stress echocardiography, CT angiography, nuclear cardiology, and MRI.

1.1.3.1. Coronary Catheterization / Angiography

As mentioned in section 1.1.2, coronary catheterization is the primary method to evaluate the chamber stiffness. In this method, a catheter is inserted into the heart through blood vessels in the leg. Pressure monitoring and blooding sampling were then performed via the catheter. In addition, the position and volume of blood within the heart chambers and arteries can be obtained by a following injection of radiocontrast dye through the catheter, and using X-ray fluoroscopy to estimate [37].

1.1.3.2. Echocardiogram

Echocardiogram uses ultrasonic wave for continuous visualization of the heart chamber and blood movement with Doppler technique. This is the one of the most commonly used approached in cardiovascular disease diagnosis. It is a functional imaging method and can be used in two cardiac function assessment. It can be used for systolic function assessment by observing the wall motion abnormalities, which is indicative of cardiovascular disease. And by using contrast agent during the echocardiogram, it can also be used to assess the myocardial perfusion. Using the contrast agent makes the microbubbles remain in the vascular space until dissolved, which reflects

the microvascular circulation. And the signal intensity indicates the relative concentration of the microbubbles in different regions of the myocardium, and thus reflects the relative myocardial blood volume in these region [38, 39].

1.1.3.3. Computed Tomography (CCTA)

With the fast development of computed tomography (CT) technology, the advantage of fast acquisition and high resolution of CT accelerate the usage of CT in cardiology as well. There mainly two types of CT scans in cardiology, calcium-score screening heart scan and coronary CT angiography. CT is an effect way to detect calcium remain, and using calcium-score screening with CT can detect calcium deposits found in atherosclerotic plaque in coronary arteries, which is an indicator of the risk of future coronary artery disease. Coronary CT angiography (CCTA) uses intravenous injection of contrast to obtain high resolution, three dimensional images of the moving heart to determine the fat and calcium deposits. And the whole body CT scan helps to identify potential problems or disease [40, 41].

1.1.3.4. Cardiac Nuclear Imaging

Cardiac nuclear imaging includes Single Photon Emission Computed Tomography (SPECT) and cardiac Positron Emission tomography (PET). Similar to conventional nuclear medicine planar imaging, SPECT uses gamma rays but is able to provide 3D information. It is commonly used for nuclear cardiology procedure. Different from SPECT, PET detects pairs of gamma rays which were emitted indirectly by a positron-emitting radionuclide. So that PET can provide three-dimensional images of radionuclide concentration within the body. The nuclear images enable visual image analysis of multiple different metabolic chemical processes and can be used to assess the perfusion. On the other hand, by using the ECG gated SPECT, the global and regional LV function can be assessed in addition to perfusion. By comparing the gated SPECT with MRI or echocardiography, the correlations of LV ejection fraction, volume, and regional wall motion can be estimated. [38, 42, 43] .

1.1.3.5. Magnetic Resonance Imaging (MRI)

With the advantage of differentiates the soft tissue better than CT, MRI in cardiology is growing. Currently, the implementation of MRI in cardiology has limitation on lengthy scanning time and restriction on some metallic implants such as pacemakers. Also, the continuous movement of the heart can reduce the image quality. However, since by manipulating with different MRI sequence, multiple functions can be achieved with MRI in cardiac image. The cardiac MRI has a promising future. Typical application of MRI in cardiac imaging includes assessment of perfusion, non-invasive angiography, and systolic function assessment [38, 44]. The cardiac MRE technique introduced in this dissertation is one of the application of MRI in cardiac image.

1.1.4. Existing Cardiac MRE Implementation on Human and Large Animal Model

Implementing MRE on the heart provides an alternative for assessing the left ventricle function by stiffness estimation temporally and non-invasively. Researchers have studied the implementation of MRE for assessing heart wall stiffness in humans and porcine models. Two major MRE groups initiated studies in 2008 and 2009 with different methods.

1.1.4.1. Cardiac MRE Studies with Conventional MRE Concept (WI-MRE):

In 2009, researchers at the Mayo clinic published a study on a heart-simulating phantom [45], with an acoustic driver developed for human and large animal studies, a multi-phase MRE sequence [46] and an inversion method specifically for shell geometry [47]. *In vivo* and invasive studies with multiple driving methods [48] and *in vivo* non-invasive studies under different loading conditions with improved inversion processing [49] were conducted on a porcine model and, as one would expect, estimated heart wall stiffness variation throughout the cardiac cycle correlated with heart pressure variation, with a maximum near end-systole and minimum near end-diastole. More in vivo experiments were conducted in porcine and human subjects with different inversion algorithms, including the phase gradient [50] and LFE algorithms [51].

1.1.4.2. Cardiac MRE studies with wave amplitude variances (WAV-MRE):

Instead of using the conventional MRE concept that converts wave images into a stiffness map, the MRE group in Charité-Universitätsmediz in Berlin developed an alternative approach in 2008, which is specifically suitable to the heart, with its cyclic temporal stiffness change behavior. This Wave Amplitude Variance (WAV) method is based on the estimated relation between shear stiffness and wave amplitude at different time points, as given by $\frac{\mu(t_1)}{\mu(t_2)} = \left(\frac{U(t_2)}{U(t_1)}\right)^4$, where $\mu(t_1)$, $\mu(t_2)$ and $U(t_1)$ and $U(t_2)$ are the shear stiffness and wave amplitude at different time point of t_1 and t_2. Thus, instead of giving a stiffness value, this method gives a ratio of stiffness at end-systole and end-diastole. Continuous acquisitions covering multiple cardiac cycles were performed to capture multiple vibration cycles, and a plot of displacement amplitude in the time domain could be drawn. A correlation of displacement and cardiac stage of diastole or systole need to be derived in this method to identify the valid vibration affected ROI [25, 52]. The experiments were done in vivo and noninvasively on human subjects, and show a difference between young volunteers (20-35 yrs.), senior volunteers (50-60 yrs.) and patients with relaxation abnormalities [53].

1.2 Objectives of This Study

This dissertation has the ultimate goal to apply MRE on an *in vivo* mouse heart model. As a common animal model for studying the heart failure processes, the dimension of the mouse heart is usually less than 10 mm in all dimensions. With cardiac MRE, one can monitor the myocardial stiffness change during the cardiac cycle, and discover the stiffness ratio difference between the healthy and pressure overloaded mouse heart. In order to achieve these goals and to push MRE to its limits on a few fronts, pilot studies addressing the following aims are undertaken:

Aim 1: Use MRE to study the viscoelastic properties of tissue-like material over a wider frequency range than has been done before to quantify the appropriateness of different proposed viscoelastic models;

Aim 2: Use MRE to study the wave propagation behavior in a shell geometry model similar to the left ventricle;

Aim 3: Study wave propagation behavior in the complex geometry of the mouse using a 3-dimensional computational finite element (FE) simulation model under different actuation conditions;

Aim 4: Develop and test an experimental system for murine cardiac MRE, which includes:

- *Aim 4.1:* efficiently introducing harmonic mechanical wave motion into the mouse body;
- *Aim 4.2:* developing MRE pulse sequences on a 9.4 Tesla Agilent MRI system for MRE experiments, in order to encode vibratory motion in the mouse heart at different phases of the cardiac cycle;
- *Aim 4.3:* developing Matlab software to post-process the MRE experimental data, including converting the displacement data to stiffness maps using several different inversion algorithms; and

Aim 5: Assess whether developed *in vivo* cardiac MRE can differentiate normal and pathological models of heart disease that are expected to cause differences in myocardial stiffness.

1.3 Structure of the Dissertation

The chapter-wise organization of this dissertation is as follows:

Chapter 2 starts with the basics of magnetic resonance imaging involved in this study, and then introduces the fundamentals of magnetic resonance elastography (MRE), including the theory and the three components in MRE: excitation, motion encoding and data interpreting.

Chapter 3 presents the study of aim 1 in this dissertation: ultra-wideband MR Elastography for robust shear viscoelasticity model identification [54] This is an extended study of a previous article [55], covering a wider band of frequency and smaller size phantom than has ever been considered previously by anyone to the best of our knowledge. More viscoelastic model types are compared than have been compared in previous studies.

Chapter 4 presents the study of the aim 2 in this dissertation: study the wave propagation in a shell geometry phantom model. This study is meant to mimic the geometry of the left ventricle, a spherical shell with fluid inside, and examine how waves propagate in such a spherical geometry.

Chapter 5 is a finite element study of wave propagation in a computational mouse model conducted to examine how waves propagate in the complicated biological geometry, and thus test the feasibility of cardiac MRE and to optimize a vibratory actuator design prior to the costly in vivo experiment.

Chapter 6 introduces the method of cardiac MRE on the mouse model, including experiment setup, pulse sequence and post processing method. And initial results of this implementation on a healthy mouse model are also given in this chapter.

Chapter 7 shows further results of applying cardiac MRE on a myocardial infarction mouse model and a sham mouse model.

Chapter 8 provides a summary of the projects, highlighting original contributions, analyzing the limitations of the current study, and looking forward to the future study directions.

2. MAGNETIC RESONANCE ELASTOGRAPHY

Magnetic Resonance Elastography (MRE), as a diagnostic imaging technique in quantitatively assessing the mechanical properties of soft tissue, is developed based on the MRI technique. This chapter starts from the theory of Magnetic Resonance Imaging (MRI), and follows with a comprehensive introduction of MRE, including a review of the existing inversion algorithms in stiffness reconstruction in MRE.

2.1 Magnetic Resonance Imaging

2.1.1. Concepts of Magnetic Resonance

Magnetic Resonance (MR) is based on the interaction between applied magnetic fields and nuclei that process spin. An intrinsic property of the nucleus is *spin* or *spin angular momentum* that he nucleus can be considered to be rotating about an axis at a constant rate of velocity. And, only a nucleus with an odd atomic weight and/or odd atomic number, which has non-zero *spin (*or *nuclear spin quantum number) I*, interacts with an external magnetic field and can be studied using MR. For ^{1}H, ^{13}C, ^{19}F, and ^{31}P nuclei, it's *spin* $I = \frac{1}{2}$. A spin system in this case is called a spin $-\frac{1}{2}$ system [56]. For MRI, the hydrogen nucleus, or proton, is the most important nucleus, because of its abundance in various soft tissues and organs.

If the spinning nucleus is positively charged, it creates a local magnetic field around it, which is called *nuclear magnetic dipole moment* or *magnetic moment*. When a proton is placed in a strong external magnetic field B_0, this external magnetic field attempts to align the nucleus magnetic moment parallel to the direction of B_0. This action creates a torque that force the nucleus to precess around the axis of B_0 [56, 57], shown in Figure 2-1a.

In general, MR measures collections of similar spins rather than an individual spin. Consider a collection of hydrogen protons in an arbitrary volume of tissue. Each proton has a spin vector of equal magnitude. The summation of the spin vector is defined as *net magnetization*. And,

MR is based on manipulating this *net magnetization* $\boldsymbol{M_0}$ [57]. Generally, the spin vectors for the entire protons collection within the tissue are oriented randomly in all directions which causes a zero sum of all of these spin vectors, meaning no net magnetization is observed in the tissue (Figure 2-1b). When exposing this piece of tissue in an external magnetic field $\boldsymbol{B_0}$, each proton begins to precess about the magnetic field. The rate or frequency of precession is expressed by the **Larmor equation** shown in Equation 2-1:

$$\omega_0 = \gamma B_0 \qquad [2\text{-}1]$$

where ω_0 is the *Lamor frequency* in MHz, $\mathbf{B_0}$ is the external magnetic field strength in Tesla (T) and γ is a constant called the *gyromagnetic ratio* for each nucleus in MHz/T; it is 42.67 MHz/T for ^{1}H proton. The net magnetization only has a z component because the vector sum of the components in x and y axis is averaged to zero, shown in Figure 2-1c.

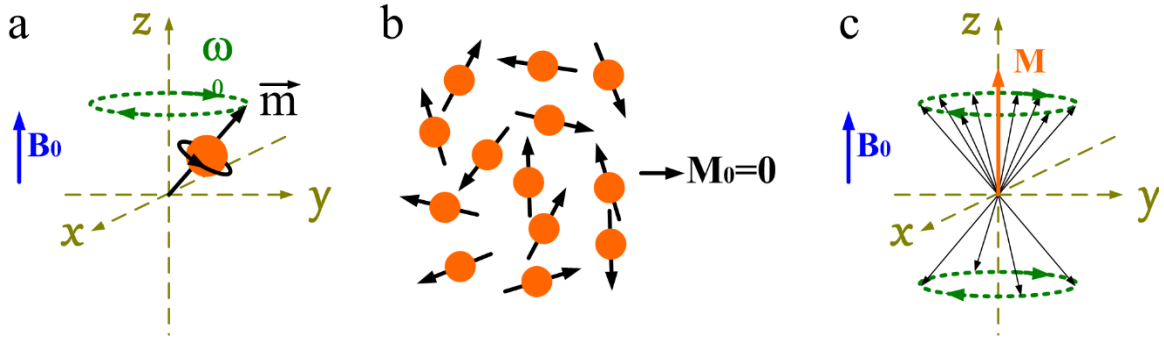

Figure 2-1 (a) Precession of a proton about an axis parallel to the direction of the main magnetic field B_0; (b) Summation of the spin vector of a collection of protons $\boldsymbol{M_0}$ is 0 when the spins are randomly oriented in all directions; (c) A thermal equilibrium of magnetization in the main magnetic field B_0.

In brief, the MR experiment can be considered as an energy transfer: the sample absorbs energy at the correct frequency; the energy is re-emitted after a short time and is then detected and processed. In order to obtain an MR signal, transitions needs to be induced by an energy exchange between the protons in the parallel and anti-parallel energy levels [58]. The required energy is supplied by an oscillating magnetic field denoted as $\boldsymbol{B_1}(t)$, which is short-lived and oscillates in the range of radio-frequency ω_{rf} and thus is called an RF pulse. When it is irradiated with the energy at a correct frequency, a proton at lower energy (parallel) level will absorb a certain amount quantum of energy and be excited to a higher energy (anti-parallel) level, and a proton at a higher energy level will be stimulated to release its energy and go to the lower energy level. The spin in different orientations (energy levels) has different energy of interaction with the external magnetic field B_0:

$$E = -\gamma\hbar m_I B_0 \qquad [2\text{-}2]$$

where $\hbar$ is Plank's constant h (6.6×10^{-34} J-s) divided by 2π, m_I is the *magnetic quantum number*, and is $\frac{1}{2}$ at parallel orientation and is $-\frac{1}{2}$ at anti-parallel orientation for a spin $-\frac{1}{2}$ system.

The correct frequency of the energy that can achieve this excitation has a relation with the energy difference between the two energy levels as follows:

$$\hbar\omega_{\mathrm{rf}} = \Delta E = \frac{1}{2}\gamma\hbar\mathrm{B}_0 + \frac{1}{2}\gamma\hbar\mathrm{B}_0 \qquad [2\text{-}3]$$

from Equation 2-1, it can be derived:

$$\omega_{rf} = \omega_0 \qquad [2\text{-}4]$$

This quantized energy absorption is known as *resonance absorption*, Equation 2-4 is known as *resonance condition*, and this correct frequency is known as the *resonance frequency* [56, 57].

For a collection of protons in a volume of tissue, there are more protons at the lower energy level and so they have a net absorption of energy by the tissue during the RF pulse. When applying the oscillating magnetic field $\boldsymbol{B_1}$, or RF pulse, perpendicular to the main magnetic field $\boldsymbol{B_0}$, absorption of the RF energy of the resonance frequency cause the net magnetization $\boldsymbol{M}$ to rotate away from its equilibrium orientation to a new orientation that perpendicular to both $\boldsymbol{B_0}$ and $\boldsymbol{B_1}$ follows a right-hand rule [59]. If the transmitter is left on long enough time and at a high enough amplitude, $\boldsymbol{M_0}$ can be rotated entirely into the transverse plane and is called 90° pulse. In order to simplify this rotation, a rotating reference frame whose coordinate system is rotating at the Lamor frequency would be considered, and the motion of $\boldsymbol{M_0}$ in this reference frame is a simple vector rotation. This rotating reference frame will be used as the basis for all future discussion in this dissertation.

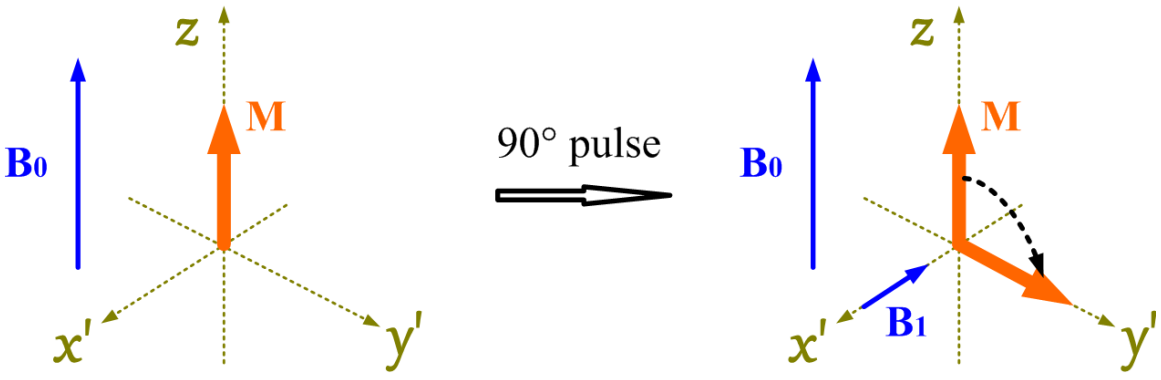

Figure 2-2: Application of B_1 field along x-axis rotates the magnetization towards y-axis following a right-hand rule in the rotating frame.

After the transmitter turned off, the protons begin to realign themselves to the original equilibrium state at their lowest energy state, and emit energy at frequency of ω_0 during this process. If a receiver coil, a loop of wire, is placed perpendicular to the transverse plane, the realigning protons induce a voltage, or MR signal, in the wire during their precession. The time-domain MR signal is collectively referred to as the free induction decay (FID), has an initial magnitude that depends on the value of $\boldsymbol{M_0}$ immediately prior to the 90° pulse. The FID decays with time when more protons give up their absorbed energy through a process called "relaxation", and the coherence of the protons motion is lost during relaxation [57].

2.1.2. Bloch Equation and Relaxation

As mentioned above, the spins are disturbed from their equilibrium states by the excitation of the RF pulse and relax back to the equilibrium states through a process called "relaxation" after the RF transmitter is turned off. The time evolution of the magnetization $\boldsymbol{M}$ is characterized by a differential equation called Bloch equation [56]:

$$\frac{dM}{dt} = M \times \gamma B - \frac{M_x i + M_y j}{T_2} - \frac{(M_z - M_0)k}{T_1} \qquad [2\text{-}5]$$

where M_0 is the magnetization at equilibrium in the presence of B_0 only, B is the applied magnetic field that comprises the static B_0 field and the RF B_1 field, $\hat{\imath}$, $\hat{\jmath}$ and $\hat{k}$ are the unit vectors in the Cartesian coordinate system, and T_1 and T_2 are two time constants that characterize the "relaxation". So the time evolution of the components M_x, M_y and M_z can be rewritten as [58]:

$$\frac{dM_x}{dt} = \gamma M_y \left(B_0 - \frac{\omega}{\gamma}\right) - \frac{M_x}{T_2}$$

$$\frac{dM_y}{dt} = \gamma M_z B_1 - \gamma M_x \left(B_0 - \frac{\omega}{\gamma}\right) - \frac{M_y}{T_2} \qquad \textbf{\textit{[2-6]}}$$

$$\frac{dM_z}{dt} = -\gamma M_y B_1 - \frac{M_z - M_0}{T_1}$$

T_1 is the time required for the z component M_z to return to 63% of M_0, and is also known as the longitudinal relaxation or "spin-lattice" relaxation time because it involves the protons losing their energy to the surrounding lattice. T_2 is the relaxation time required for the transverse component of M to decay to 37% of M_0 via irreversible processes, which is also known as transverse relaxation time or "spin-spin" relaxation time because it involves the loss of "phase coherence" between the protons precessing in the transverse plane. Both of the values of T_1 and T_2 depend on the magnetic field strength [57]. T_2 is much shorter than T_1, and is much shorter for solids than liquid for most of tissues. And the contrast of MR is based on the difference between T_1 and T_2 in different tissues.

Immediately after an RF pulse of arbitrary tip angle α applied along the x axis, the M_z component is given by $M_0 cos\alpha$, and M_z has a time dependent function after the RF pulse given by:

$$M_z(t) = M_0 cos\alpha + (M_0 - M_0 cos\alpha)(1 - e^{-\frac{t}{T1}}) \qquad [2\text{-}7]$$

No M_x components immediately after the RF pulse, and M_y component is given by $M_0 sin\alpha$, and has a time dependent function as:

$$M_y(t) = M_0 sin\alpha \, e^{-\frac{t}{T_2}} \qquad \textbf{[2-8]}$$

2.1.3. Magnetic Resonance Imaging

As mentioned above, when exposed in an external magnetic field B_0, the proton precesses about the axis parallel to the direction of B_0 at the Larmor frequency. In order to obtain an MR image, which requires spatial information in two dimensions or three dimensions, three physical gradients are needed to be applied on three orthogonal directions or so called: slice selection,

readout or frequency encoding and phase encoding. The presence of gradient magnetic field results in an expanded version of the Larmor equation:

$$\omega_1 = \gamma(B_0 + G \cdot r_i) \quad [2\text{-}9]$$

where ω_i is the frequency of the proton at position r_i and G (usually in unit of mT/m or Gauss/cm) is a vector representing the total gradient amplitude and direction.

Slice selection is accomplished through using a frequency-selective RF pulse simultaneously with a gradient known as the slice selection gradient (G_{ss}). The slice orientation is determined by the gradient direction. The gradient amplitude and the certain RF pulse characteristics determine both the slice thickness and slice position, which associated by two factors: a central frequency ω_s and a narrow bandwidth of frequency $\pm\Delta\omega_s$. The particular location excited is determined by the central frequency of the pulse when the slice selection gradient is present. And the slice thickness (th) is determined by the frequency bandwidth $2\Delta\omega_s$ and the amplitude of the selection gradient G_{ss} [58]:

$$th = \frac{2\Delta\omega_s}{\gamma G_{ss}} \quad [2\text{-}10]$$

From the properties of the Fourier transform, a longer RF pulse results a narrower frequency bandwidth and so that a thinner slice for a given value of G_{ss} [58]. Typically, the duration of the RF pulse is fixed so that the bandwidth. Therefore, slice thickness is determined by G_{ss}, and larger G_{ss} is required for thinner slices [57]; see Figure 2-3. And, by changing the central frequency ω_s of the RF pulse, the slice can be moved to different location of the object. Multislice imaging can be achieved by using the same G_{ss} but a unique RF pulse during excitation with a different central frequency for each slice (Figure 2-3). In multislice imaging, the time of the selected slice

undergoing T_1 relaxation during the time TR-TE can be used to acquire images from adjacent slices; thus, the maximum number of slices is limited by the ratio of TR/TE [58].

After the slice is selected, the MR signal from the other two dimensions must be encoded to create a two-dimensional image, which differentiates MRI from MR spectroscopy. Signal from one direction is encoded by creating a spatially dependent precessional frequency during signal acquisition, which is called frequency or readout encoding. And the other direction is encoded by applying a spatially dependent phase on the precessing protons, which is so called phase encoding.

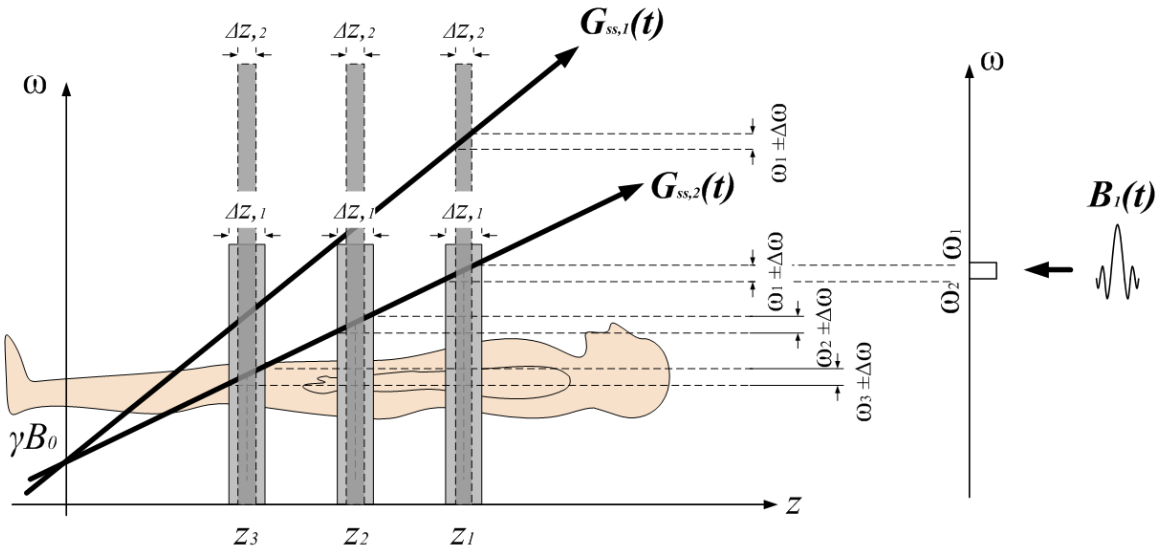

Figure 2-3: Slice selection process and illustration of different gradient strengths maps different slice thicknesses under the same bandwidth.

In readout or frequency encoding, a linear gradient field G_{ro} is turned on during data acquisition. The protons begin to precess at different frequencies depending on their

position along this direction under the influence of this frequency encoding gradient, where each of these frequencies is super imposed into the echo. The echo signal can be measured by the receiver coil. The signal is then be digitized for furture Fourier transformation. There are several factors determines the magnitude of G_{ro}: FOV_{ro} and the Nyquist frequency ω_{NQ}, which is referred to the receiver bandwidth. This relationship can be expressed as [57]:

$$\Delta\omega_{RO} = 2\omega_{NQ} = \gamma\Delta(G_{RO}FOV_{RO}) \quad [2\text{-}11]$$

where $\Delta\omega_{RO}$ is the frequency range in the image. G_{RO} is chosen so that the protons located at the edge of FOV_{RO} precess at the Nyquist frequency for the image.

In phase encoding, a gradient turned on and off before the data acquisition begins, so that a number of different values, N_{pe}, of this phase-encoding gradient G_{pe} muse be used. Thus the total scanning time is proportional to the number N_{pe}. Phase encoding gradient G_{pe} is perpendicular to both G_{ss} and G_{RO}. Phase encoding gradient is the only gradient that changes amplitude during the data acquisition loop. The spatial dependent phase shift $\Delta\phi$ in phase encoding has a relationship with the phase encoding gradient power G_{PE} and the duration τ_{PE} as [56]:

$$\Delta\phi = \Delta\omega_{PE}\tau_{PE} = 2N_{PE}G_{PE}FOV_{PE}\tau_{PE} \quad [2\text{-}12]$$

where N_{PE} is the number of phase encoding steps, FOV_{PE} is the field of view in the phase encoding direction.

After applying the phase-encoding gradient G_{pe} for a period τ_{pe} by turning on and off the gradient before the data acquisition begins, the proton precession returns to its

original frequency before G_{pe} was turned on, but away from the same phase at its previous state. The phase shift amount is determined by three factors: the magnitude and duration of G_{pe} and the location of the proton. The information of the MR image can be obtained by repeating the slice excitation and signal detection for N_p times with a different amplitude of G_{pe} for each time [57].

2.1.4. Basic Pulse Sequence

A pulse sequence is a sequence of commands controlling the hardware of the MR scanner such as RF pulse, gradient and receiver etc., by which the MR image can be obtained. All of these sequences are based on either spin-echo or gradient-echo data acquisition. The spin echo sequence, shown in Figure 2-4, is a commonly used pulse sequence, which has at least two RF pulses: an excitation pulse and one or more $180°$ refocusing pulse that generate the spin echo(es). The gradient pulse in the readout direction has an opposite polarity as the gradient in the slice selection direction in order to refocus the protons at the same time as the spin echo.

The gradient echo sequence is another commonly used pulse sequence which does not use a refocusing $180°$ pulse, as in Figure 2-5. The echo signal is generated only through the gradient reversal. The rephasing of protons and echo signal is accomplished by applying a second gradient pulse of the same duration and magnitude but opposite polarity in at least two directions: the slice selection and the readout direction. The advantage of using gradient echo sequence is several fold: the sequence kernel time may be shorter than for an analogous spin echo sequence; the total RF energy deposition is lower because less total RF power is applied to the patient, etc. However, it also suffers from the disadvantage of loss of signal from static magnetic field inhomogeneity.

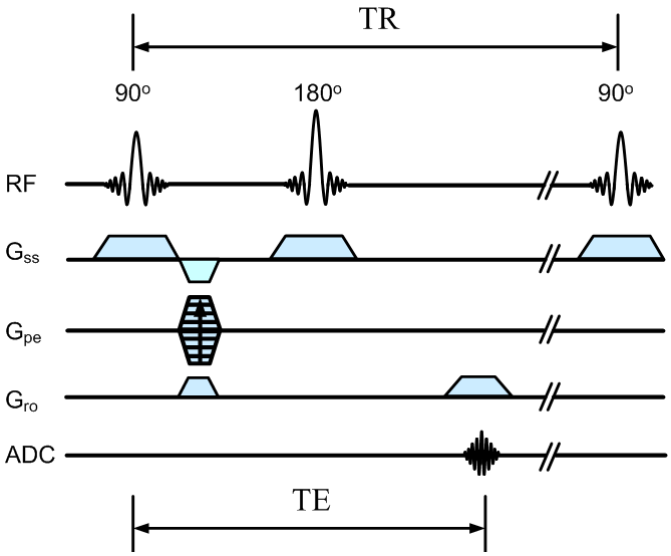

Figure 2-4: The basic spin-echo imaging sequence. A single 180 degree refocusing pulse features this sequence. And in this basic spin echo, only one single detected echo, and one single phase-encoding table is presented. The echo time TE is measured from the middle of the RF pulse to the center of the echo.

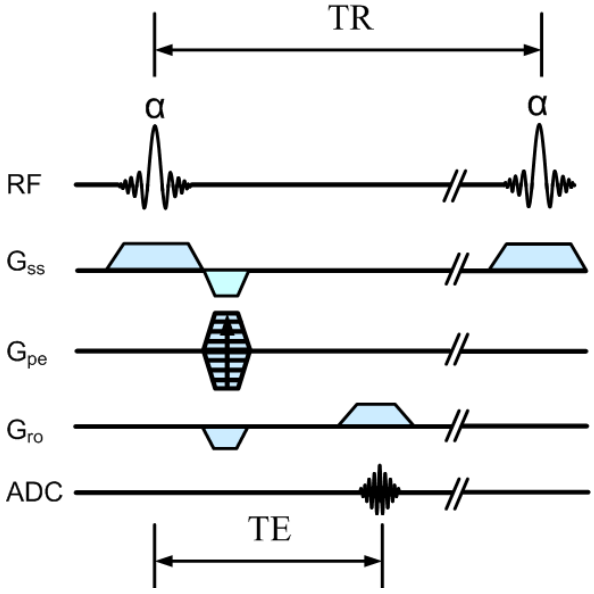

Figure 2-5: The typical gradient echo sequence. The polarity of the G_{ro} dephasing gradient pulse. The polarity of the G_{ro} is opposite to that of the G_{ro} pulse applied during signal detection.

2.2 High Resolution Magnetic Resonance Elastography

2.2.1. Introduction of High Resolution Magnetic Resonance Elastography

Magnetic resonance elastography is an emerging technology for quantitatively estimating the mechanical properties of viscoelastic material such as soft tissue. This technology obtains a stiffness map of the scanned object by mapping the propagation of mechanical waves through the object by a special magnetic resonance imaging technique, which is based on phase-contrast imaging. Therefore, there are three essential components in a successful implementation of MRE: 1) an actuation source that can efficiently induce harmonic excitation into the object; 2) a MR imaging technique that can successfully encode the tissue response under the induced harmonic excitation to one or a series of wave image(s); 3) an appropriate inversion algorithm that can reasonably convert the wave image(s) to a stiffness map.

2.2.2. Mechanical Stimulation

Magnetic Resonance Elastography uses harmonic vibration to excite the object, and a shear wave is desired in MRE because of its relatively shorter wavelength, which can be more easily captured in the field of view (FOV) in soft tissue, as compared to the compression wave. The mechanical actuation can be generated by various external driver devices. Because of the small dimensions of the objects in the high resolution MRE experiments in this dissertation, a short wavelength is needed so that enough waves can be observed in the FOV, and therefore an actuator that can create stable high frequency vibration is required, such as piezo actuators and acoustic speakers.

A signal generator is used to create the electric harmonic signal for these devices. The signal generator is triggered by and synchronized with the MR pulse sequence. The signal is then amplified by an audio amplifier to induce enough displacement into the object. For the piezo, an additional DC power supply is also needed to give an offset of the voltage in order to avoid negative

voltage which would potentially damage the piezo. Single frequency vibration is typically used in conventional MRE. With the development of MRE technology, multi-frequency vibration can also be encoded in MRE which can efficiently reduce the scanning time if information at multiple frequencies is required [60, 61].

One problem that the high resolution MRE faces is the high attenuation under high frequency vibration. As mentioned above, high frequency vibration is required in high resolution MRE due to the small size of the objects. But in a viscoelastic material, attenuation increases with the frequency, which might cause waves to attenuate such that not enough waves can be captured in the FOV. On the other hand, the size within the RF volume coil or gradient is typically small in the high field MR scanner in order to keep the homogeneity of the RF magnetic field, which limits the available space for the actuation driver. Thus, how to compensate for attenuation and how to minimize the driver are essential in the design of the experimental setup in high resolution MRE. Different customized actuation methods will be introduced in the following chapters corresponding to different experiments.

2.2.3. Deformation Acquisition

The measurement of the tissue motion under the excitation is the technique that involves MRI in MRE. This measurement is based on an phase-contrast MRI technique introduced by Moran in 1982 [62]. Muthupillai et al. then adopted and developed the technique so as to encode the propagating wave in the tissue in response to the excitation. The fundamental of the deformation acquisition is based on the principle that the a phase shift Φ in an NMR signal can be caused by the motion of the nuclear spins when in the presence of a magnetic field gradient, given by [8]

$$\Phi = \gamma \int_0^{\tau} \vec{G}_r(t) \cdot \vec{r}(t) dt \qquad [2\text{-}13]$$

where γ is the gyromagnetic ratio characteristics of the nucleus, τ is the time duration of the gradients, $\vec{G}_r(t)$ is a time dependent function of the magnetic gradient which is so called motion encoding gradient (MEG) in MRE, and $\vec{r}(t)$ is the position of the nuclear spins as a function of time.

Generally, a pulse sequence of MRE can be developed by inserting pack(s) of decent shaped MEGs into any MRI pulse sequence at an appropriate position and synchronize the MEGs with the excitation signal. A typical gradient echo MRE pulse sequence with sinusoidal MEG shape that encodes motion on the slice select direction in shown in Figure 2-6.

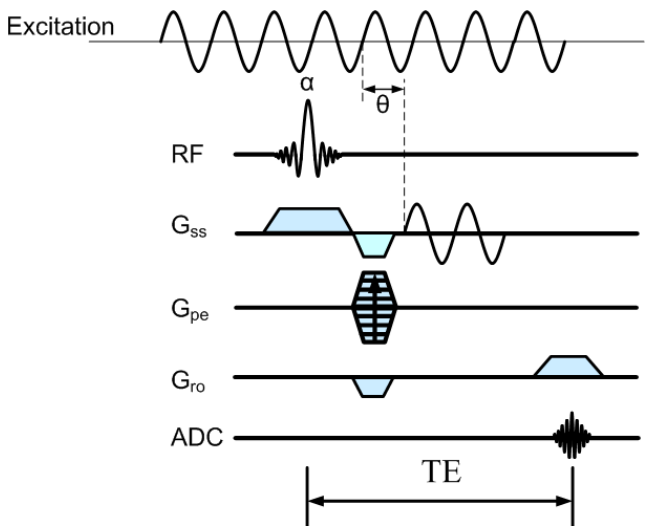

Figure 2-6: A typical gradient echo based MRE pulse sequence with a sinusoidal shaped MEG that encodes motion in the slice selection direction. The MEG is synchronized with the excitation. The phase difference between the MEG and vibration θ varies by different phase offsets.

The excitation is usually triggered before the RF pulse so that have enough time for the tissue to reach a steady state vibration. The most frequently utilized MEG shapes include

sinusoidal, trapezoidal and flow compensated shapes. The MR image obtained by this pulse sequence is called wave image, which shows the information of the propagating wave in the corresponding phase. Typically, two such wave images need to be collected with opposite polarity of the MEG. And subtracting the phase of the two wave images can remove non-motion related phase information [63]. The acquisition repeats for N times (called phase offsets) by changing the phase difference between the MEG and vibration θ by $2\pi/N$ so that to obtain the temporal information of one cycle of the vibration, to show the propagation of the wave and for further post processing.

With the development of the MRE technique, various MRE acquisition methods have been developed to improve MRE efficiency by manipulating the phase shift θ or the waveform of the excitation signal. Using the fractional encoding MRE [64], one can decouple the frequency of the excitation and the frequency of MEG, so that to apply lower frequency vibration, which has lower attenuation in soft tissue, but keep a relatively short TE for a decent SNR of the MR image by using a higher frequency MEG. Using SLIM (SampLe Interval Modulation for the simultaneous acquisition of displacement vector data) MRE [65], one can encode the mono-frequency motion on three directions in one single scan instead of three separate scans in the conventional MRE. Using SDP (Selective spectral Displacement Projection for multi-frequency) MRE [61], one can encode motions of three different frequencies on three directions respectively in one single scan. And using ULTIMAte (Unified Sampling Time Interval Modulation) MRE [66], one can expand this encoding efficiency improvement method to encode as many as possible frequencies information on the any or all of the three directions in one single scan.

2.2.4. Interpretation from the Deformations to Stiffness

The ultimate goal of MRE is to obtain an image that shows the stiffness level of different organs by color so that it can easily help the physicians make a decision of potential disease related

unusual stiffness change. Thus, how to convert the wave image to a stiffness map is an important feature in MRE. This is also a procedure that can achieved by various methods.

2.2.4.1. Local frequency estimation (LFE)

As we know, the wave patterns are different when the wave propagates in mediums with different mechanical properties. When a shear wave at frequency f propagates in a linear viscoelastic material, the shear wave phase speed has a relation with the wavelength λ, the frequency f, the real part of the wave number k, the complex-valued shear modulus G, and the density ρ of the material as follows:

$$c_{ph} = \frac{2\pi f}{real(k)} = \lambda f = \text{real}\left(\sqrt{\frac{G}{\rho}}\right) \quad [2\text{-}14]$$

For most soft tissue the density is assumed to be same as water ($1000\ kg/m^3$); thus, successive estimation of the real part of the wavenumber from the wave image can yield a stiffness map from Equation 2-14. Local frequency estimation (LFE) is an inversion method based on wave number estimation [67]. This is also the first general approach in estimating stiffness data in MRE [8]. In a wave image, the real part of the wave number k can be considered as a frequency in the spatial domain. The LFE is an algorithm that calculates the local wave number (spatial frequency) from a wave image using log-normal filters. Then, using Equation 2-14 a shear stiffness map can be generated. Therefore, the LFE algorithm is more of an image processing technique rather than a mechanics approach. Since the wave number doesn't change during harmonic vibration, a single wave image is required to use this inversion method. This method is relatively insensitive to noise [10] but requires at least a half wavelength of the shear motion in order to provide an accurate estimate of the wave number.

2.2.4.2. Algebraic Inversion of Differential Equation (AIDE)

Soft tissue is considered as a linear viscoelastic material, which leads to its shear modulus being a complex number $G = G_R + jG_I$, where the imaginary part is associated with viscous losses leading to attenuation. The shear stiffness μ estimated from LFE in equation 2-14 is a real value which has a relation with this complex shear modulus G as below (the derivative refers to APPENDIX A) :

$$shear\ stiffness\ \mu = \sqrt{\frac{2(G_R^2 + G_I^2)}{G_R + \sqrt{G_R^2 + G_I^2}}} \quad [2\text{-}15]$$

When doing multiple repetitions (N) of the MRE scan with evenly spaced phase offset (1/N), we can obtain the wave propagation information in the time domain as well, including the attenuation information, by doing Fourier transform on the N wave images. Therefore, in order to obtain the viscoelastic properties of the soft tissue, an algorithm based on a mechanics approach is required. Algebraic inversion of the differential equation (AIDE) is such a method based on Navier's equation[11]:

$$(\lambda + G)\nabla(\nabla \cdot \vec{\boldsymbol{u}}) + G\nabla^2\vec{\boldsymbol{u}} = -\rho\omega^2\vec{\boldsymbol{u}} \quad [2\text{-}16]$$

where λ and μ are the two Lam é constants, and the vector $\vec{\boldsymbol{u}}$ is displacement.

AIDE assumes local homogeneity and isotropic material properties. The equation can be rewritten as:

$$\vec{\boldsymbol{A}}\begin{bmatrix}\lambda + G \\ G\end{bmatrix} = -\rho\omega^2\begin{bmatrix}u_1 \\ u_2 \\ u_3\end{bmatrix},\ \ where\ \vec{\boldsymbol{A}} = \begin{bmatrix}u_{i,i1} & u_{1,ii} \\ u_{i,i2} & u_{2,ii} \\ u_{i,i3} & u_{3,ii}\end{bmatrix} \quad [2\text{-}17]$$

A full inversion of mechanical properties λ and μ from a three dimensional matrix can be then derived as below:

$$\begin{bmatrix} \lambda + G \\ G \end{bmatrix} = -\rho\omega^2 \left(\vec{\boldsymbol{A}}^* \vec{\boldsymbol{A}}\right)^{-1} \vec{\boldsymbol{A}}^* \begin{bmatrix} u_1 \\ u_2 \\ u_3 \end{bmatrix} \quad [2\text{-}18]$$

This three dimensional full inversion algorithm does not make additional assumptions or simplifications, and both Lam é constants can be derived from this method. However, this method requires nearly isotropic voxel /resolution on the three dimension matrix, and is noise sensitive.

Since soft tissue can be considered as an incompressible material [68], Algebraic Helmholtz Inversion (AHI) including two-dimensional inversion and three-dimensional inversion were then derived from above based on assumption of incompressibility [11].

By assuming incompressibility of the medium ($\nabla \cdot \vec{\boldsymbol{u}} = 0$**)**, Equation 2-16 can be simplified as:

$$G\nabla^2 \vec{\boldsymbol{u}} = -\rho\omega^2 \vec{\boldsymbol{u}} \quad [2\text{-}19]$$

By setting all derivatives in the out-of-plane direction ($i = 3$) to zero, the stiffness from a single slice wave image can be obtained from the scalar two-dimensional Helmholtz inversion:

$$G(\omega) = \frac{-\rho\omega^2 \vec{\boldsymbol{u}}(\omega)}{\nabla^2 \vec{\boldsymbol{u}}} \quad [2\text{-}20]$$

A three-dimensional Helmholtz inversion can be obtained in a similar way. Besides assuming incompressibility, additional simplification can be made by neglecting the compressional wave so that applying curl-operator on the three-dimensional displacement matrix $\vec{\mathbf{Q}} = \nabla \times \vec{\boldsymbol{u}}$, which leads to:

$$G\nabla^2 \vec{\mathbf{Q}} = -\rho\omega^2 \vec{\mathbf{Q}} \quad [2\text{-}21]$$

The three dimensional Helmholtz inversion can be derived as:

$$G(\omega) = -\rho\omega^2 \left[\left(\nabla^2\vec{\mathbf{Q}}\right)^{\mathrm{T}}\left(\nabla^2\vec{\mathbf{Q}}\right)\right]^{-1}\left(\nabla^2\vec{\mathbf{Q}}\right)^{\mathrm{T}}\vec{\mathbf{Q}} \quad [2\text{-}22]$$

2.2.4.3. Overlapping subzone technique

Overlapping subzone technique is based on the finite element method (FEM). In this technique, the full partial differential equation is inverted by using Newton's method to minimize the difference $F(E)$ between measured displacement and calculated displacement from FEM by substituting an estimated Young's modulus iteratively [69]:

$$F(E) = \sum_{k=1}^{N}\sum_{i=1}^{3}(u_{ik}^{m} - u_{ik}^{c})^2 \quad [2\text{-}23]$$

where the superscript c denotes calculated and m denotes measured. k stands for a sub-zone.

This algorithm initially solves the displacements for the global system of the problem region for an initial set of material properties, and calculates the error F(E), then creates a subzone containing N elements. The method literately minimizes the error function on the sub-zone, then proceeds with a new one until all of the elements are included in at least a minimum number of sub-zones and the global error is minimized. This method has shown good results [69] on both synthetic data and MRE data, but the disadvantage is the calculation time is long because of the iteration.

2.2.5. Application of High Resolution Magnetic Resonance Elastography

Other than clinical MRE, high resolution MRE focuses more on small samples. For example, high resolution MRE can be used on phantom for theoretical studies, such as examining wave propagation pattern change from one medium to another with different stiffness in different geometry, or as a tool for viscoelastic model identification and parameter estimation. Bioengineered-tissue is used more and more nowadays in tissue engineering studies and clinics. High resolution MRE can also be used to estimate the tissue stiffness during its growth as a

monitoring parameter [70]. Finally, small animal models such as mice, rats and rabbits are very common in various pathology study in disease or treatment progression. High resolution MRE can also server as a tool in estimation of the stiffness change of the diseased tissue, and provides valuable information to clinical application.

3. PHANTOM STUDY ON FEASIBILITY OF MRE IN VISCOELASTICITY ESTIMATION

This chapter was previously published as Yifei Liu, Temel K. Yasar, Thomas J. Royston, "*Ultra wideband (0.5 – 16 kHz) MR elastography for robust shear viscoelasticity model identification*", Physics in Medicine and Biology, 2014. 59(24): p. 7717.

3.1 Introduction

The viscoelastic properties of biological tissue not only affect its motion behavior caused by external dynamic loads, but might also reflect its intrinsic cell structure arrangement. For instance, when considering a fractional Springpot viscoelastic model, the two viscoelastic properties μ_α and α reflect the connectivity and alignment of the structural building blocks in the organ, respectively. These two parameters can change as a result of pathology, which reveals changes in the structure of the cell organization [71, 72]. Thus, identifying the most suitable model and monitoring the viscoelastic property changes could be helpful in diagnosing and monitoring specific attributes of the biological tissue structure. This, in turn, may become a more sensitive and specific biomarker of disease progression and response to therapy. Combining MRE measurements over a wide frequency range can generate curves of the real and imaginary part of the complex shear modulus (storage and loss moduli) that may better capture multiscale tissue behavior as compared to measurements over narrower bands or single frequencies. Viscoelastic model types with fewer parameters that still accurately capture the dynamic viscoelasticity behavior over a wide dynamic (frequency) range are more valuable than more complex models that require more fitting parameters with greater uncertainty and difficulty in interpretation and linking to intrinsic multiscale tissue structure.

Other groups have conducted multi-frequency MRE studies on organ viscoelasticity. A study on brain viscoelasticity was done from 25 Hz to 62.5 Hz with band resolution of 12.5 Hz. Four models – Voigt, Maxwell, Zener and Springpot – were utilized for fitting; the Springpot model

was the best fit [71]. A similar study on liver over the frequency range of 25 Hz to 600 Hz was done by the same group [13, 72]. In these studies, it was also shown that a fractional order model was more accurate than integer order models.

In the present study, MRE was conducted over a wider frequency range, from 500 Hz to 16 kHz, in three experiments of 500 Hz to 3 kHz, 1 kHz to 7.5 kHz, and 5 kHz to 16 kHz. Because the wavelength is inversely proportional to the frequency under harmonic motion where low frequency means long wavelength, and waves attenuate rapidly at high frequency, the boundaries of the frequency range in each experiment are decided by the criteria that a minimum of one full wave should be observed in the sample.

3.2 Material and Method

3.2.1. Sample Preparation

All samples were made with two-part Smooth-On, Inc. Ecoflex® 0010 Platinum Cure Silicone Rubber. Different from the previous study, Silicone Thinner® Silicone Rubber Thinning Additive is added to this combination in this study in order to better release air bubble as well as elongate the sample curing for enough preparation time. A mixture of part A, part B and thinner in ratio of 1:1:0.1 by volume was prepared in a big container before distributing to the three experiment test tubes. The mixture was put in a vacuum chamber (5305-1212, Thermo Scientific-Nalgene, Rochester, NY) for 15 minutes before distribution in order to speed up the air bubble escape.

Because wavelength is inversely proportional to frequency under harmonic motion, three sample tubes in different dimensions were selected in this study for low, mid and high frequency experiments. All of the tubes have both ends open to minimize the effect from compression waves. An inner diameter (ID) = 30 mm, outer diameter (OD) = 34 mm, length L = 35 mm Delrin® tube with both ends open was selected for low frequency experiments from 500 Hz to 3 kHz. In order to avoid the mixture spilling from the tube bottom, the tube bottom was sealed with a piece of

laboratory parafilm (BEMIS®, WI, USA) and then capped tightly with a flat cylinder before pouring the mixture into the tube. The mixture was poured to the top of the tube. This sample is prepared while the mixture is still in liquid state and doesn't capture too much air during the pouring. An ID = 8 mm, OD = 9.5 mm and an ID = 4 mm, OD = 4.9 mm Borosilicate Glass NUM tubes were selected for mid frequency experiments from 1 kHz to 7.5 kHz and high frequency experiments from 5 kHz to 16 kHz, respectively. The mid frequency range and high frequency range glass tubes had the bottom cut to the final length of 70 and 75 mm, respectively. Similar to the Delrin® tube, the bottom of the glass tubes were sealed with a piece of parafilm and a lump of clay to avoid spilling. The same mixture was slowly injected into and filled to the top of the two glass tubes with a 5 ml syringe and PTFE dispensing needle (gauge 16, 1 ½″ long, McMaster-CARR®) to avoid introducing air bubbles into sample.

The curing time for Ecoflex given by the manufacturer is 4 hours at room temperature. In order to ensure it is fully cured and reaches a stable state, the three samples were placed vertically for one week. The sealing parafilm and cap / clay were removed before the experiment.

3.2.2. Magnetic Resonance Elastography Experiment

Magnetic Resonance Elastography is a method based on the principle that when adding an oscillating magnetic gradient to a present magnetic field gradient, a phase shift caused by the motion of nuclear spin accumulates in different amounts Φ in the NMR signal[8]. When the sample is under a continuous oscillatory motion at the same time with the gradient oscillation, the phase accumulation Φ for a given point on the image over a time Δt has a relation with the oscillating gradient and the displacement at that point as below:

$$\Phi = \gamma \int_0^{\Delta t} \vec{K}(t) \cdot \vec{u}(t) dt \qquad [3\text{-}1]$$

where γ is the gyromagnetic ratio of the nucleus, which is 42.576 MHz/T for hydrogen nuclei. $\overrightarrow{GK}(t)$ is the motion encoding gradient (MEG) in the time domain and $\vec{u}(t)$ is the displacement vector in the time domain.

Assuming both MEG and mechanical motion are mono-frequency sinusoids of the same frequency,$G(t) = G_0\sin(\omega t + \theta_g)$ and $u(t) = U_0\sin(\omega t + \theta_n)$, the phase accumulation Φ can be expressed as:

$$\Phi = \frac{1}{2}\gamma TNG_0U_0cos(\Delta\theta) \quad [3\text{-}2]$$

where $T = 2\pi/\omega$ is the period of the mechanical vibration. N is the number of MEG cycles, and $\triangle\theta = \theta_g - \theta_n$ is the relative phase between the mechanical motion and the MEG [8, 19, 73].

In order to obtain the harmonic component of the vibration motion, multiple acoustic wave images (typically four or eight) are obtained from multiple scans by adjusting the phase offset $\triangle\theta$ regularly spaced within a vibration cycle. By extracting the corresponding information from the frequency domain by doing a Fast Fourier Transform (FFT) over these phase contrast images, a complex displacement field can be reconstructed including the information of the amplitude and the phase of the harmonic displacement in the spatial domain[9].

The MRE experiments in this study were completed in two different MRI scanners and three different RF coils in order to cover all three frequency ranges efficiently. The low frequency experiment was conducted in a 9.4 Tesla Agilent (Santa Clara, CA) horizontal bore preclinical MR scanner with self-shielded gradient coils (maximum strength 100 Gauss/cm). The low frequency sample in an OD = 34 mm tube was scanned in a 39 mm birdcage quadrature radiofrequency (RF) coil. Mid and high frequency experiments were done in a 11.74 Tesla Bruker (Billerica, MA) 56-mm vertical bore MR scanner with a 19 mm gradient coils (maximum strength 3000 mT/m). The mid frequency sample in an OD = 9.5 mm tube was scanned in a 10 mm birdcage Bruker RF coil

for the frequency range from 1 kHz to 7.5 kHz. The high frequency sample in an OD = 4.95 mm tube was scanned in a 5 mm Bruker birdcage coil for frequency range from 5 kHz to 16 kHz.

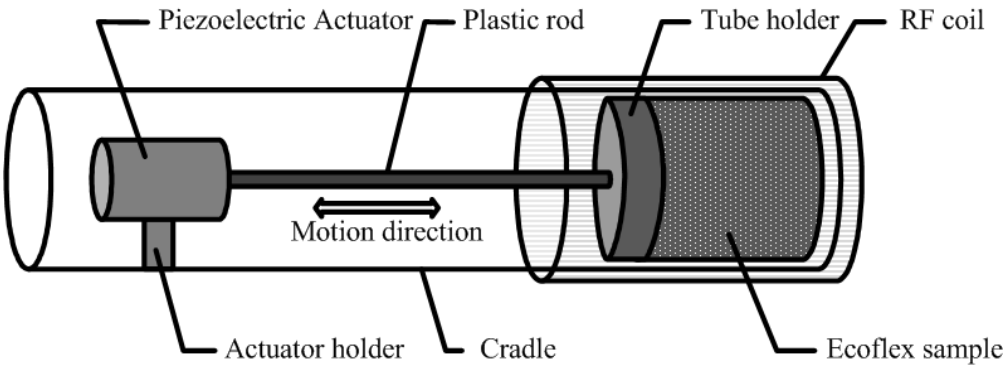

Figure 3-1: Setup for MRE experiment in 9.4 Tesla Agilent horizontal bore system. The piezoelectric actuator is mounted on the plastic cradle. In order to avoid electromagnetic interference between the charged piezoelectric actuator and RF coil, the actuator is located far away from the RF coil. A Delrin® rod connects the actuator and a tube holder which mount tightly on the sample container. An inertial ground (not shown) is connected to the left side of the actuator.

In each of the three experiments, the sample container was driven by a piezoelectric actuator. The MRE setup for mid and high frequency experiments is the same as our previous study [55]. A piezoceramic stack actuator (6.5x.5x18 mm, Thor Labs. Inc) providing 11.6 μm displacement amplitude at 100 Volts was selected for these two experiments. The setup for the low frequency experiment in the 9.4 Tesla Agilent horizontal bore system is shown in Figure 3-1. A preloaded piezo-actuator (P-840.1) from Physik Instrumente (PI) (GmbH & Co. KG, Germany) is selected for this low frequency experiment. The actuator is mounted on a plastic cradle, connected to the test tube via a long plastic rod and a tube holder. This actuator can provide 30 μm displacement at 100 volts. The peak to peak voltage applied to the piezoelectric actuators was 32 Volts for all experiments. A DC supply is added into the circuit in order to give a positive bias to

the voltage and avoid negative voltage to the piezoelectric actuator. The actuator shakes the entire test tube transversely. Because the Ecoflex clings to the test tube wall persistently after it is cured, the tube's transversal motion generates shear waves on the boundary of the sample, which then circularly propagate towards to the center in a focusing fashion.

A gradient echo based sample interval modulation for the simultaneous acquisition (SLIM) MRE pulse sequence [65], which can obtain motion in all three directions in one scan, was utilized in all experiments. Due to the low SNR and wave attenuation at the upper boundary of each frequency range in all three experiments, parameters including repetition time (TR), flip angle (FA), gradient power on slice direction and the MEG duration were adjusted for each frequency accordingly. TABLE I gives the detail values for these parameters. The image acquisition matrix was 128x128 for all scans. The actuator was triggered 20 milliseconds before the MEG pulse starts in order to have the sample reach steady state. The MEG duration was kept to be around 2 milliseconds with an integer MEG number for most of the scans to keep the echo time (TE) short enough for a high SNR free induction decay (FID) signal. For the ultra-high frequency range, 13 kHz to 16 kHz, the MEG duration was increased approximately to 3 milliseconds with an integer MEG number in order to achieve more phase accumulations

TABLE I
MAIN MRE SCAN PARAMETERS FOR ALL EXPERIMENTS

Frequency (kHz)	Scanner	Sample Dia. (mm)	Coil Dia. (mm)	FOV (mm)	TR (ms)	TE (ms) (w/o MRE duration)	FA (degree)	Gradient Power (Gauss/cm)	MEG Duration
0.5 ~1.5	9.4 T	30	39	36x36	100	2.56	20	20	~ 2ms with integer MEG number
1.75 ~3	9.4 T	30	39	36x36	100	2.56	25	20	~ 2ms with integer MEG number
1 ~ 5	11.74 T	8	10	10x10	100	3.95	30	75	~ 2ms with integer MEG number
5.5 ~ 7.5	11.74 T	8	10	10x10	300	3.95	30	90	~ 3ms with integer MEG number
5 ~ 12	11.74 T	4	5	6.4x6.4	500	2.94	50	90	~ 2ms with integer MEG number
13 ~ 16	11.74 T	4	5	6.4x6.4	600	2.94	50	90	~ 3ms with integer MEG number

3.2.3. Complex Shear Modulus Estimation

The geometrical focusing MRE experiment method [74] was utilized in this study. In this method, the cylinder under axisymmetric steady state vertical harmonic motion, $u = u_{za}\exp(j\omega t)$, shown in Figure 3-2a, generates shear waves from the wall of the cylinder. These shear waves propagate towards the center of the cylinder (cylindrical wave propagation) with less attenuation than planar wave propagation due to the geometric focusing phenomenon. For a homogenous and isotropic viscoelastic medium, the displacement along the radial position and far enough away from the free surface at the top and bottom can be written as below:

$$u_z(r,t,k_\beta) = u_{za}\frac{J_0(k_\beta r)}{J_0(k_\beta a)}e^{j\omega t}, \quad k_\beta = \omega\sqrt{\frac{\rho}{G_R+jG_I}} \qquad [3\text{-}3]$$

where $j=\sqrt{-1}$, $J_0(z)$ is the 0th order Bessel function of the first kind, ρ is the medium density, and μ_R and μ_I are the real and imaginary parts of the shear modulus representing the storage and loss property of the medium, respectively. The advantage of this method is that, the shear wave focuses at the center of the sample, and compensates for the attenuation [75]. Figure 3-2b and c show the real and imaginary parts of the displacement at phase 0 for a propagating planar wave and a cylindrically propagating wave for a medium with density $\rho = 1{,}000\ kg/m^3$, G_R = 60 kPa, G_I =15 kPa and radius of 15 mm under a 2 kHz harmonic vibration with amplitude of 1 μm. It can be observed that the shear wave amplitude may even get amplified in the center of the cylinder.

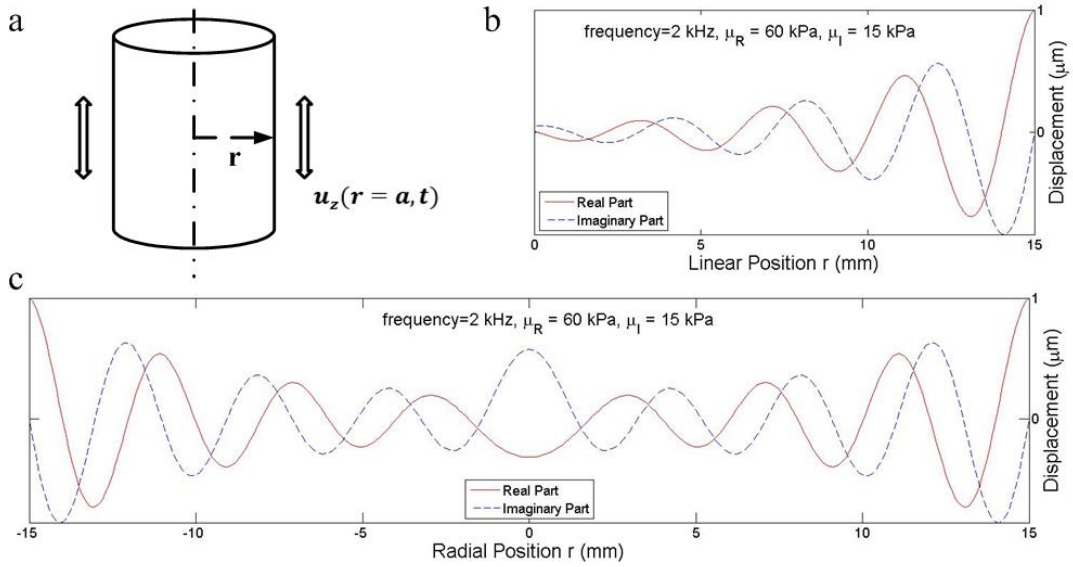

Figure 3-2: a: Diagram of the cylinder used in geometrical focusing MRE method. A harmonic vibration is applied axisymmetrically on the cylinder wall along the vertical direction indicated by the arrows. b: The real and imaginary part of the displacement of planar wave at 2 kHz for a medium with $\mu_R = 60\ kPa$ and $\mu_I = 15\ kPa$. c: the real and imaginary part of the displacement along the radial direction of cylindrically propagating wave generated by geometrical focusing method.

In order to estimate the complex shear modulus of Ecoflex, 18 line profiles with 10° separation passing through the center of the complex MRE wave image encoded in the in-plane direction were taken as shown in Figure 3-3a, b, c and d for frequencies 2.75 kHz, 7 kHz, 11 Hz and 16 kHz, respectively. Each line profile was fit to the closed form solution, as given in Equation 3-3, in order to estimate the real and imaginary part of the complex shear moduli for that particular frequency. The curve fitting was done with a custom written Matlab code utilizing the Global Optimization toolbox. Compared to the previous study, a quadratic offset $y = ax^2 + bx + c$ was used instead of a DC offset y = c in the closed form solution in order to compensate the bias originated from compression waves and uneven vibration due to the unavoidable misalignment of the piezoelectric actuator and the test tube. Figure 3-3e to Figure 3-3l show the fitted result of one of the 18 line profiles from the four frequency wave images in Figure 3-3a, b, c and d,

correspondingly. In these fitted line profile figures, the Y axis indicates the normalized displacement based on the maximum magnitude of the complex displacement over the diameter.

A normalized error for each spatial point was calculated by dividing the difference between the experimental line profile and the estimated line profile from the closed form solution by the maximum absolute amplitude of the experimental line profile.

$$error_{point} = \frac{y_{experiment} - y_{analytics}}{max\left(abs\left(y_{experiment}\right)\right)} \quad [3\text{-}4]$$

$$error = \sqrt{\frac{1}{n}\sum\left(error_{point}\right)^2} \quad [3\text{-}5]$$

3.2.1. Indentation Experiment for Static Shear Modulus

The static shear modulus μ_0 was measured by the indentation experiment. The experiment was done with a force measurement (Model DS2-1, IMADA, INC., IL, USA) and a Quick-Mount Linear Stage (460A series, Newport, Corporation, USA) on the 30 mm low frequency experiment sample. A rigid conical indenter was utilized. In this case, the total force F applied is a function of sample Young's modulus E, the indentation depth and the geometry of the indenter as below:

$$F = \frac{\pi E}{2(1-\nu^2)} a^2 \, tan(\theta) = \frac{2E}{\pi(1-\nu^2)} \frac{d^2}{tan(\theta)} \quad [3\text{-}6]$$

where $d = \frac{\pi}{2}\epsilon$ is the indentation depth, $\epsilon = a \tan\theta$ is the depth of the contact region, a is the contact radius, and θ is the angle between the plane and the side surface of the cone [76]. The tip angle of the indenter is $85°$; thus $\theta = 47.5°$ in this experiment.

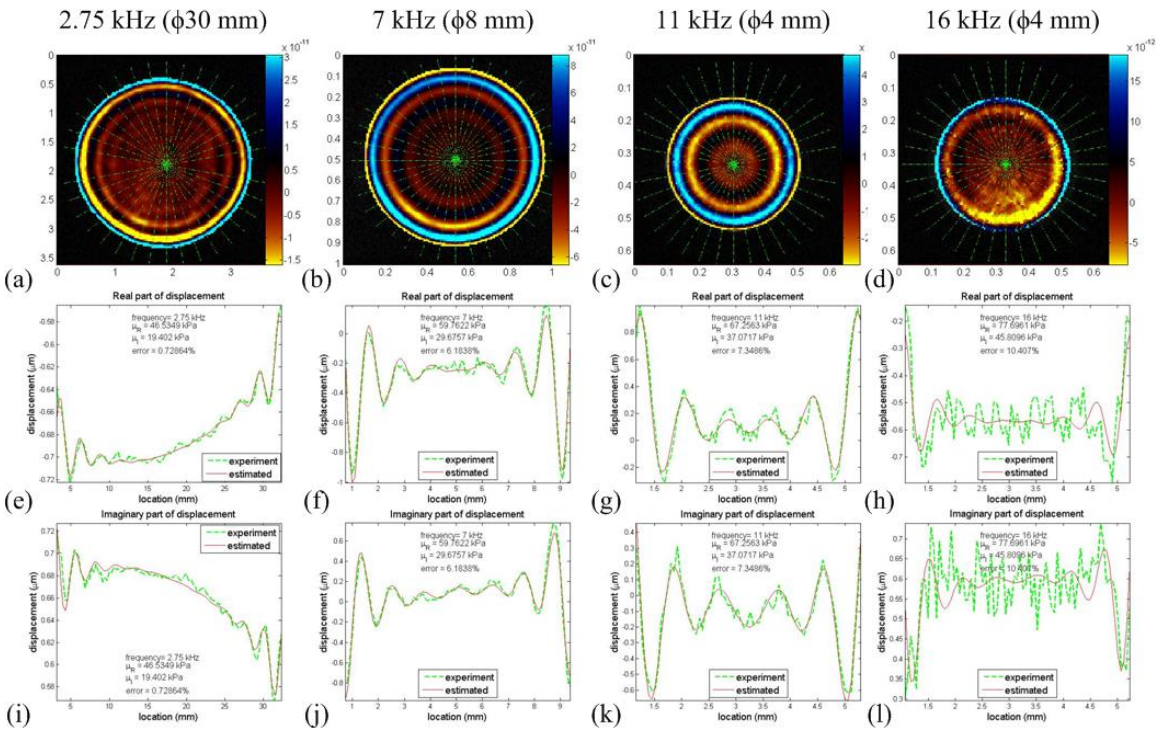

Figure 3-3: Wave image and line profile with curve fitting for real and imaginary part of the displacement result for different frequencies in different sample containers. A quadratic offset strategy was utilized for fitting the closed form solution to experiment line profiles in order to compensate the uneven vibration caused by unavoidable misalignment of the actuator and the test tube. (a, e, i), (b, f, j), (c, g, k), (d, h, l) are results for 2.75 kHz, 7kHz, 11 kHz and 16 kHz from low, mid and high frequency experiments, respectively. The estimated result of the real and the imaginary part of the shear moduli and the error percentage for each fitting are indicated in the fitting plots. The Y axis for (e) to (l) are normalized displacement based on the maximum magnitude of the complex displacement over the diameter.

3.2.2. Viscoelastic Model Parameter Estimation

Because of its characteristics of both elasticity and viscosity, viscoelastic models are constructed as a combination of the basic rheological elements: linear elastic spring(s) and linear viscous dashpot(s). The Kelvin-Voigt Solid and Maxwell-Wiechert Fluid models are the two simplest combinations of these elements in parallel and in series, respectively. A generalized model can be constructed by putting a collection of Voigt or Maxwell units in series, plus an isolated

spring or dashpot. The Generalized Maxwell model is the most widely used linear integer order viscoelastic model. Besides using a collection of a same type viscoelastic unit in a model, composite Voigt and/or Maxwell units and basic element(s) of spring and/or dashpot reproduce more realistic viscoelastic behavior. The Zener model (one version of Standard Linear Solid composite model) is one of these various composite models. [68, 77]. The schematic and corresponding equation of shear modulus in the frequency domain $G^*(\omega)$ of these four models are given in TABLE II Here, μ_0 in Voigt, Zener and Generalized Maxwell models is the static shear modulus measured in the above section *Indentation Experiment for static shear modulus.*

TABLE II
SCHEMATIC AND SHEAR MODULUS OF INTEGER ORDER VISCOELASTIC MODELS

Viscoelastic model	Schematic	$G^*(\omega)$
Voigt	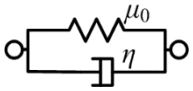	$\mu_0 + j\omega\eta$
Maxwell		$\frac{j\omega\mu_1\eta}{j\omega\eta + \mu_1}$
Generalized Maxwell	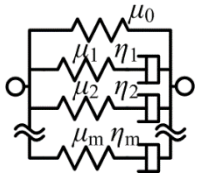	$\mu_0 + \frac{j\omega\mu_1\eta_1}{j\omega\eta_1 + \mu_1} + \frac{j\omega\mu_2\eta_2}{j\omega\eta_2 + \mu_1} + \cdots$
Zener	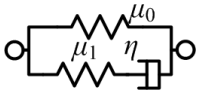	$\frac{j\omega\eta(\mu_0 + \mu_1) + \mu_0\mu_1}{j\omega\eta + \mu_1}$

However, integer order viscoelastic models does not perfectly represent some common viscoelastic materials such as clay and biological tissues. Fractional models were introduced

because of their success in the description of complex dynamics [78, 79]. A widely utilized basic fractional model is the Springpot model (Figure 3-4a), which can be derived from a ladder network model of hierarchical arrangements of springs and dashpots. By assuming $\boldsymbol{E_1 = E_2 = E_3 = \cdots = E}$, $\boldsymbol{\eta_1 = \eta_2 = \eta_3 = \cdots = \eta}$ and $\boldsymbol{\mu_\alpha = E(\eta/E)^\alpha}$, where $\boldsymbol{0 < \alpha < 1}$ is the fractional derivative order, it is usually simplified as a symbol shown in Figure 3-4b with two parameters $\boldsymbol{\mu_\alpha}$ and [78-80]. Adding a spring element in parallel to the Springpot model forms the Fractional Voigt model. When the fractional derivative order $\boldsymbol{\alpha}$ equals to 1, this model becomes a Voigt model. The stiffness of the added spring is equivalent to the measurable static stiffness $\boldsymbol{\mu_0}$, and thus won't increase the unknown parameter number. Three more fractional order models were considered as well in this study, including two fractional versions of the Maxwell model, replacing the spring or dash pot element with the Springpot unit, respectively, and a 3-parameter fractional Zener model which adds a spring in parallel to the fractional Maxwell-Spring model. The schematic and equation of shear modulus in the frequency domain $\boldsymbol{G^*(\omega)}$ of these five fractional order models are shown in TABLE III. Here, μ_0 in all these viscoelastic models is the static shear modulus measured in the section 3.2.1.

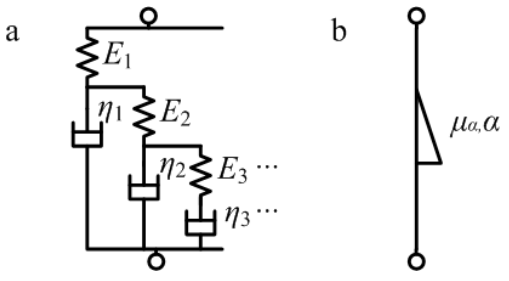

Figure 3-4: a: Schematic of the commonly utilized fractional Springpot model b: simplified symbol of Springpot Model.

In order to estimate the model parameters, as in the previous study [55], the complex shear modulus equation in frequency domain $G^*(\omega)$ of these viscoelastic models were fit to the median of the estimated complex shear modulus over the frequency range from 500 Hz to 16 kHz by minimizing the root mean square error (RMSE) defined in Equation 3-7. A mean absolute percentage error (MAPE) defined as Equation 3-8 was utilized for comparison between models. The curve fitting was done in a customized Matlab code using the global optimization toolbox.

$$error_{RMSE} = \sqrt{\frac{\sum \left(G(\omega)_{model} - median\left(G(\omega)_{experiment}\right)\right)^2}{N}} \quad [3\text{-}7]$$

$$error_{MAPE} = \frac{1}{N}\sum abs\left(\frac{G(\omega)_{model} - median\left(G(\omega)_{experiment}\right)}{median\left(G(\omega)_{experiment}\right)}\right) \quad [3\text{-}8]$$

where *N* is the number of frequency points.

3.2.1. Model Selection Criterion

The number of unknown parameter(s) varies in different viscoelastic models. In order to fairly compare different models, a model selection criterion besides the mean absolute percentage error is necessary. Akaike Information Criterion (AIC) and Bayesian model selection are two popular criteria for model selection in various applications [81, 82]. We choose AIC defined as Equation 3-9 for model scoring in this paper.

$$AIC = Nln\left(\frac{RSS}{N}\right) + 2k \quad [3\text{-}9]$$

$$RSS = \sum\left(median\left(G(\omega)_{experiment}\right) - G(\omega)_{model}\right)^2 \quad [3\text{-}10]$$

Here, N is the number of frequency points, RSS defined in Equation 3-10 is the residual sum of squares, and k is the number of parameters in the model.

TABLE III
SCHEMATIC AND SHEAR MODULUS OF FRACTIONAL VISCOELASTIC MODELS

Viscoelastic model	Schematic	$\boldsymbol{G^*(\omega)}$
Springpot	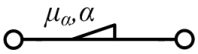	$\mu_\alpha(j\omega)^\alpha, 0 < \alpha \leq 1$
Fractional Voigt	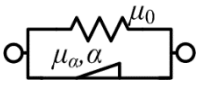	$\mu_0 + \mu_\alpha(j\omega)^\alpha, 0 < \alpha \leq 1$
Fractional Maxwell-spring		$\frac{\mu_1\mu_\alpha}{\mu_\alpha + \mu_1(j\omega)^{-\alpha-1}}, 0 < \alpha \leq 1$
Fraction Maxwell-dashpot	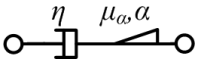	$\frac{j\omega\mu_\alpha\eta}{\eta(j\omega)^{1-\alpha} + \mu_\alpha}, 0 < \alpha \leq 1$
3-parameter fractional Zener	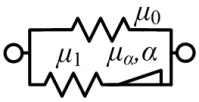	$\mu_0 + \frac{\mu_1\mu_\alpha}{\mu_\alpha + \mu_1(j\omega)^{-\alpha-1}}, 0 < \alpha \leq 1$

3.3 Results

3.3.1. Indentation Experiment for Static Shear Modulus

Figure 3-5 shows the indentation experiment curve. The estimation result of static Young's Modulus E is 36.89 kPa. Poisson's ratio is assumed to be 0.4999998 for viscoelastic material in this study, which results an estimated static shear modulus $\mu_0 = 12.3$ kPa.

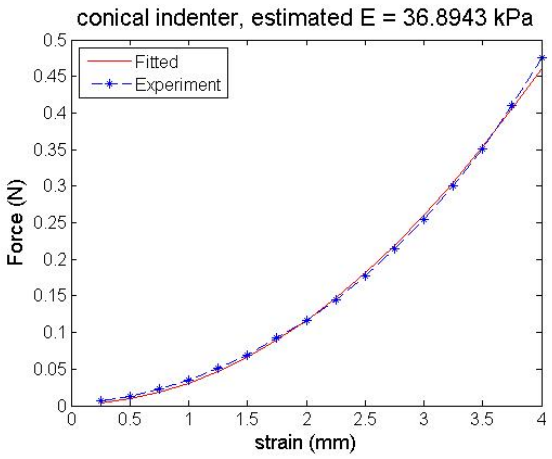

Figure 3-5: Indentation result for static Young's Modulus E with a rigid conical indentor.

3.3.2. Shear Modulus Estimations

The box plot result of the real and imaginary part of the shear modulus over the entire frequency range is given in Figure 3-6. The data of each box comes from the 18 shear modulus estimations corresponding to 18 line profiles. The result from the three experiments are shown in the same plot and distinguished with different colors. For the three experiments, there were overlaps between the low and mid, and mid and high frequency range. The overlapped ranges are indicated with two rectangles in the plot.

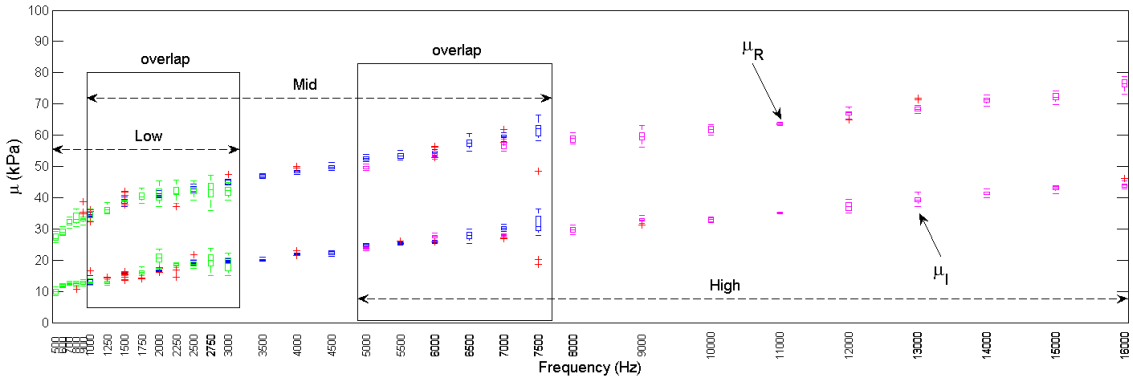

Figure 3-6: Box plot of the real and the imaginary part of the shear modulus estimations. The overlapped frequency range from low and mid, and mid and high frequency ranges are indicated by the two rectangular frames labeled 'overlap'. 32 frequency points (0.5 to 1 kHz with 100 Hz interval, 1 to 3 kHz with 250 Hz interval, 3 to 8 kHz with 500 Hz interval, and 8 to 16 kHz with 1 kHz interval) are listed on the frequency axis. Data from the three experiments of low (ϕ30 mm, 0.5 – 3 kHz), mid (ϕ8 mm, 1 - 7.5 kHz) and high (ϕ4 mm, 5-16 kHz) frequency are grouped with different colors. The lines in the boxes mark the median value estimated from all 18 line profiles of the corresponding frequency scan. The whiskers extend to the most extreme data points, which are plotted as red markers (+)

3.3.3. Viscoelastic Model Parameter Estimations

Four integer order viscoelastic models and five fractional order models were compared in this study. The Voigt and the Maxwell models are the two basic viscoelastic models combining the spring and dashpot elements in parallel and series, respectively. Although it has been observed that these simple two-parameter models do not successfully describe the shear dynamic behavior in many materials [83], these two models were included in the study for reference. Compared to these two models, the three-parameter Zener model, which is a parallel combination of a Maxwell unit and a spring, has more flexibility in representing viscoelastic behavior. The Generalized Maxwell model is the most widely utilized integer order viscoelastic model. Adding more parameters into the equation allows it to adapt to various viscoelastic material behavior for a wide range of frequencies. A 5-parameter Generalized Maxwell model, which includes two branches of Maxwell units, was examined in this study. The parameter μ_0 in Voigt, Zener, and Generalized Maxwell is

the static shear modulus measured in the indentation experiment. The real and the imaginary part of the complex shear moduli of these four integer models and experimental estimation are shown in Figure 3-7a, b. The estimates of the parameters as well as error percentages and AIC score for each model are given in TABLE IV.

TABLE IV
ESTIMATES OF THE VISCOELASTIC PARAMETERS FOR THE INTEGER MODELS

Model	1st Parameter	2nd Parameter	3rd Parameter	4th Parameter	Error (%)	AIC
Voigt	η =0.5455 ($Pa \cdot s$)	/	/	/	68.76	683.3
Maxwell	μ =68.06 (kPa)	η =4.645 ($Pa \cdot s$)	/	/	38.26	642
Generalized Maxwell	μ_1 =78.5 (kPa)	μ_2 =30.17 (kPa)	η_1 =0.72 ($Pa \cdot s$)	η_2 =9.4 ($Pa \cdot s$)	7.08	538
Zener	μ_1 =66.47 (kPa)	η_1 =2.36 ($Pa \cdot s$)	/	/	29.6	624.8

A plot of μ_I versus μ_R of each viscoelastic model and the experimental values are shown in Figure 3-7c. The slope of this plot corresponds to the loss factor in viscoelasticity. It is observed that none of these four integer models offer a good match with the experimental measurement. A normalized root mean square error between the shear modulus $G^*(\omega)$ of each model and experimental result over the frequency range is given in Figure 3-7d.

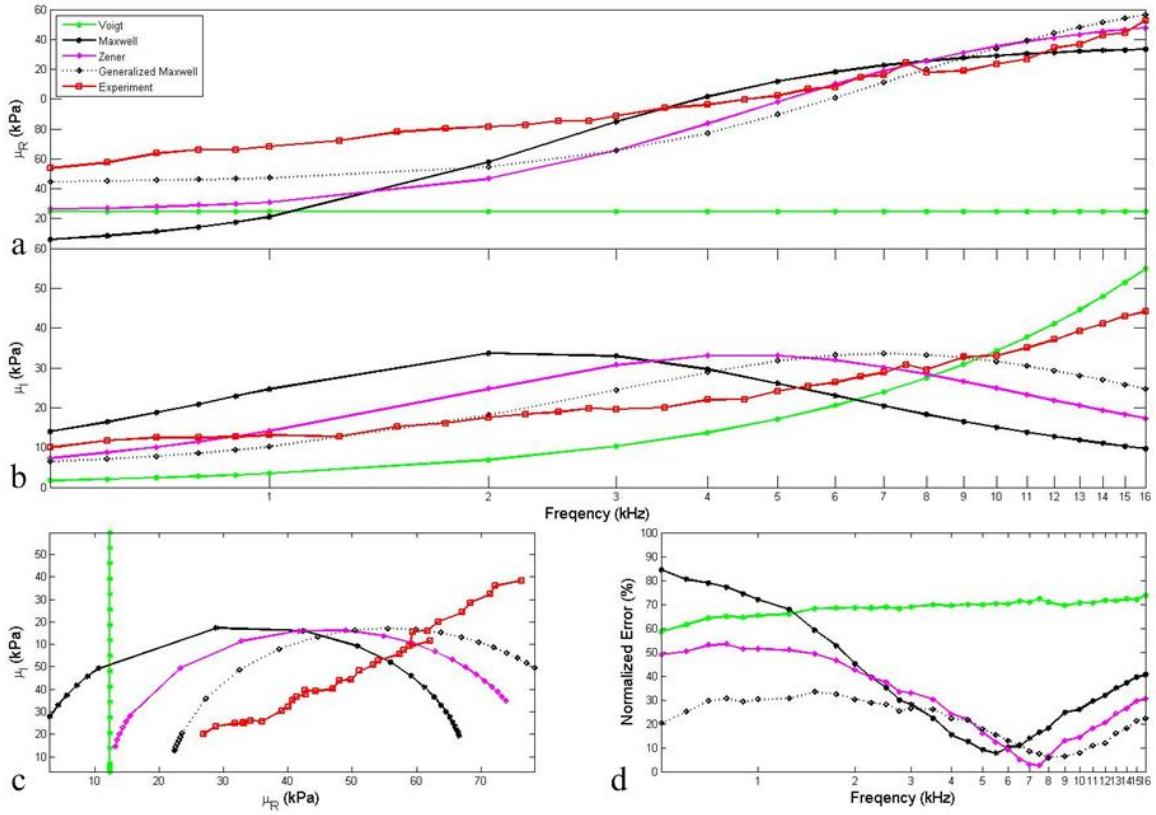

Figure 3-7: The complex shear modulus estimation for four integer viscoelastic models with the parameters estimated via minimization of mean square error between experimental data and the predicted model over the entire frequency range from 500 Hz to 16 kHz: (a) real part of shear modulus μ_R versus frequency. (b) imaginary part of shear modulus μ_I versus frequency. (c) μ_I versus μ_R plot, where the slope of the plot represents the viscoelastic loss factor. (d) normalized root mean square error between the estimated experimental shear modulus and the shear modulus from fitted viscoelastic models.

The previous study has shown that the basic fractional viscoelastic Springpot outperforms the four integer models above. And it also revealed that adding a spring in parallel to the Springpot model gives it even more flexibility and accuracy. In order to examine further how well the fractional models perform, three more fractional models were compared in this study. Estimated complex shear moduli over the frequency range for these five fractional models and experimental estimations are shown in Figure 3-8a and b, and the estimated viscoelastic parameters are given in

TABLE V. The μ_I versus μ_R plot of each model, and the experimental values and the plot of normalized error are shown Figure 3-8c and d, as well. It can be observed that all of the five fractional order models have a better performance than integer order models.

TABLE V
ESTIMATES OF THE VISCOELASTIC PARAMETERS FOR THE FRACTIONAL MODELS

Model	1st Parameter ($Pa \cdot s^{\alpha}$)	2nd Parameter	3rd Parameter	Error (%)	AIC
Springpot	μ_{α} =2626	α =0.2996	/	6.51	528.9
fractional Voigt	μ_{α} =982	α =0.374	/	3.79	499.2
fractional Maxwell-spring	μ_{α} =2300	α =0.3177	$\mu_1 = 10^6$ Pa	7.10	537
fraction Maxwell-dashpot	μ_{α} =2684	α =0.2977	η =500($Pa \cdot s$)	6.81	536.8
3-parameter fractional Zener	μ_{α} =839	α =0. 393	$\mu_1 = 10^6$ Pa	4.12	506.3

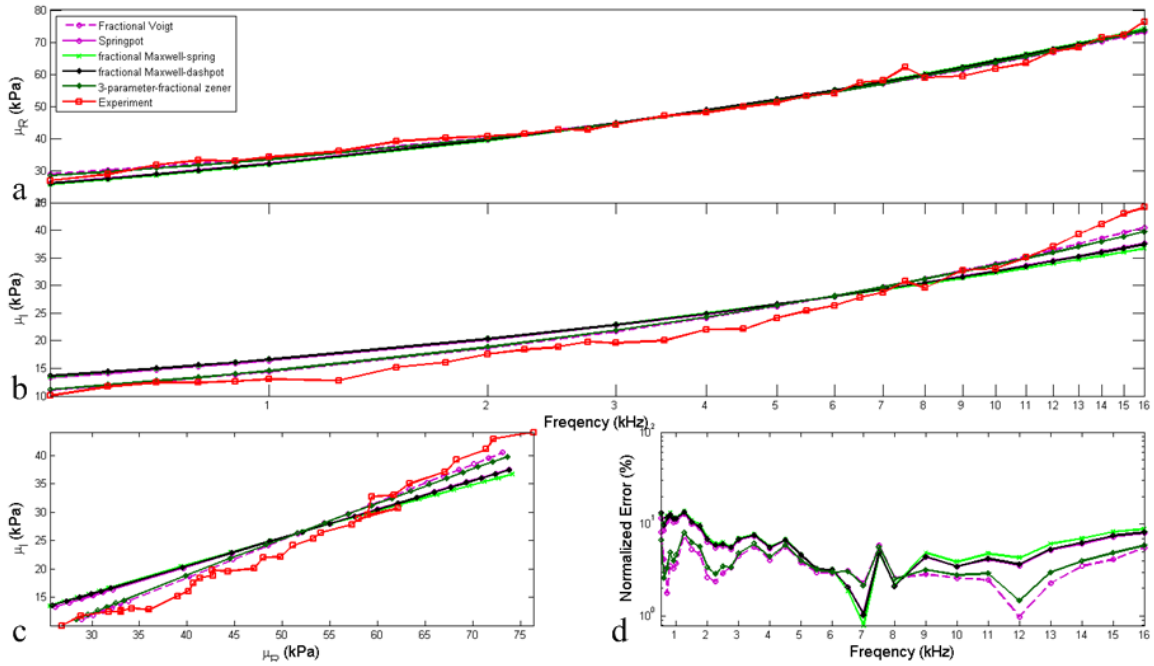

Figure 3-8: The complex shear modulus estimation for five fractional viscoelastic models with the parameters estimated via minimization of square error between experimental data and predicted model over the entire frequency range from 500 Hz to 16 kHz. (a) real part of shear modulus μ_R versus frequency. (b) imaginary part of shear modulus μ_I versus frequency. (c) μ_I versus μ_R, where the slope of the plot represents the viscoelastic loss factor. (d) normalized root mean square error between the estimated experimental shear modulus and the shear modulus from fitted viscoelastic models.

3.4 Discussion

Elastography is becoming more recognized and accepted as a means to quantitatively and non-invasively assess biological tissue *in vivo*. Identifying an appropriate tissue viscoelastic model, and estimating and monitoring its viscoelastic parameters could be a new biomarker and a new approach for diagnosing and monitoring certain pathologies and their response to treatment. Studies have shown that when assuming a Springpot model for brain tissue, the two parameters μ_α and α represent the connectivity and alignment of the structural building blocks in the tissue, respectively [71]. It was shown that specific aspects of brain viscoelasticity were altered in experimental autoimmune encephalomyelitis [84] and after treatment in normal pressure hydrocephalus [85].

Thus, carefully selecting an appropriate model for the biological organ became more important. Many studies has shown fractional viscoelastic models capture the dynamic viscoelasticity of a biological tissue more precisely than integer order models [13, 18, 71]. From the results in Figure 3-7, Figure 3-8, TABLE IV and TABLE V, it can also be clearly observed that even the two-parameter Springpot model outperforms the five-parameter Generalized Maxwell model. Thus, as an extension of the previous study, this article not only expanded the experimental frequency range, but also focused more on the performance of various fractional models.

Considering Figure 3-8 and TABLE V, although the two versions of fractional Maxwell models have one more fitting parameter than the Springpot, the three of them have similar error percentages. Also, the additional parameter, μ_1 or η, reached the predefined upper boundary in optimization. More curve fitting was done with increasing these upper limits, and it was found that the shear modulus curves of these two models approach that of the Springpot when the additional parameters approach infinity. This can also be proven by rewriting the shear modulus equations of these two models as below.

$$G^*(\omega) = \frac{\mu_1 \mu_\alpha}{\mu_\alpha + \mu_1 (j\omega)^{-\alpha}} = \frac{1}{\frac{1}{\mu_1} + \frac{1}{\mu_\alpha (j\omega)^{\alpha+1}}} \qquad [3\text{-}11]$$

$$G^*(\omega) = \frac{j\omega \mu_\alpha \eta}{\eta (j\omega)^{1-\alpha} + \mu_\alpha} = \frac{1}{\frac{1}{j\omega\eta} + \frac{1}{\mu_\alpha (j\omega)^{\alpha}}} \qquad [3\text{-}12]$$

From the observation above, the two versions of fractional Maxwell models, fractional Maxwell spring Equation 3-11 and fractional Maxwell dashpot Equation 3-12, converge to the Springpot model when optimized, and so the 3-parameter fractional Zener model will be equivalent to the fractional Voigt model.

Furthermore, as in the previous study, the fractional Voigt model has a better convergence and lower AIC score than the Springpot model without increasing the number of unknown

parameters given that μ_0 is known. The following conclusions can be made: 1) the Springpot model outperformed most other viscoelastic models because of high accuracy and less optimization parameters were needed; 2) however, if the sample's static shear modulus is measurable, the fractional Voigt model has the advantage of more flexibility and even better accuracy than the Springpot; 3) Increasing the complexity of a fractional model does not necessarily yield a better model estimation due to increased complexity of the optimization and the noise in the experimental data.

This study was done on a tissue-like material. When expanding this method to clinical application, the slower slew rate of the gradient coil in high field human MR scanners limits the upper limit of frequency range. In our previous study, identification of a viscoelastic model in a limited frequency range from 200 Hz to 900 Hz was discussed. It was concluded that, although the error percentage became higher, the fractional model obtained based on a low frequency range was still able to predict behavior at high frequencies (up to 7.75 kHz which is the highest frequency discussed in that paper) accurately. Additionally, real tissue would have more complicated behavior than tissue-like material. As seen from the result in Figure 3-7, integer order models cannot even capture the curve of a tissue-like material. Therefore, it is expected that fractional order models will continue to outperform integer order models in fitting real tissue.

Studies from other groups have utilized the Springpot model for clinical application on brain and liver [71, 72, 84]. From the results in the present study, the fractional Voigt model outperforms the Springpot model by adding a static stiffness in parallel. However, in clinical application, it's impossible to perform *in vivo* indentation tests on an organ. Thus, adding the static stiffness μ_0 as an unknown parameter could be an option if μ_0 converges to the indentation test. In order to test this possibility, another fitting was done on the models to have μ_0 in the equation of $G^*(\omega)$ shown in TABLE VI. It can be found that the μ_0 estimated from fractional Voigt model

converges the best to the static stiffness measured from the indentation. This strengthens the possibility to use the fractional Voigt model for clinical application.

TABLE VI
ESTIMATES OF THE VISCOELASTIC PARAMETERS FOR THE MODELS HAVING STATIC STIFFNESS AS A PARAMETER

Model	μ_0 (kPa)	1st Parameter	2nd Parameter	3rd Parameter	4th Parameter	Error (%)	AIC
Voigt	μ_0=49.83	η =0.5455 $(Pa \cdot s)$	/	/	/	29.97	624.6
Generalized Maxwell	μ_0=27.5	μ_1 =88.8 (kPa)	μ_2 =22.8 (kPa)	η_1 =0.57 $(Pa \cdot s)$	η_2 =2.17 $(Pa \cdot s)$	29.6	624.8
Zener	μ_0=36.4	μ_1 =74.55($kPa)$	η_1 =0.9217 $(Pa \cdot \mathrm{s})$	/	/	13.67	573.1
fractional Voigt	μ_0=16.72	μ_α = 637.3 $(Pa \cdot s^\alpha)$	α = 0.4077	/	/	3.34	495.2
3-parameter fractional Zener	μ_0 =18.33	μ_α =453 $(Pa \cdot s^\alpha)$	α =0.4408	$\mu_1 = 10^6$ (Pa)	/	3.33	496.9

In summary, this study identifies and estimates viscoelastic models and parameters with an approach that compares the complex shear modulus curve in the frequency domain of the predicted mechanical model's equation and experimental estimation on a tissue-mimicking Ecoflex phantom in an ultra-wide frequency range from 500 Hz to 16 kHz. The complex shear modulus of Ecoflex was estimated by curve fits to the closed form solution with line profiles extracted from MRE

experiments conducted in two MRI scanners. Four integer order and five fractional order viscoelastic models were examined in this study, and it is observed that fractional order models describe this viscoelastic material better than integer order models, especially over such a wide frequency range. And, adding a spring element in parallel to a basic fractional model increases the flexibility of the model to also capture static behavior. Among these fractional models, the Springpot and fractional Voigt model have sufficient accuracy and offer the best efficiency with the least number of parameter to be optimized.

4. PHANTOM STUDY OF SHELL GEOMETRY MODEL

Parts of this chapter was previously published as Yifei Liu, Temel K. Yasar, Thomas J. Royston, "*Interpreting Microscopic Magnetic Resonance Elastography Measurements using Finite Element Analysis*", Proceedings of the ASME 2013 International Mechanical Engineering

4.1 Introduction

The left ventricle (LV) has a geometry analogous to a spherical shell with fluid inside. When mechanical waves propagate from the surrounding tissue into the heart, reflection occurs at the solid-solid interface of the myocardium and the surrounding tissue as well as at the fluid-solid interface of the blood in the LV and the myocardium. Thus, assessing elasticity of this geometry structure is also necessary. This chapter is a pilot study to examine how waves propagate in such a spherical shell geometry. In this study, a shell structure phantom with approximately spherical geometry was made out of silicon material filled with liquid. The shell phantom was embedded in agarose gel filled in a test tube. Two situations with different stiffness of the surrounding gel were examined using Microscopic Magnetic Resonance Elastography (μMRE). The results show that reflections occurs at the fluid-solid boundary in the sample, and affected the inversion calculations on the two situations in different ways.

4.2 Material and Methods

A nominally spherical phantom with dimensions of 7x7x6.6 mm^3 was made of a silicon phantom (ECOFLEX 0010, SMOOTH-ON, USA). Water was injected into the phantom during the curing to form a shell phantom with the inner diameter of ~ϕ3 mm. Figure 4-1 shows the 3D model of the phantom reconstructed in MIMICS (Materialise, USA) from the MRI scan of the same sample.

Two MRE experiments with the spherical shell phantom embedded into a ϕ8.8 mm plastic test tube filled with soft surrounding gel (1.2% agarose in water) and a same test tube filled with

stiffer surrounding gel (2.2% agarose in water) were done in the 11.74 Tesla Bruker vertical bore magnet (Bruker DRX-500MHz Avance Spectrometer). Geometrical focusing MRE experiments [75] were performed on both of the samples. The experimental setup is shown in Figure 4-2. The test tube along with the phantom inside was shaken along the longitudinal axis with harmonic vibration at 5 kHz by the piezo-ceramic stack mounted on the top of the test tube. The agarose gel had a welded contact with the test tube wall. Shear waves can thus be generated and propagate inward from the tube's wall.

Figure 4-1: 3D reconstruction model of the nominally spherical ecoflex phantom with liquid injected inside. The left image is the front view and right image is the left view of the phantom.

Ecoflex is a silica based gel while the agarose gel is a water-based gel. In order to prevent chemical shift artifact, frequency offset and fat suppression was applied to suppress the water signal. A spin echo SLIM MRE sequence [65] of 8 phase offsets was applied to encode motion in the three directions in a single scan. 9 slices of saggital scans were acquired. Other scanning parameters includes: TE/TR = 9.62 / 1000 ms, slice thickness = 0.5 mm, acquisition matrix = 128x128, FOV = 1cm x 1 cm. The strength of the MEG gradient was 80 Gauss/cm on each direction. The frequency of the vibration and the MEG was 5 kHz. The output voltage to the piezo was set to a 25 Volts. 20 MSG cycles with 6 pre-delay cycle and 5 post-delay cycles were synchronized with the vibration.

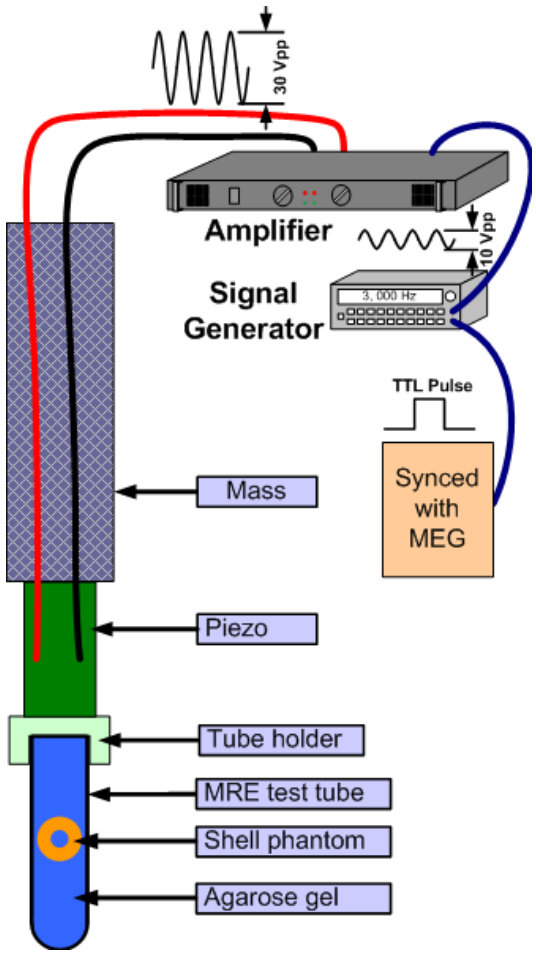

Figure 4-2: µMRE experiment setup. A MEG synchronized harmonic signal was generated from the signal generator and amplified before sending to the piezo actuator. The piezo actuator shakes the test tube vertically. A shear wave was then generated from the wall and propagated radially inwards.

There are multiple inversion algorithms to reconstruct a stiffness map in MRE from wave images. Local Frequency Estimation (LFE) [67] and Helmholtz inversion [11] are the two most popular inversion approaches. Both of these two methods were applied in this study to determine an appropriate inversion algorithm for this special shell geometry sample. A fourth order Butterworth spatial filter with cut-off of 4 and16 waves/FOV was selected based on observation and estimated stiffness, and was applied on the wave images for all three motion directions to filter

out the compression waves and high frequency noise. In this shell geometry, reflection is expected at the fluid-solid interface. Directional filters [86] can be applied to eliminate the reflection effect. Multiple stiffness maps were calculated by applying different numbers of directional filters in order to find out the most efficient combination.

ROIs of the shell phantoms on each slice were semi-automatically obtained by adjusting threshold of the intensity of the MRI image. Erosion of 7 pixels were applied on the ROIs to avoid the boundary condition [87].

4.3 Results

The wave motion on the three directions of the 9 slices from both softer (Figure 4-3a) and stiffer (Figure 4-3b) surrounding gel cases are given in Figure 4-3. Because the water signal (surrounding agarose gel and fluid inside the shell) was suppressed, the signal from the Ecoflex (shell phantom) was dominant in the scan. The same amplitude range was applied on all of the wave images. Shear waves can be observed from the wave motion on vertical directions.

Figure 4-4 shows the stiffness map of all of the 9 slices calculated by applying the Local Frequency Estimation (LFE) method and the Helmholtz inversion with assumption of motion on the vertical direction on the wave images for the softer gel (Figure 4-4a) and stiffer gel (Figure 4-4b) cases. Besides the Butterworth spatial filter, a directional filter of four directions (180°) was applied on the wave image for the Helmholtz inversion to eliminate the reflection at the fluid-solid boundary.

In order to further investigate the effect of a different number of direction filters applied on the wave images in inversion, stiffness maps of 1) without directional filter; 2) 4 directional filter (180° separated); 3) 8 directional filter (90° separated); and 4) 16 directional filters (45° separated) of the softer surrounding gel case is given in Figure 4-5. The reason not to choose the softer surrounding gel case is because the reflection is worse in this case by observing the wave images in Figure 4-3.

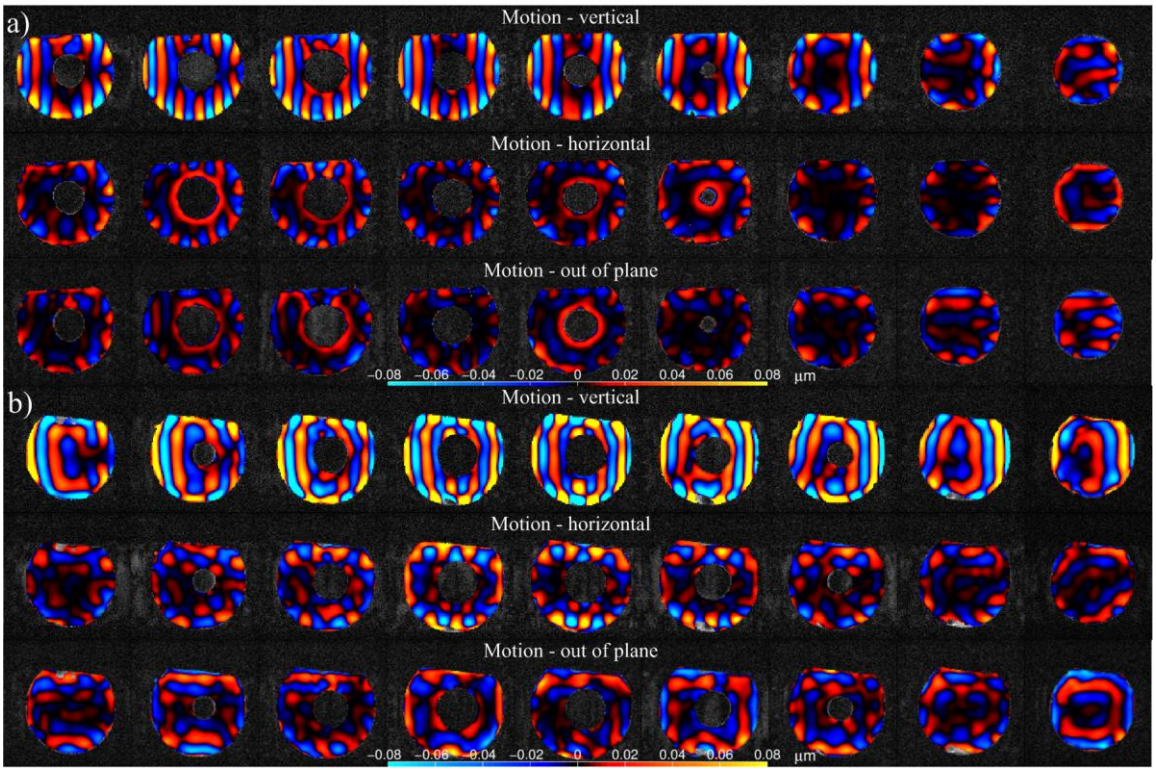

Figure 4-3: Wave image in vertical, horizontal and out of plane directions of the 9 slices for both cases. a) wave images of the softer surrounding gel case. b) wave images of the stiffer surrounding gel.

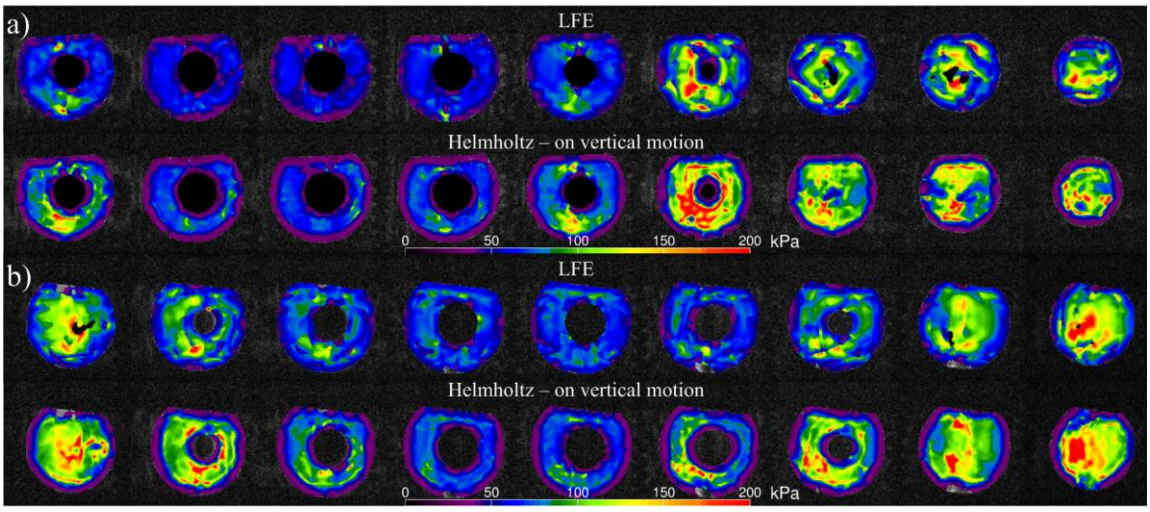

Figure 4-4: Stiffness maps obtained from LFE and Helmholtz inversion of the 9 slices for both cases. a) stiffness maps of the softer surrounding gel case. b) stiffness maps of the stiffer surrounding gel.

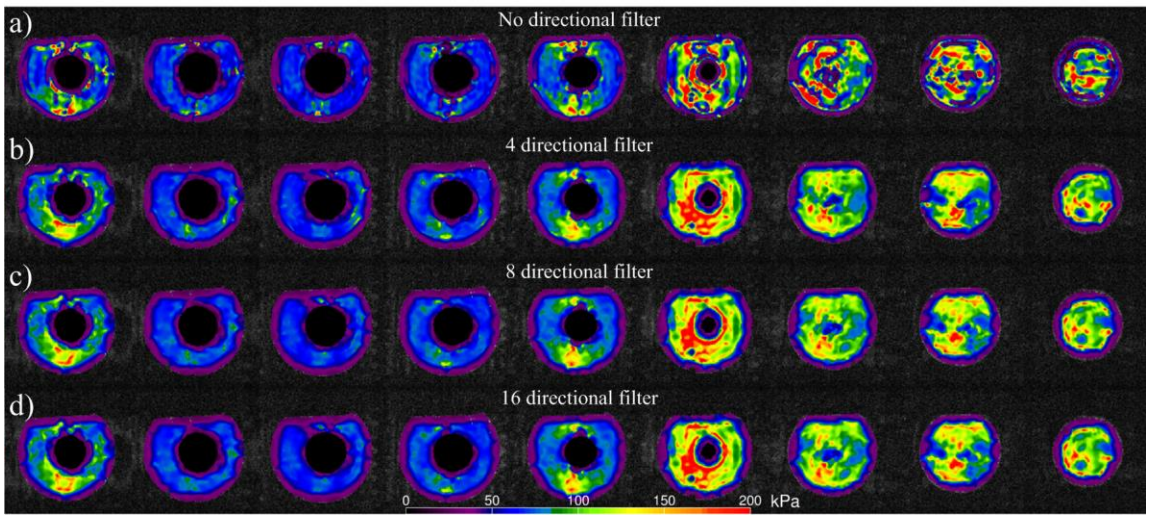

Figure 4-5: Stiffness maps by applying different number of directional filters on the softer surrounding gel case. a) without directional filter; b) applied with 4 directional filters (180° separated); c) applied with 8 directional filter (90° separated); d) applied with 16 directional filters (45° separated).

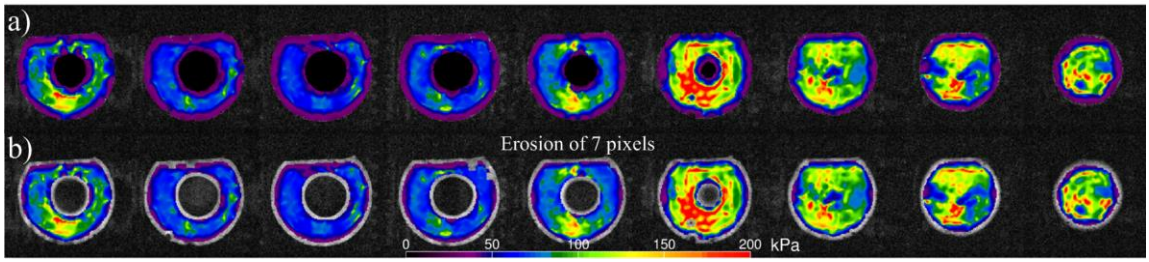

Figure 4-6: Erosion of 7 pixels on the ROI using Butterworth spatial filter and four directional filters on the softer surrounding gel case: a) stiffness maps without erosion on ROI b) stiffness map with erosion on ROI.

Moreover, boundary conditions [87] can be observed in both Figure 4-4 and Figure 4-5, on both outer and inner boundaries of the shell, especially from the result of Helmholtz inversion. ROIs with erosion of seven pixels were thus applied on the stiffness maps, shown in Figure 4-6, for each slice to eliminate the boundary effect. Stiffness was then calculated by averaging over the

ROI, and TABLE VII gives the shear stiffness obtained from LFE and Helmholtz inversion, and the complex shear modulus obtained from the Helmholtz inversion for each slice of both cases.

TABLE VII
SHEAR STIFFNESS AND SHEAR MODULUS RESULTS FROM LFE AND HELMHOLTZ INVERSION

Slice	Softer surrounding gel			Stiffer surrounding gel		
	LFE	Helmholtz		LFE	Helmholtz	
	Shear stiffness (kPa)		Shear Modulus (kPa)	Shear stiffness (kPa)		Shear Modulus (kPa)
1	67.97	78.14	62.22+j33.63	93.53	105.46	77.8+j51.66
2	55.86	61.14	53.48+j22.19	81.72	94.06	70.91+j43.02
3	54.21	58.7	52.65+j19.28	73.49	74.93	61.08+j30.46
4	59.01	63.31	53.68+j24.22	68.68	65.55	57.85+j23.09
5	68.28	75.94	61.6+j32.6	68.37	65.83	57.18+j24.52
6	91.83	115.71	79.49+j57.51	68.33	77.17	61.86+j32.67
7	83.66	94.5	65.29+j49.49	79.78	92.16	71.5+j41.6
8	88.91	96.34	70.04+j46.92	89.79	99.63	73.47+j46.76
9	90.59	95.7	68.1+j44.42	107.85	121.42	86.98+j59.51

4.4 Discussion

In this experiment, the sample was excited in the vertical direction (along the longitudinal axis). Shear waves were generated from the outer boundary of the test tube and propagated radially inwards. However, from Figure 4-3, motions on the axial plane (motion in the horizontal and out of plane directions) can also be observed, especially in the softer surrounding gel case (Figure 4-3a). This is expected since when shear waves propagate in a heterogeneous and multiphase medium a strong reflection of shear waves happens when the wave hits the fluid-solid interface, which complicates the wave pattern. Therefore, finding a method to diminish the influence of reflections before the inversion is required in this case. On the other hand, it can also be observed that the reflection in the stiffer surrounding gel case is less, due to the converging wave pattern in the shell.

In MRE, a directional filter can be applied to eliminate reflections [86]. However, for a shell geometry with strong reflection in the center in this case, how the directional filter can improve the inversion and how many directions is more appropriate and efficient needs to be considered. The softer surrounding gel case was examined with applying different numbers of directional filters because it has a stronger reflection as noted above. From Figure 4-5, it is clear that adding directional filtering improves the inversion significantly, as noted by comparing the stiffness map without and with 4 directional filters. However, applying even more directional filters doesn't necessarily help as 4, 8 and then 16 directional filters did not significantly improve estimates further. Thus, 4 directional filters with 180° separation is enough and efficient in the inversion in shell geometry.

Considering the selection of inversion algorithm, the LFE estimates the stiffness based on estimating the local wavelength, and Helmholtz calculates the stiffness and shear modulus from the wave equation under certain assumptions. From Figure 4-4 and TABLE VII no obvious difference can be found between the results from these two algorithms. The Helmholtz inversion can provide the viscoelastic properties including the attenuation property of the sample. But boundary

conditions need to be considered when using Helmholtz inversion. From Figure 4-4, the LFE is less affected by boundary conditions. Erosion can be applied to eliminate the boundary condition effect, but it's applicable only when the resolution is high and one has enough pixels after erosion.

In summary, this shell phantom study provides useful information for the in vivo cardiac MRE study in the future, including the advantage and disadvantage of using different inversion algorithms, how many directional filters to use for an efficient inversion, and how the reflection can be expected in different surrounding tissue conditions.

5. FINITE ELEMENT SIMULATIONS OF WAVE PROPAGATION IN A COMPUTATIONAL MOUSE MODEL

5.1 Introduction

In the previous chapter, wave propagation in a shell phantom mimicking the left ventricle was studied in an in vitro MRE experiment. However, the murine body has a complex geometry with various organs having different mechanical properties. Although wave propagation in a shell geometry is studied above, wave propagation in the mouse body is still far more complex. Because of the protection of ribcage, it is unclear if mechanical vibratory energy introduced at, for example, the sternum with an amplitude that is not harmful to the animal, will propagate into the heart with sufficient amplitude to enable MRE. In order to address this issue, in this chapter, several computational simulations were conducted to test the feasibility of cardiac MRE and to optimize a vibratory actuator design prior to the costly in vivo experiment. And the results provided valuable information for the actuation method design and vibration frequency selection.

5.2 Methods

5.2.1. Model Reconstruction

In order to create a 3D model of the mouse thorax region with organs of lungs, heart, ribcages, etc. for the simulation, an ECG and respiration gated, *in vivo* 32-slice, saggital, gradient echo, black blood MRI scan of a mouse heart at the end of diastole was taken in a 14.1T Bruker vertical bore MR scanner. MRI parameters include: FOV = 2 cm, matrix size = 256x256, slice thickness = 0.25 mm, TR/TE = 100/2.06 ms, with four averages . The same mouse was sacrificed immediately after the MRI scan and an ex vivo μCT scan was taken on the mouse thorax region. The scan was taken with a μCT 50 (SCANCO Medical, Swiss) scanner, with a slice thickness of 0.01 mm. Three-dimensional computational models of the mouse body and the heart were

reconstructed from the CT scan and the MRI scan in MIMICS (Materialise, Belgium) and combined into one model shown in Figure 5-1.

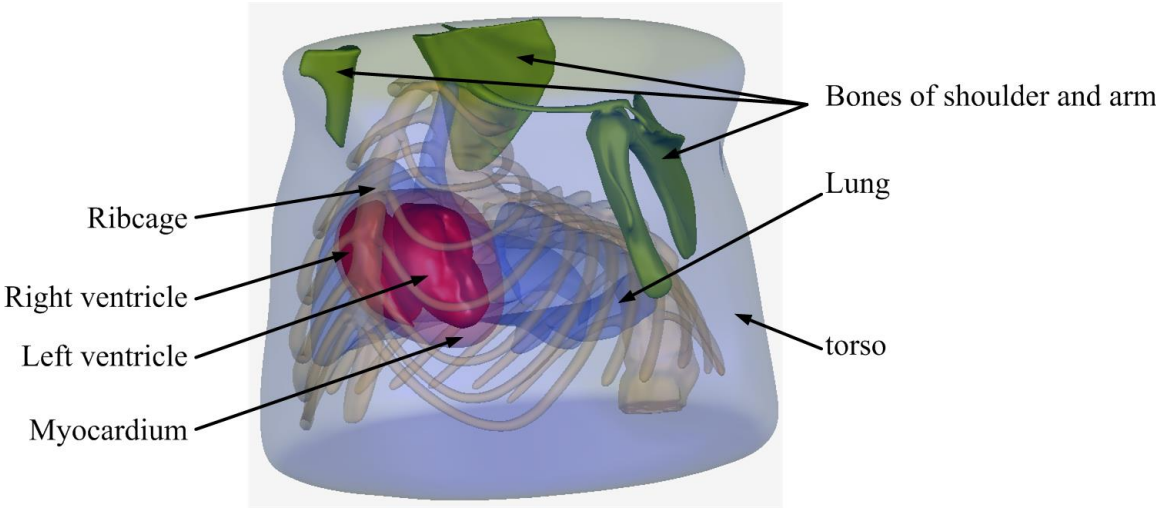

Figure 5-1: 3D model of the mouse thorax region reconstructed from a μCT scan of a mouse body and a thin sliced MRI scan of the mouse heart. The model was reconstructed in MIMICS (Materialise, Belgium).

5.2.2. Material Properties Definition

Material properties need to be defined before doing the simulations. There are a few references estimating soft tissue stiffness of mice in static state [88, 89] or in MRE [90], and for a porcine model in MRE [48] or identified the viscoelastic parameters of the porcine lung [91, 92]. Material properties of each organ were mainly defined based on analogous estimations from these articles. A 3-point bending experiment on the ribcage was also performed to estimate the static stiffness of the ribcage. From Chapter 3, it was found that to best represent viscoelastic behavior of soft tissue, a fractional order model has a better convergence than integer an order model. For

calculation convenience, a Springpot model was assumed for all soft tissues, where the frequency dependent shear modulus $G^*(\omega)$ of this model is:

$$G^*(\omega) = \mu_\alpha (j\omega)^\alpha, 0 < \alpha \leq 1 \quad [5\text{-}1]$$

the loss factor ζ for this model can be derived as:

$$\zeta = \frac{G_I}{G_R} = \tan(\frac{\pi\alpha}{2}) \quad [5\text{-}2]$$

On the other hand, from the introduction in Chapter 2, shear stiffness μ instead of complex shear modulus $G = G_R + jG_I$ is usually estimated, for example by the LFE inversion algorithm. And the shear stiffness μ has a relationship with shear modulus G as below:

$$\mu = \frac{2(G_R^2 + G_I^2)}{G_R + \sqrt{G_R^2 + G_I^2}} \quad [5\text{-}3]$$

Combining Equation 5-1 and Equation 5-3, it can be found:

$$\mu_\alpha = \frac{\mu}{2\omega^\alpha}(\cos\left(\frac{\pi\alpha}{2}\right) + 1) \quad [5\text{-}4]$$

From Equation 5-2, the loss factor in the Springpot model is frequency independent. If the fractional order α is assumed, by substituting the shear stiffness estimation at a certain frequency, μ_α can be found from Equation 5-4. Thus, the stiffness at any other frequencies can be easily estimated.

From the result in Chapter 4, the fractional order α for the Springpot model identification is 0.2996 for Ecoflex, a soft tissue mimicking phantom. So here, α is assumed to be 0.3 for the heart and fat in the simulations in this study.

From an MRE study of mouse liver in the Mayo clinic [90], the shear stiffness of normal mouse liver is around 2 kPa at 120 Hz. Assuming $\alpha = 0.3$, the shear stiffness of the mouse liver at

400 Hz would be 2.87 kPa. According to this, the shear stiffness of mouse fat and heart at 400 Hz were defined to be 2 kPa and 4 kPa. And stiffness at other frequencies can then be calculated. This definition also agrees with the result of the myocardium stiffness obtained in the *in vivo* Cardiac MRE study on a mouse, which will be introduced in the next chapter.

In this simulation, the blood in the left and right ventricle was considered to have zero net flow rate, and defined as a nearly incompressible solid material with very low stiffness (shear modulus = 1+1j Pa).

The stiffness of the lung was defined based on the fractional Voigt model derived for the porcine lung in a recent study [92]. And the wave speed of compression and shear waves were applied to define the material properties of the lung.

A three point bending test was performed in this study on a mouse rib to found the Young's modulus of the ribcage: 836.6 MPa. The Young's modulus of the rat bone is 1.2 GPa according to a reference [93]. Since the ribcage is the factor most important in cardiac MRE study, and waves would be attenuated before it reaches the spine and arm, the Young's Modulus of both bones and ribcage were defined to be 836.6 MPa for simplification. The detailed definition of material properties can be found in TABLE VIII. The shear modulus in simulation at each frequency needs to be calculated using the μ_α and α in the table by Equation 5-1.

5.2.3. Finite Element Simulations

In order to mimic the MRE experiments which reflect the tissue response under vibration, harmonic analysis finite element simulations were performed on this 3D model in COMSOL (COMSOL Inc. USA). The entire geometry was meshed as tetrahedral elements, with the total element number of 522,972. Minimum element size over all geometries is 0.1 mm and the maximum element size is 2.5 mm. Maximum element growth rate is 6.963 and average growth rate is 1.846.

TABLE VIII
MATERIAL PROPERTIES OF EACH ORGAN DEFINED FOR THE SIMULATIONS

Organ	Density $\boldsymbol{\rho}$ [kg/m^3]	Young's Modulus E [MPa]	Poisson's Ratio $\boldsymbol{\nu}$	Bulk Modulus K [GPa]	Shear Stiffness @ 400 Hz $\boldsymbol{\mu}$ [kPa]	$\boldsymbol{\mu_\alpha}$ [kPa·s$^\alpha$]	α	$\boldsymbol{c_p}$ [m/s]	$\boldsymbol{c_s}$ [m/s]
Bone	1500	836.6	0.45	/	/	/	/	/	/
Fat	965	/	/	2.2	2	0.181	0.3	/	/
Lung	250	/	/	/	/	/	/	28.2+6.7j	6.1+1.4j
Heart	1000	/	/	$3*10^{-3}$	4	0.361	0.3	/	/
blood	1060	/	/	2.2	$(1+1j)*10^{-4}$	/	/	/	/

In order to test the feasibility of cardiac MRE, and design the excitation approach, multiple simulations with different actuation methods and different size of the actuation area(s) were performed. The result of a group of simulations has a similar setup with the eventually selected actuation method for the *in vivo* cardiac MRE experiment would be shown in this dissertation. Simulations of other actuation methods would be discussed in session 5.4, the discussion session.

In these simulations, an area on the mouse chest, close to the heart, was excited in the direction into the body (compressional excitation to the mouse body). The actuation area was obtained as a projection of an ellipse with major axis of 5 mm and minor axis of 4 mm on the left thorax area. A 20 μm amplitude harmonic displacement normal to the mouse body was applied on this area as the excitation. An area at the back of the torso, close to the spine, was set to be fixed, mimicking the boundary condition of the mouse lying on a MR scanner slider. Comparing to the

simulations under other type of excitations in this study, this actuation creates the most energy into the mouse body and the wave can propagate into the heart.

In order to find an appropriate driving frequency for *in vivo* cardiac MRE experiment, multiple simulations were also done at different frequencies with this actuation setup. Results of two harmonic simulations with frequency of 400 Hz and 1 kHz, which are two typical frequencies in the *in vivo* cardiac mouse MRE experiments, would be shown in this dissertation. In the *in vivo* cardiac MR imaging, short axis view is usually taken since it gives an excellent cross-sectional view of the left and right ventricles and often displays the cardiac skeleton and valve annuli. So in these simulations, a short-axis slice was also taken on each simulation for comparison and examination of the wave propagation, as shown in Figure 5-2.

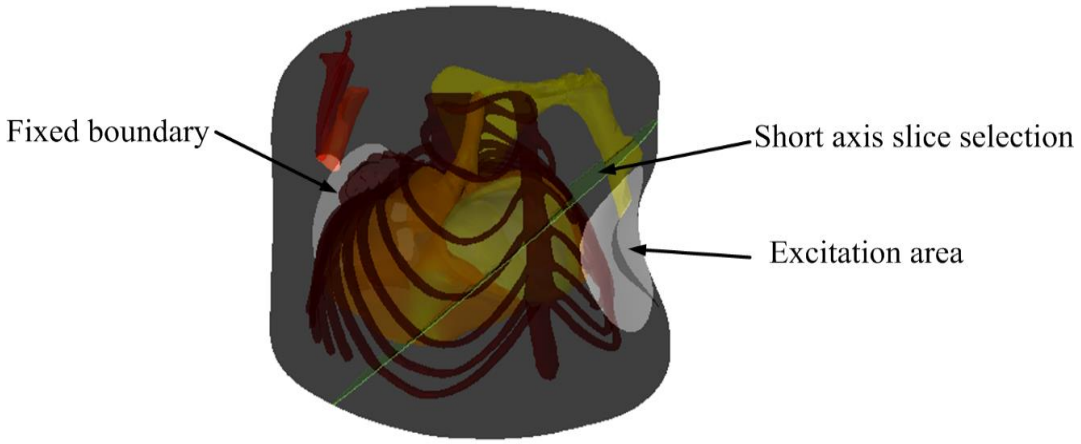

Figure 5-2: The slice selection of short-axis plane of the left ventricle. Wave images will be compared on this plane. A projected area of an ellipse on the model was defined as the excitation area, a 20 μm amplitude harmonic vibration was applied on this area in the direction into the mouse body. An area on the back was fixed to mimics the condition when the mouse lying on the slider in the MRE experiment.

5.3 Results

Wave image results for 400 Hz and 1000 Hz on the short axis plane for the three encoded motion directions are shown in Figure 5-3. The edge of the organs inside, including the lungs, heart, left and right ventricle, the ribcages and arm bones, was also shown in the figure, so that how the wave propagated in different organ can be observed. The wave images on each motion directions and different frequency were scaled in the same color range for comparison. From the wave images, it can be found that wave length is long and the wave penetrated deeper into the mouse body at 400 Hz, and the wave can propagate into the mouse body as well as the heart, although partially, and provides some useful information for the *in vivo* experiments.

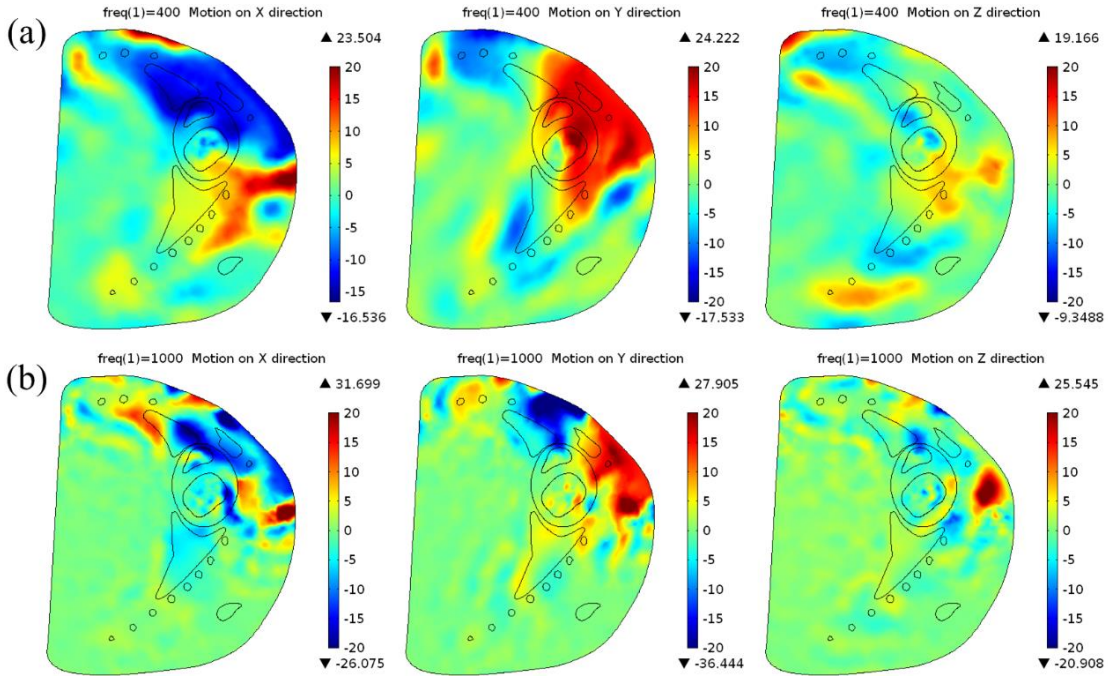

Figure 5-3: Wave images on the short axis slice plane shows the motion on X, Y and Z direction under excitation of a) 400 Hz and b) 1000 Hz. All the wave images are under the same color scale for comparison.

As a further examination, a wave amplitude image was generated for both of the frequencies shown in Figure 5-4. From the wave amplitude image, although the overall wave amplitude was higher under the higher frequency excitation of 1000 Hz, the highest amplitude happened between the actuator and the ribcage, which is mainly due to the reflection.

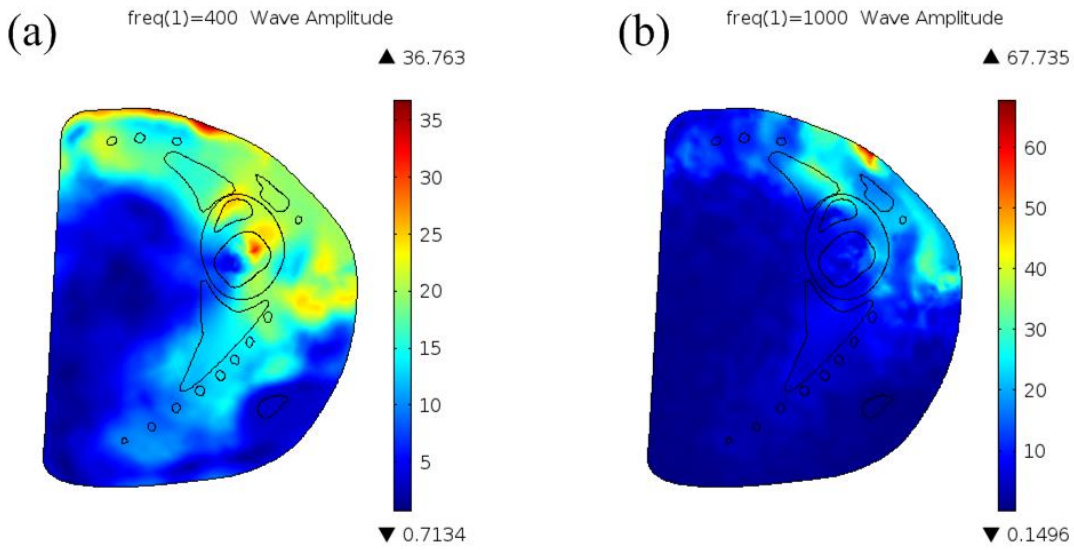

Figure 5-4: Wave amplitude at a) 400 Hz and b) 1000 Hz.

In order to have a better look at the wave amplitude and examine how deep the wave can penetrate into the mouse body, the wave amplitude images were redrawn with the same color range for both of the frequencies as shown in Figure 5-5. From these wave amplitude images, it can be clearly seen that the wave affects more area at 400 Hz due to the lower attenuation.

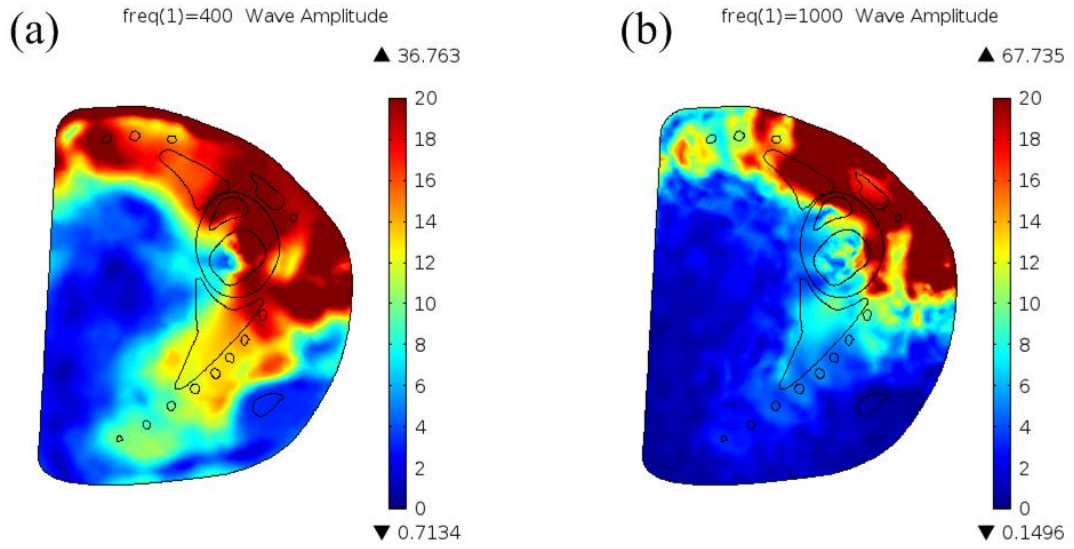

Figure 5-5: Wave amplitude at a) 400 Hz and b) 1000 Hz. All the wave amplitude are at the same color scale.

5.4 Discussion

MR Elastography is becoming more and more recognized in recent years. However, it is also costly, especially during the research stage, due to the use of the MR scanner to test different excitation setups and debugging of the pulse sequence. As a low cost computational method, FEA can be utilized for the mechanical actuation method design in MRE studies, to examine the wave propagation pattern and tissue response under different excitation designs. In this study, finite element simulations were done as a pilot study for the *in vivo* mouse cardiac MRE experiment, providing important information and benefitting the actuation method design.

In this chapter, only simulations with the eventually selected excitation method in the *in vivo* cardiac MRE experiment were presented. However, more simulations were done with different excitation methods. For example, the excitation design of using a piezo actuator drives the mouse chest via a rigid rod (Figure 5-6a) with a harmonic motion in the direction of head to tail was simulated by giving excitation on a small area in the same direction on the chest near the heart.

Design of a cymbal piezo actuator (Figure 5-6b and c) was simulated by given motion in the anteroposterior direction similar as in this simulation, but on a smaller area (same as the size of the cap) and with a lower excitation amplitude (defined by the measurement of the displacement of the cymbal piezo at the corresponding frequency). And excitation on one or two simultaneous excitation area(s) and at different places were examined. Some MRE experiments with these actuation design were also taken to test the result. However, both the MRE experiment results and the simulations results of these two designs showed limited wave propagation into the mouse body, and only the design shown above had the best penetration.

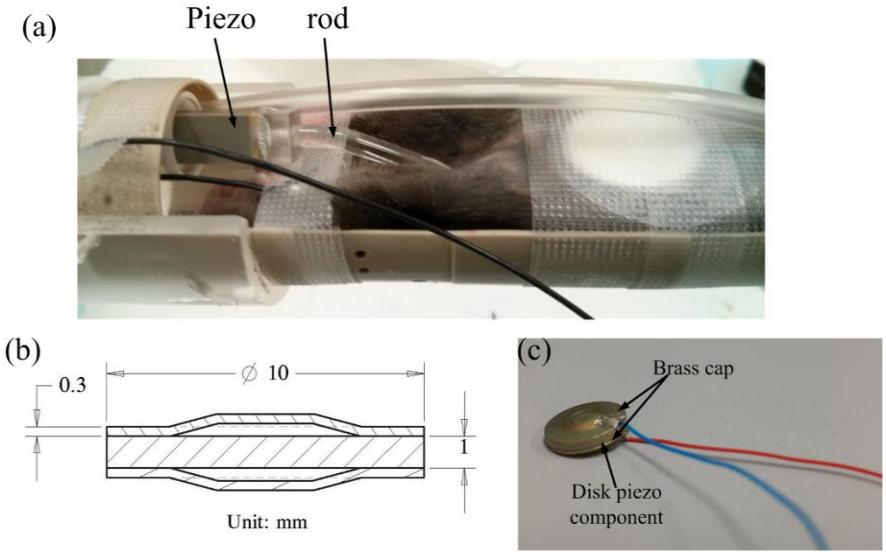

Figure 5-6: Other excitation designs were examined in the simulations. a) design of using a piezo to give a motion horizontal to the head to tail direction of the mouse via a rigid rod b) and c) design of a cymbal piezo actuator

By observing the simulations results in this chapter with the final selected excitation design, several conclusions can be made. First of all, this design can induce wave penetration into

the mouse heart. This promising result confirmed the potential feasibility of *in vivo* cardiac MRE in a mouse with this excitation design. Furthermore, by comparing the wave images and wave amplitude images at two frequencies in Figure 5-3 and Figure 5-5, the lower frequency of 400 Hz has longer wave length and less attenuation so that can affect more areas inside of the mouse body. However, from the wave amplitude images of Figure 5-5, even if under the lower frequency of 400 Hz, the wave attenuated fast and cannot have impact on the entire heart region. Although there is a possibility that the material properties defined in these simulations overestimated the attenuation capability of the soft tissue, this result provided important information and a reminder that the region of interest (ROI) selection should consider this factor in the post-processing of MRE experiment data in the future. Moreover, due to the complicated geometry of the mouse body, waves can be observed on the three directions; so, 3D motion encoding should be considered in the *in vivo* MRE experiment as well.

The finite element simulations on the 3D mouse model are very informative as a low cost *virtual* experiment method, and so is very useful in the *in vivo* MRE excitation design. However, the accuracy of the result is also highly dependent on the material properties definition. On the other hand, the anatomical geometry also varies when the animal at different position or condition, for example, the shape of the fat would be different when the animal is at supine or at up-right positon and so that affects the simulation result. Furthermore, especially for the cardiac MRE, the myocardium stiffness varies during the cardiac cycle. Mimicing the wave propagation in the myocardium during the cardiac cycle at different phase involves transient simulations and more pressure information to define the mechanics between the myocardium and blood flow. Thus, finite element simulations on animal related MRE experiment can provide useful information, but is difficult to be fully comparable with the experiment result.

6. FEASIBILITY STUDY OF IN VIVO CARDIAC MAGNETIC RESONANCE ELASTOGRAPHY ON MOUSE

Parts of this chapter was submitted (first submitted on April 2015, second revision submited on September 2014) as Yifei Liu, Thomas J. Royston, Dieter Klatt, E. Douglas Lewandowski, "Cardiac MRE on mouse heart: initial results", Magn. Reson. Med

6.1 Introduction

Increased left ventricle (LV) stiffness, one of the contributing factors to abnormal systolic or diastolic function, has been found in various cardiovascular diseases (CVD) such as diastolic heart failure, cardiac fibrosis, steatosis, altered sarcomere activity and hypertension [94-98]. Conventionally, the primary approaches to assessing the contractility of the LV include an invasive method of measuring the pressure-volume (P-V) curves over the cardiac cycle [99, 100] and noninvasive approaches of assessing deformation of the LV during systole and diastole, such as tagged MRI [101] or strain and strain rate echocardiography [102, 103].

As a remote palpation method, MR Elastography (MRE) is capable of estimating tissue stiffness or viscoelasticity non-invasively. MRE is a phase contrast-based MRI technique that observes the tissue response to a cyclic mechanical excitation. Subsequently, a map of the viscoelastic or stiffness properties of the targeted region of interest (ROI) is calculated with an appropriate inversion algorithm. MRE is a useful tool for the noninvasive mechanical characterization of soft biological tissues, including phantoms and engineered constructs [54, 70], and the technique shows diagnostic potential for various diseases affecting different organs, such as the liver, brain, muscle, etc. [9, 16, 71].

Using MRE to noninvasively estimate the myocardium stiffness has been attempted in humans and large animals using a shear wave amplitude approach (WAV-MRE) [25, 104, 105] and using a shear wave inversion approach (WI-MRE) [48, 106]. Both techniques indicate the diagnostic potential of cardiac MRE. The mouse model is a very common animal model in CVD

studies [107, 108], which can provide fundamental insight into disease progression and pathophysiology. While there have been numerous studies applying MRE to the mouse brain [84, 109], there are few studies applying any form of noninvasive elastographic imaging to internal organs and deep structures within the torso of the mouse. This limited application is a consequence of the unique technical challenges associated with accounting for the rapid cardiac and respiratory cycles, in addition to the small dimensions. To the best of the author's knowledge, the study presented here is the only published account of mouse cardiac MRE. MRE, which uses an external stimulus potentially enables quantitative and localized estimates of myocardial stiffness without the need for invasive catheterization. In this study, MRE was implemented on a healthy mouse model to assess the stiffness and shear wave amplitude change in the myocardium during the cardiac cycle. This study is challenging due to the fast heart beating rate (typically 500 beats/min) and small dimension of the mouse heart (typically less than 10 mm in all directions). The result is promising and demonstrates how myocardial stiffness and shear wave amplitudes change during the cardiac cycle.

6.2 Methods

6.2.1. Experimental Setup

Five female adult C57BL/6 mice (age range 3-13.5 months, weight range 20-30 grams) were examined. The experiments conformed to our university Animal Care Committee (ACC) principles, and all the procedures were approved by the university ACC committee.

Mice were induced anesthesia with 5% vol. isoflurane in 1-liter oxygen flow for 3 min in an induction chamber and then were placed in a customized nonmagnetic cradle with a nose cone for inhaled anesthesia (1-1.5% vol. isoflurane at 1-liter oxygen flow), delivered with an isoflurane vaporizer machine (E-Z Anesthesia, E-Z System Corporation, PA). Mice were positioned supine in the cradle. The hair on the left thorax area was removed with Nair® depilating agent. A 3D printed polylactic acid (PLA) plastic tube tip was then placed on the chest above the heart as a

passive driver as shown in Figure 6-1b. The right front paw and left back paw were connected to ECG leads. A respiration pillow was placed and taped on the abdomen area.

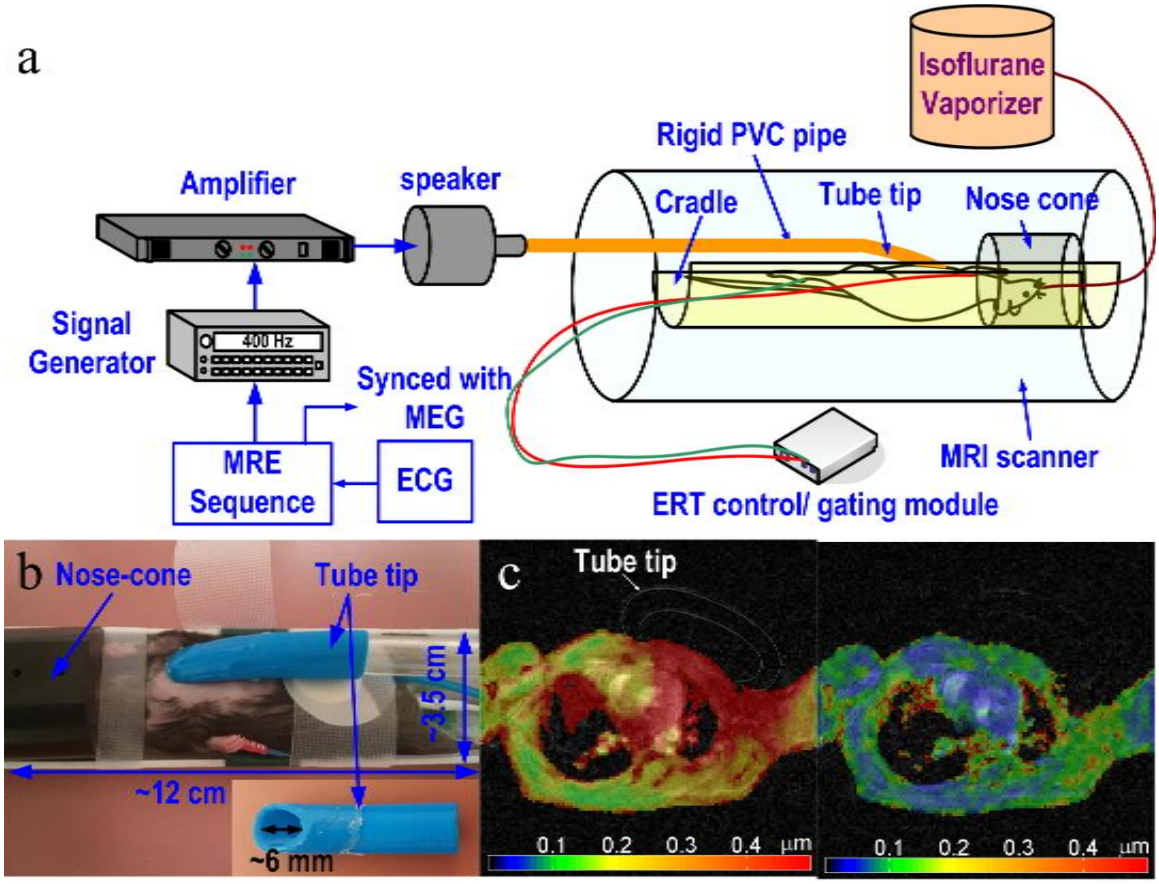

Figure 6-1: a) Cardiac mouse MRE experimental setup. The mouse was positioned supine in a customized nonmagnetic cradle with a nose cone connected to an isoflurane vaporizer for inhaled anesthesia. A 3D printed tube tip was placed on the left side of the chest of the mouse at one end and connected to an acoustic speaker at the other end via rigid PVC pipes. ECG, respiration and temperature signals were monitored by an ERT control/gating module; b) The photo of the mouse setup with the customized nose cone and the 3D printed tube tip. c) and d) A confirmation of the excitation from this setup by comparing the wave amplitude image of an MRE scan (c) and a control scan (d) at the same cardiac phase (at ES) in mouse #5. The location of the actuator tip is tagged on the figure c. Intensity of the tip was weak in the magnitude images and therefore graphically highlighted in the figure.

All experiments were performed on a 9.4 Tesla Agilent (Santa Clara, CA) horizontal bore preclinical MR scanner with a self-shielded gradient coils (maximum strength 100 Gauss/cm) and a $\phi 39$ mm birdcage quadrature RF coil. The mouse along with the cradle was slid into the scanner. An air heating system (SA Instruments, Inc. NY) regulated the body temperature of the mouse and kept it ~$37°C$. The other end of the tube tip was connected to an acoustic speaker (11829BT, Electro Voice, MN, USA) located ~5 meters away from the magnet via several long rigid PVC pipes. The acoustic speaker was driven by an audio amplifier (P3500S, YAMAHA, Japan). The ECG, respiration and temperature signals were detected and monitored by an ERT control/gating module (SA Instruments, Inc. NY). The schematic of the experimental setup is shown in Figure 6-1a.

6.2.2. Image Acquisition

A gradient echo based cine-MRI sequences was upgraded with MEGs and prospective ECG triggering for cardiac cine-MRE. We adopt the concept of fractional encoding in order to combine rapid acquisition (and thus short MEGs) with low frequency vibrations. Fractional encoding has been introduced by Rump et al. [64]. In its cardiac MRE implementations one specific vibration state is estimated from successive repetition time (TR) intervals [104] which implies a condition for the MEG period (τ_g), the mechanical vibration period (τ_v) and the repetition time TR:

$$\tau_v = N \cdot TR; (N = 1,2,3 \dots), \text{ and } q = \frac{\tau_g}{\tau_v} < 1 \qquad [6\text{-}1]$$

Due to the lower limit of our acoustic speaker (~280 Hz) and the need for a sufficient TR based on SNR considerations (a longer TR is required due to the longer T1 under this ultra-high magnetic strength), we implemented fractional MRE with a vibration period τ_v that was shorter than the TR. This implementation violates Equation 6-1 and therefore, we propose a data acquisition scheme that allows for arbitrary phase shifts of the vibration instead of phase-conformed in successive TR intervals. As illustrated in Figure 6-2, the vibration was activated by the R-wave

ECG signal and was maintained for 1.5-2 cardiac cycles in expiration. During the interval of active vibration, data were acquired for one line in k-space with 16-18 phases (number of phases depends on mouse heart beating rate) corresponding to different phases of the cardiac cycle. After the ECG trigger, a minimum vibration forerun of 20 ms was allowed before the start of the first phase for ensuring a mechanical steady state. After the last cardiac phase the vibration was turned off and the sequence of events was repeated for acquisition until the k-space was filled. Temporal resolution with eight time steps was achieved by increasing the forerun for consecutive image acquisitions by $\frac{1}{8}\tau_v$.

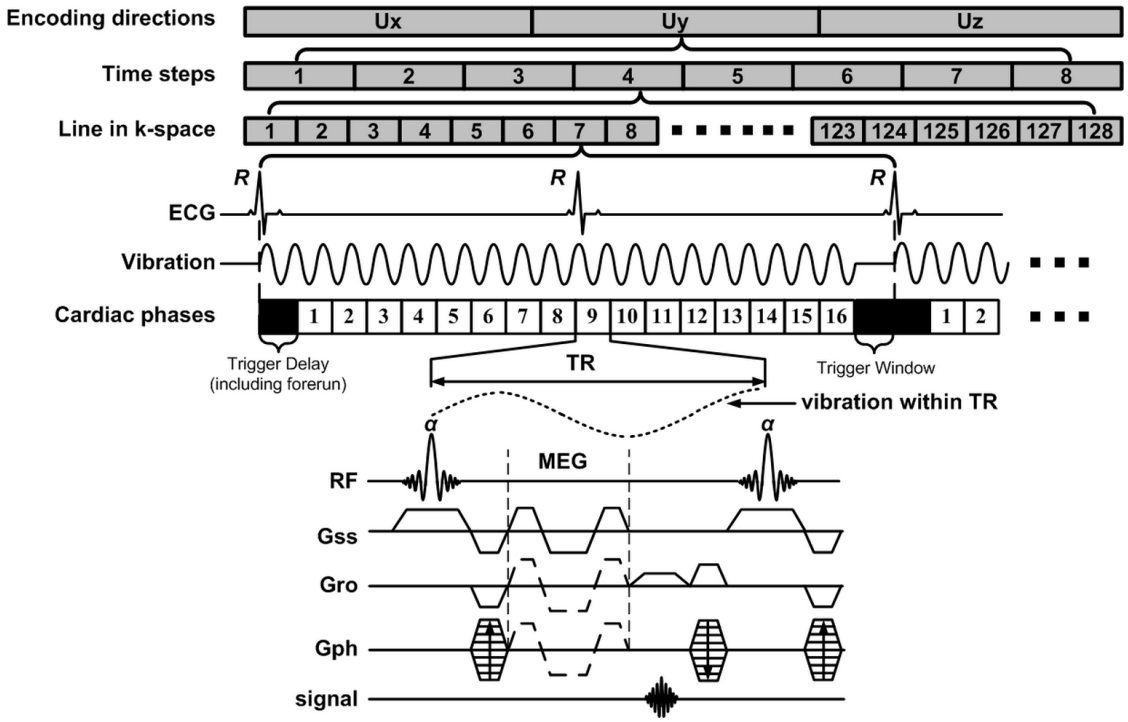

Figure 6-2: A modified fractional encoding, prospective ECG-gated, gradient echo cine-MRE pulse sequence. The mechanical vibration is triggered with the R-wave ECG signal and is turned off immediately after the MEG of the last cardiac phase. The forerun time between the mechanical vibration trigger and the RF pulse of the first cardiac phase acquisition allows enough time for the acoustic wave to travel from the speaker to the mouse body and reach steady state. A flow compensated motion encoding gradient shape is applied to compensate for blood flow. More than 1.5 cardiac cycles are scanned in order to reconstruct the motion in at least one full cardiac cycle.

A short-axis slice was selected at the middle level of the LV for MR imaging. An MRE scan without acoustic actuation was performed as a control scan. Typical MRE sequence parameters were: FOV=2.5x2.5 cm with a 128x128 matrix; single slice of 1 mm slice thickness; flip angle $\alpha = 20°$; 2 averages; 400 Hz of vibration; one cycle of a flow-compensated MEG with a strength of 20 Gauss/cm and a duration of 1 ms. With timing parameters of TR/TE = 9.44/2.25 ms and a heart beating rate of 440~500 beats/min, the scan duration for one motion encoding direction was typically 12.5 minutes. The 3D displacement vector was acquired by repeating the acquisition with varying MEG directions resulting in a total measurement time of 37.5 min for each data set.

6.2.3. Data Processing

Image post-processing was performed using a custom-written software using Matlab (an executable file is downloadable on our lab website as a sharing resource, the link will be updated in the final submission, and a movie file of this software is submitted as well for review and online publication). Phase-difference images were calculated to correct for static field inhomogeneity by subtracting phase images acquired with relative trigger shifts of $\frac{\tau_v}{2}$. Subsequently, the complex wave image for each cardiac phase on each encoding direction was obtained after a Fourier-transform on the phase-difference images over one vibration cycle. A fourth order Butterworth bandpass filter with bandwidth of 1-30 waves/FOV plus an additional 2D directional filter (four directions separated by 90°) were applied on the complex wave images to remove high-frequency noise and compensate for reflections [86]. Since data is available only in a single image slice, we are restricted to calculate the complex shear moduli G from the filtered complex wave images U using a 2D direct inversion algorithm (Helmholtz inversion). The complex shear moduli $G_{j,n}(x, y, \omega)$ at cardiac phase $\#j$ on direction n ($n = 1,2,3$) were calculated from the filtered complex wave images $U_{j,n}(x, y, \omega)$ using a 2D direct inversion algorithm (Helmholtz inversion) [11, 63] shown in Equation 6-2:

$$G_{j,n}(x,y,\omega) = \frac{-\rho\omega^2 U_{j,n}(x,y,\omega)}{\nabla^2 U_{j,n}(x,y,\omega)} \quad [6\text{-}2]$$

We determined for each cardiac phase an effective complex shear modulus G_{eff_j} as a weighted sum of the complex shear moduli along the three directions and the weighting coefficient is calculated from the direction-dependent displacements [50]:

$$G_{eff_j}(x,y,\omega) = \sum_{n=1}^{3} G_{j,n}(x,y,\omega) \cdot w_{j,n}\,,\; w_{j,n} = \frac{|U_{j,n}(x,y,\omega)|}{\sum_{k=1}^{3}|U_{j,k}(x,y,\omega)|} \quad [6\text{-}3]$$

In addition to the wave inversion based processing approach we also assess stiffness variations over the cardiac cycle by observing shear wave amplitude variations. We adopt the theory of Sack et al. [52], that the ratio of the wave amplitude $\bar{U}$ at two different time points t_1 and t_2 is inversely related to the ratio of stiffness μ under the assumption of a constant flux of the elastic wave energy:

$$\frac{\mu(t_1)}{\mu(t2)} = \left(\frac{\bar{U}(t_2)}{\bar{U}(t_1)}\right)^4 \quad [6\text{-}4]$$

6.2.4. Region of Interest Selection

Due to the attenuation, the intrinsic contraction of the heart and the location of the excitation, the impact of the mechanical acoustic wave on the mouse body as well as the mouse heart varies from anterior to posterior locations. The wave amplitude therefore needs to be considered in deciding a suitable ROI for analysis. The wave amplitude can be calculated using Equation 6-5:

$$\bar{U}_j(x,y,\omega) = \sqrt{\sum_{n=1}^{3}\left|U_{j,n}(x,y,\omega)\right|^2} \quad [6\text{-}5]$$

In order to identify regions of contracting tissue and to suppress static regions within the image, a correlation map $\hat{S}$ is calculated according to Equation 6-6 below [110]:

$$\hat{S} = \frac{1}{N}\sum_{j=1}^{N} \overline{U}_j S_j - \frac{1}{N^2}\sum_{j=1}^{N} \overline{U}_j \sum_{j=1}^{N} S_j \; ; \; S = \begin{cases} 0, \; for \; systole \\ 1, \; for \; diastole \end{cases}, \qquad [6\text{-}6]$$

where, N is the total number of the cardiac phases scanned and S is a step function determined by observing the duration of systole and diastole. The vibration amplitudes caused by a mechanical wave propagating in tissue depend (among other things) on the tissue stiffness [111]. Therefore, the expected amplitudes will not change over the cardiac cycle in regions that do not contract and Equation 6-6 yields 0 for such a scenario. Thus the correlation map $\hat{S}$ compensates for the intensity of the unmoved region, and enhances the intensity of the region affected by both external mechanical vibration and the intrinsic contraction/dilation.

We examine correlations of cardiac phase and spatial averages of both wave inversion derived cardiac stiffness and shear wave amplitudes using three distinct ROIs. A semi-automatic ROI selection code is written in order to generate these ROIs for each cardiac phase. Three masks are generated in preparing the ROIs. A Mask #1 is automatically generated from the intensity of the MR magnitude images at each cardiac phase. A Mask #2 corresponds to the overall excitation affected map by adding up the wave amplitude images (Equation 6-5) of all cardiac phases. The correlation map $\hat{S}$ obtained from Equation 6-6 defines the two-dimensional Mask #3. Finally, the ROIs used for spatial averaging are defined as follows:

ROI 1: The LV manually selected from Mask #1.

ROI 2: The intersection of ROI 1, Mask #2 and Mask #3 using interactively selected thresholds to ensure sufficient wave energy and the inclusion of parts of the myocardium that are contracting.

ROI 3: The upper part of ROI 2 close to the source of the mechanical excitation.

See Figure 6-4 and Appendix Figure 4 for an illustration of the ROI selection steps.

6.3 Results

6.3.1. Implementation and Representative Image Results.

Individual MRE results shown in this section are primarily represented by experiments on mouse #5. Figure 6-1c and d show the comparison of the wave amplitude map of an MRE scan (Figure 6-1c) and its corresponding control scan without external actuation (Figure 6-1d) at the same cardiac phase (at ES). The figures are transparently overlapped with the magnitude image in order to identify the location of the left ventricle. From these figures, it can be observed that the excitation impacts the entire mouse body, and the red region indicates that the most affected area covered at least half of the left ventricle and was stronger in the region close to the actuation source.

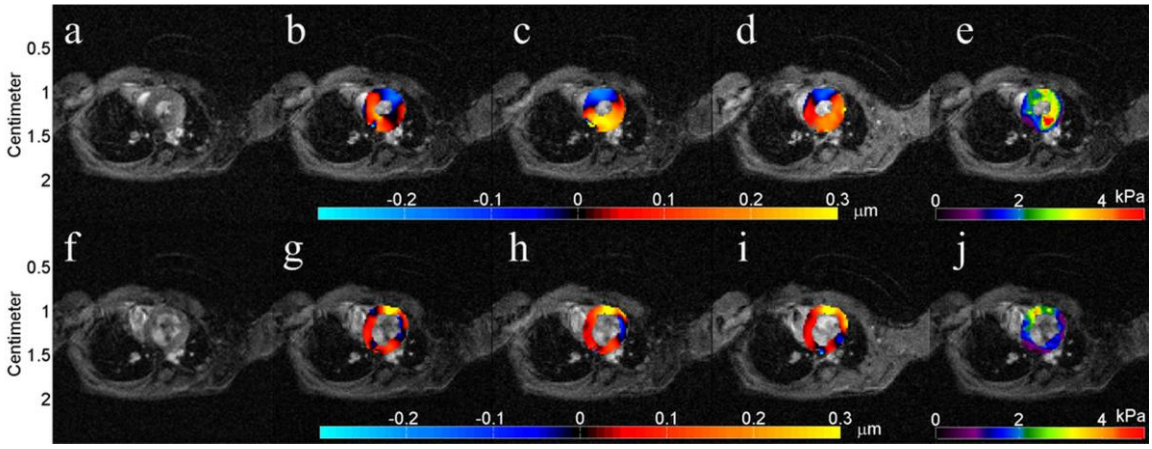

Figure 6-3: A typical cardiac MRE scan result of the left ventricle. (a-e) shows the result at the end of systole (ES), where (a) is the magnitude image, (b-d) are the wave images at the three motion directions of vertical, horizontal and out of plane respectively, and (e) is the stiffness map of the left ventricle. (f-j) shows the result at the end of diastole (ED), where (f) is the magnitude image, (g-i) are the wave images at the three motion directions and (j) is the stiffness map of the LV.

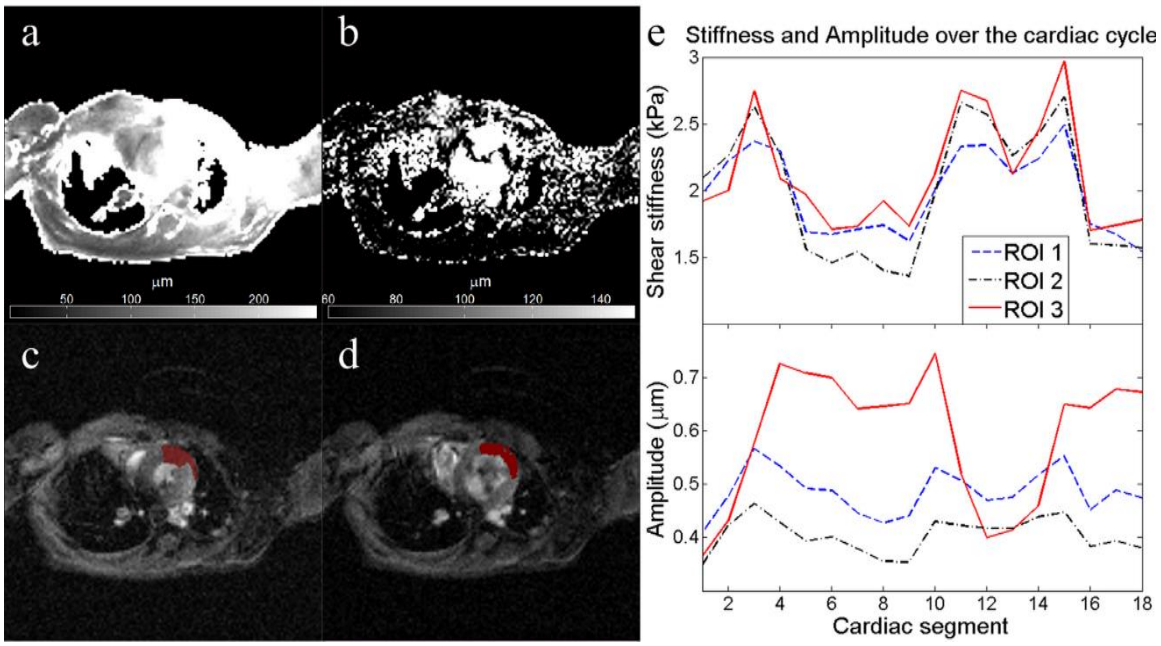

Figure 6-4: a) The overall excitation affected map, which is the summation of the wave amplitude images of all cardiac phases; b) the correlation map generatated from equation ***Error! Reference ource not found.***; c) ROI 3 at end-systole; d) ROI 3 at end-diastole; e) the stiffness and wave amplitude change during the 18 cardiac phases (covered ~1.5 cardiac cycles) averaged over the ROIs: ROI #1: the entire LV; ROI #2: the full correlated region; ROI #3: the upper region of ROI #2, which was close to the chest.

The results of the same MRE scan above are given in Figure 6-3. Figure 6-3a and Figure 6-3f are the magnitude images at end-systole (phase 3) and end-diastole (phase 9). Figure 6-3b~d and Figure 6-3g~i are the corresponding wave images for vertical, horizontal and out of plane motion-encoding directions, respectively. Figure 6-3e and Figure 6-3j are the corresponding stiffness maps. An ROI of the entire left ventricle (ROI 1) was applied to the wave images and the stiffness maps and then overlapped on the magnitude images. All of the wave images use the same displacement scale, and motion can be observed in all of the three directions. This MRE scan has 18 cardiac phases and covered ~1.5 cardiac cycles. The curves of averaged stiffness and the wave amplitude over the three ROIs of each cardiac phase are given in Figure 6-4e. It can be observed that the LV stiffness increased during systole, and decreased during diastole with variations at a

lower level during either of the two intervals of the cardiac cycle. Phase 3 and phase 14 were considered end-systole and phase 9 was considered end-diastole. Figure 6-4a~d illustrates the selection process of ROI 2 and ROI 3. Figure 6-4a gives the overall excitation-affected map of the MRE scan. The bright area shows the most affected region during the entire cardiac cycle. The region started from the upper chest, close to the excitation source, and spread into the body along the direction of the excitation, and covered at least half of the left ventricle. Figure 6-4b is the correlation map generated from Equation 6-6. The high intensity correlation area covered most of the left ventricle and separated the left ventricle into two regions, upper and lower. From that ROI 2 was calculated as outlined in the methods section and ROI 3 represented the upper region of ROI 2 close to the vibration source. ROI 3 tends to be small, but it provides more accurate average amplitude. Figure 6-4c and Figure 6-4d illustrate ROI 3 at end-systole (phase 3) and at end-diastole (phase 9). The inverse proportional relation of stiffness and wave amplitude predicted by Equation 6-4 is depicted by the result of ROI 3 (solid red line) in Figure 6-4e. It can be seen that the wave amplitude decreased during systole, and increased during diastole, which is inverse to the stiffness, as expected.

6.3.2. Grouped Data and Findings

ROI 1 and ROI 3 were examined for the MRE data of all mice in the study. The average stiffness results over the two ROIs at end-diastole and end-systole are given in Figure 6-5a. A box plot of the stiffness ratios μ_{ED}/μ_{ES} along with the amplitude ratio $(U_{ES}/U_{ED})^4$ from the results of these two ROIs is shown in Figure 6-5b.

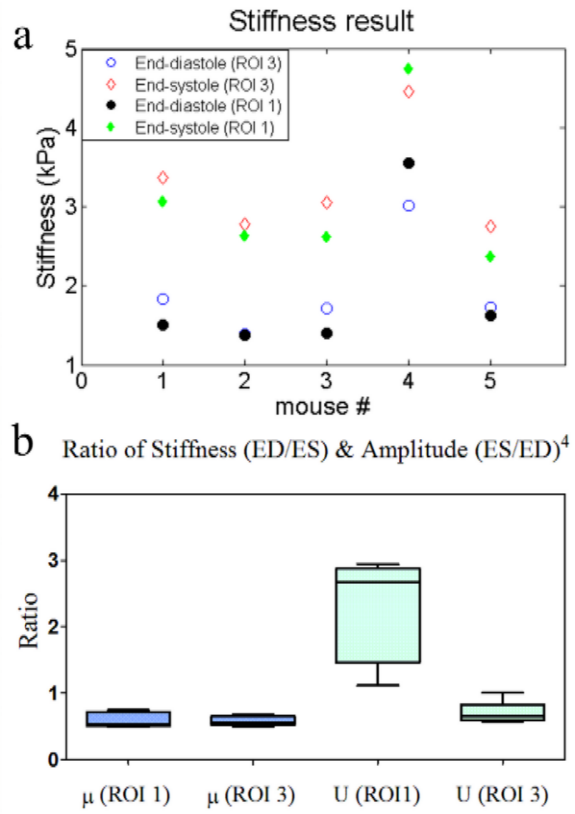

Figure 6-5: a) Plot of the stiffness at ED and ES for the five mice, with two different ROI selections; b) Boxplot of the stiffness ratio μ_{ED}/μ_{ES} of the two ROIs (entire LV and the correlated map) and the wave amplitude ratio $(U_{ES}/U_{ED})^4$ of the correlated ROI of the five examined mice.

6.4 Discussion

Cardiac MRE on humans and in porcine models has been studied by other groups with different methods (WAV-MRE by Elgeti et al. [104, 105] and WI-MRE by Kolipaka et al. [50]). However, in this study, for the first time, cardiac MRE is implemented in a mouse model and both WAV-MRE and WI-MRE processing approaches are applied. Our results suggest that the methods are useful for noninvasive detection of myocardial stiffness changes in the mouse and may therefore be valuable tools for monitoring cardiac disease progression and for testing therapies in mouse models of cardiac diseases.

Implementation of cardiac MRE on a mouse model is more challenging than on human or porcine models. The small size of the mouse body as well as the heart requires a relatively high frequency excitation. And, the small dimension of the preclinical MR scanner RF coil limits the available space for actuation setup. Multiple approaches with different excitation methods have been tried in this study, including using a piezo stack shaking a mouse bed with the mouse on it, or using a piezo stack driving a bent plastic rod to apply shear excitation directly to the mouse chest. Those approaches either could not provide enough excitation to the mouse heart or were harmful for the mouse. The custom-designed pneumatic system presented in this study provided the best excitation and least harm to the mouse. This design has also undergone multiple improvements for mouse comfort and excitation efficiency.

Also, frequency limits of this system imposed the need for a decoupling of TR and vibration period, which we successfully implemented in a modified fractional encoding pulse sequence. After removing the restriction of the vibration frequency, finding a workable excitation frequency is another factor that needs to be considered in this implementation. The small dimension of the mouse and the heart requires a high frequency excitation; however, high frequency vibration suffers from high attenuation with distance of penetration. Pre-tests with frequencies of 350 Hz, 400 Hz, 500 Hz, 800 Hz, and 1 kHz were conducted, and finite element simulations with different frequencies were performed as well in this study (not shown in here). The results showed the attenuation was too high in the region of interest at the higher frequencies; this led us to choose 400 Hz.

The ROI selection method in this study can more efficiently generate a reasonable ROI. The promising results of this study demonstrate the feasibility of MRE on the mouse heart. The stiffness of the left ventricle increased during systole, and decreased during diastole. And, the stiffness ratio matched the amplitude ratio to the power of 4 well when considering the correlated ROI 3.

However, limitations still exist in this technique. If heart rate varies greatly among the three scans, the cardiac phases at each of the three acquisitions will be unmatched, which could potentially bias the stiffness estimates. Furthermore, cardiac mouse MRE is restricted to single slice acquisitions due to the elongated scanning time with ECG and respiration gating at the current stage of development. The restriction to a 2D plane is in contrast to the need for analyzing displacements along all three dimensions because of wave refraction and reflection within the torso. The approach of using a weighted sum of the complex shear moduli derived from 2D scalar wave field inversion has yielded reasonable results in the presented study. However, a more accurate algorithm should be derived in future studies.

Finally, the ROI selection is essential, especially with regard to the WAV-MRE processing approach. From the comparison of stiffness and wave amplitude over the three ROIs in Figure 6-4e, it can be observed that the wave amplitude curve only matches the trend of stiffness in ROI 3, while the stiffness keeps the same trend for all of the three ROIs, although has differences in values. Further, Figure 6-5e illustrates that similar ratio values for amplitude (4^{th} power) and stiffness as required by Equation 6-4 are only obtained when using ROI 3. Thus, appropriate ROI selection is critical. A smaller area ROI with the same wave energy level within the fully correlated ROI provides a more accurate result, which especially holds for the wave amplitude-based approach.

In summary, this study demonstrates the feasibility of cardiac MRE on a mouse model, and provides the possibility to use cardiac MRE in exploring more applications in cardiovascular disease studies.

6.5 Acknowledgment

This work was supported by NIH grant R01HL113057 (E.D.L.).

7. IN VIVO CARDIAC MAGNETIC RESONANCE ELASTOGRAPHY ON MYOCARDIAL INFARCTON MOUSE MODEL

7.1 Introduction

The feasibility of *in vivo* cardiac MRE on a mouse was demonstrated in the last chapter. In order to examine the application of this approach to a pathology study, MRE was conducted on a myocardial infarction (MI) mouse model. MI is commonly known as a heart attack and occurs when myocardial ischemia exceeds a critical threshold [112]. As a relatively easily obtainable cardiovascular disease (CVD) animal model, the MI mouse model was selected for examination of in vivo cardiac MRE. Six MI mice and five sham-operated mice were prepared. All of the MI mice and two of the sham-operated mice had the MRE scan. Ultimately, the data acquired from this study are considered unreliable for MI assessment as mice were not imaged until too much time had elapsed since their surgery; however, the data and experience of the study are still informative, and will be helpful for future studies.

7.2 Methods

7.2.1. Animal Model Preparation

In this study, 11 female adult mice C57BL/6 (20-25 g) were separated into two groups: MI mice and sham-operated mice. The MI mice (n=6) were subjected to coronary artery ligation [113]. In this procedure, the mice were anesthetized with isoflurane, a left thoracotomy was performed in the fourth intercostal space. The pericardium was ruptured and the left anterior descending coronary artery was ligated. The chest was then closed in three layers. The mice were then allowed to recover until ambulatory. The sham-operated mice (n=5) underwent an identical surgical but the wound was closed directly after the pericardium was ruptured, without the ligation.

The experiments conformed to our university Animal Care Committee (ACC) principles, and all the procedures were approved by the university ACC committee.

7.2.2. Magnetic Resonance Elastography Experiment

Magnetic Resonance Elastography scans of the MI mice were performed in the 6th week after the surgery, and the sham-operated mice were scanned in the 7th week after the surgery. The MRE experiment setup was same as the setup in the feasibility study described in section 6.2.1. The mice were initially anesthetized with 5% vol. isoflurane in 1-liter oxygen flow for 3 min and then were placed supine in the cradle and kept anesthetized with inhaling of 1-1.5% vol. isoflurane at 1-liter oxygen flow. The hair of the mouse chest was removed and a customized tube tip was placed gently on the chest as a passive actuator, shown in Figure 7-1. The other end of the tube tip was connected to an audio speaker (11829BT, Electro Voice, MN, USA) via several rigid PVC pipes. The right front paw and left back paw were connected to ECG leads. A respiration pillow was placed and taped on the abdomen area. Rectal temperature was monitored to control an air heating system (SA Instrument, Inc. NY) regulating the body temperature of the mouse at $37°C$.

The MRE experiments were performed on a 9.4 Tesla Agilent (Santa Clara, CA) horizontal bore preclinical MR scanner, with a self-shielded gradient coil (maximum strength 100 Gauss/cm) and a 39 mm diameter birdcage quadrature RF coil. The pulse sequence applied in this study is same as in the feasibility study. A gradient echo fractional encoding cine pulse sequence, which decoupled the frequency relation between the ECG and mechanical vibration, was applied. The excitation was triggered after the ECG trigger, and 20 ms forerun was allowed for each MRE acquisition. Acquisitions of 18 cardiac phases were performed with the mouse heart beat rate above 400/min, depending on the average heart beati rate for each mouse after its rectal temperature reached at least 35 $°C$ and was stable under anesthesia. The three MRE acquisitions for each mouse were performed with the heart beating variance within 20~40 beats/min depending on the heart beat rate.

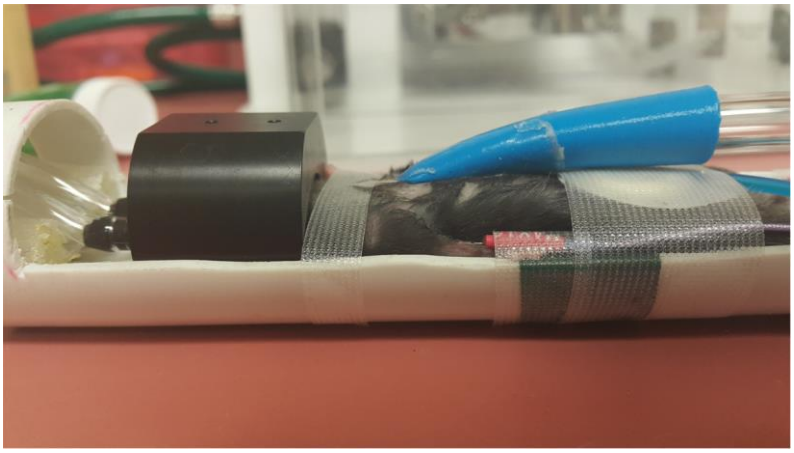

Figure 7-1: The mouse setup with the customized nose cone. The hair of the mouse chest was removed and a 3D printed tube tip was placed gently on the mouse chest.

Multi-slice, fast spin echo scans on the coronal, saggital and short-axis plane were acquired in order to identify the infarction area. A single slice of short-axis was selected crossing the infarction area. Unfortunately, the infarction area was not able to be identified in some mice. Other scan parameters include: FOV = 2.5x2.5 cm, matrix = 128x128, flip angle = 20°, TR/TE = 11.66 / 2.254 ms, slice thickness = 1 mm, 2 averages. The frequency of the MEG is 1 kHz, and the mechanical vibration frequency is 350 Hz, because the mouse ECG was found to be disturbed at 400 Hz vibration.

Motion on the three directions was acquired separately in three scans. Due to the pathological Q wave [114], the ECG leads were connected in the opposite connections, and the scan was triggered at Q peak instead of R peak. Disturbance of the ECG was also found at 400 Hz, the vibration frequency used for the feasibility study. So 350 Hz was chosen as the mechanical vibration for the MRE experiments, and the MEG frequency was 1 kHz, same as the feasibility study. The snapshot of the ECG for an MI mouse (ID#39) is given in Figure 7-2.

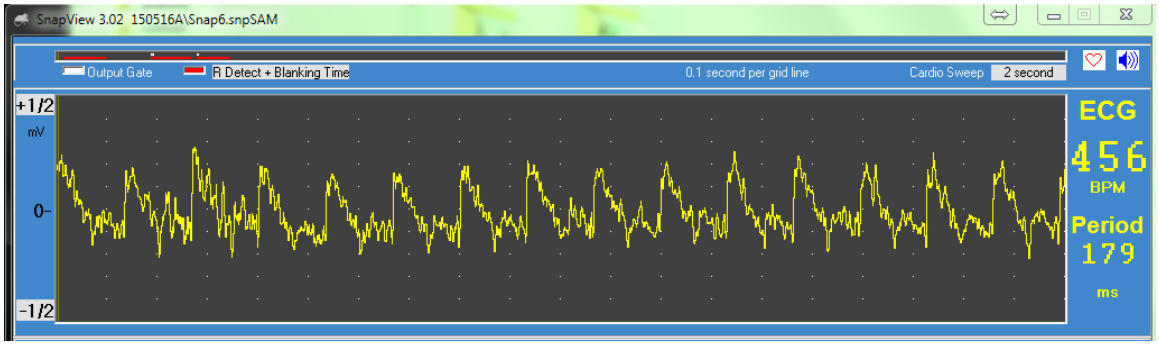

Figure 7-2: Snapshot of the ECG triggering of one mouse, the ECG leads were connected oppositely so that the Q peak was used as the scan trigger.

From the ECG snapshot in Figure 7-2, the ECG signal of the MI mice was too weak to be clearly distinguished from the disturbance caused by the MR scanner, the threshold of the ECG detection was manually adjusted to a sensitive range and thus elongated the scanning time.

Using the same method developed for the feasibility study, the effective stiffness map combining the motion of three orthogonal directions was applied in this study. The ROI was obtained the same way as in the feasibility study, with ROI#1: LV and ROI#2: correlation map. For the MI cases, a new ROI of the infarct region should be drawn to estimate the stiffness. By observing the myocardium motion in all the cardiac phases, a region of the left ventricle that has the least motion was masked manually, and by doing Boolean operation with the ROI of the LV and the excitation affected map, the ROI#3, MI region can be obtained.

7.2.3. Histology

The hearts of the MI mice were harvested immediately after the MRE scan for infarction size estimation. The procedure of euthanasia and perfusion follows the ACC approved mouse scanning protocol (ACC 10-188), and the procedure of infarct size estimations follows the article by Bohl et al. [115]. Ideally, the final infarct size is expressed as the ratio of area of necrosis (AON) to the area at risk (AAR). Thus, gross histological double-staining technique, a gold standard in

many studies, was used for the staining in this study. In this method, perfusion with a vital dye (typically Evans blue) was done following a regular perfusion with buffer in order to have the coronary artery re-occlude before the vital dye. The procedure stains the remote myocardium but not the AAR. Therefore, triphenyltetrazolium chloride (TTC) staining is necessary in order to stain the nonviable myocardium within the AAR in the second staining. With TTC staining, the nonviable areas remain unstained and the viable cells stain red. As a summary of this double-staining technique, the remote area will stain blue (with Evans blue), the AAR would be the non-blue area, and inside the AAR, the AON would be unstained and pale, and the rest area of AAR would stain red.

The mice were heparinized (50 U/10 g, IP) and anesthetized (ketamine, 80 mg/kg, plus xylazine, 12 mg/kg, IP). Hearts were excised after the mice had no response to the pinch test, and gently perfused in retrograde fashion with modified Krebs–Henseleit buffer (118.5 mmol/L NaCl, 4.7 mmol/L KCl, 1.5 mmol/L CaCl2, 1.2 mmol/L MgSO4, and 1.2 mmol/L KH2PO4) maintained at 37 ℃, equilibrated with 95% O2/5% CO2, and containing 0.4 mmol/L unlabeled palmitate complexed to albumin (3:1 molar ratio), until the eluate drains clear from the coronary sinus [116].

The heart was then lifted up and placed on the surgical pad. Several photos were taken from all angles as an alternative infarction size estimation. The heart was then placed back in the petri dish filled with clean Krebs-henseleit buffer for staining.

Evans blue, a water-soluble vital dye, was used to stain the heart. A 5% (wt/ vol) stock solution was made up of 0.9% NaCl and pigment powder (Evans Blue, E515-25, Fisher Scientific, NJ, USA). Aliquots were filtered (0.22 μm, MILLEX ® -MP, Merck Millipore Ltd,. Germany) immediately before use. The cannula and syringe were carefully filled with dye, and the heart was gently perfused with ~250 μI. The procedure were tried to be done while the heart was still beating. Unfortunately, due to the severe heart condition of the MI mice, only two hearts were kept beating during the perfusion.

The intact heart was then weighed, and wrapped in cling film, placed in an Eppendorf vial, and stored in freezer for around 30 minutes, until the heart was semi-frozen. The semi-frozen heart were then sliced into 5 ~ 7 parallel short-axis sections on a cold surface, with a razor blade. The heart sections were then immersed in freshly prepared TTC staining (1% vol/wt) in 0.9% NaCl; 2,3,5-TTC MP Biomedicals, LLC, France) at room temperature for 2 to 3 minutes. The vial was then transferred to a water bath at 37° for 15 minutes.

The sections were then removed from the vial and have the excess moisture blotted. The samples were then placed in 10% neutral-buffered formalin (Sigma-Aldrich Inc, MO, USA) for ~15 minutes to enhance the red/pale contrast between viable AAR and AON.

A microscope and an adjustable fiber optic light source were used to observe the staining result, and a camera was used to take pictures of the heart sections through the microscope. The heart sections were blotted on tissue paper for excess moisture and photographed from both sides. The size of the infarct area can be estimated from two methods: observation from the picture taken of the entire heart or observation from the stained heart size.

7.3 Results

7.3.1. Myocardium Infarction Mice

7.3.1.1. Magnetic Resonance Elastography Result

Six MI mice were scanned with MRE, but waves were successfully induced into the left ventricle only in two mice (ID#37 and ID#39), because the heart position was changed after the surgery and the wave was reflected by the blood in the right ventricle, which will be discussed later. Figure 7-3a~c and Figure 7-3e~f are the wave images on the three motion directions of these two mice where the wave motion was successfully induced. Wave motion was successfully propagated into the left ventricle, and can be observed in all three directions. Figure 7-3d and Figure 7-3h are the corresponding excitation effective maps, which is the summation of the wave amplitude image

of all cardiac phases. It can be found that the wave propagated into the left ventricle and covered around one third of the left ventricle on the right side.

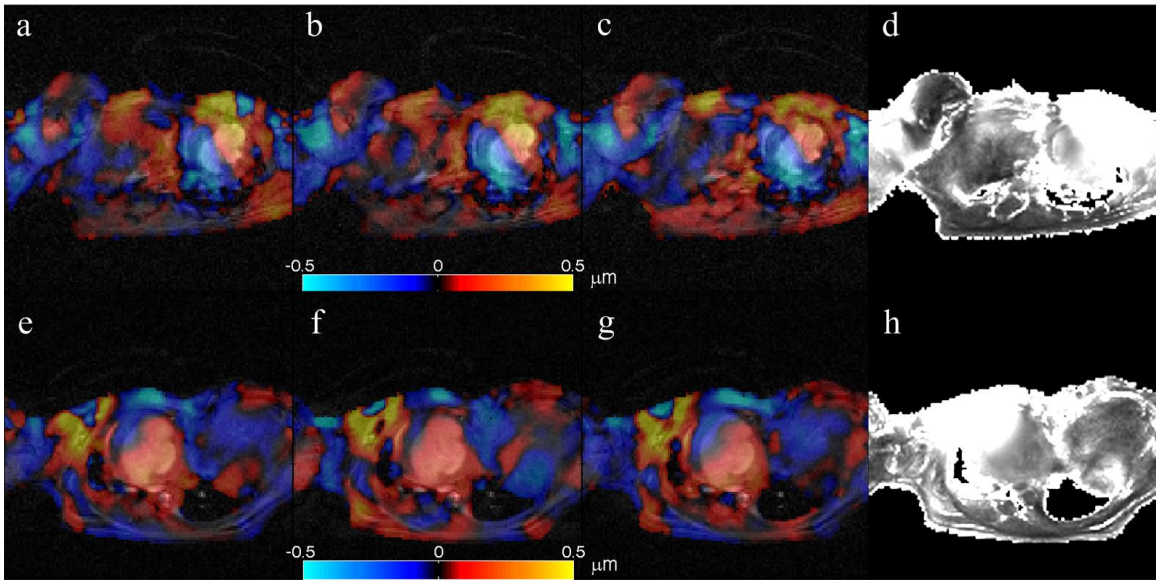

Figure 7-3: Wave images and the excitation effective maps of the two mice where the wave was successfully induced into the left ventricle. a~d are the result of mouse ID#37, and e~f are the result of the mouse ID#39. a~c) Wave image on vertical, horizontal and direction of out of plane three motion directions of mouse ID#37l d) excitation effective map of mouse ID#37, which is the summation of the wave amplitude images of all cardiac phases; e~f) wave images of the mouse ID#39; h) excitation effective map of mouse ID#39

From the magnitude image of the MRE scan of mouse ID#37 in Figure 7-4a, the infarct region can be observed at the top right area of the left ventricle. Figure 7-4b~d are the three ROIs on the magnitude image of this cardiac phase. Figure 7-4b is the ROI of LV, Figure 7-4c is the ROI of correlation map, and Figure 7-4d shows an example of the ROI of infarct region.

The stiffness map of the MRE scan of mouse ID#37 at the end of systole and diastole are given in Figure 7-6. The stiffness map is shown in ROI of LV. The stiffness and wave amplitude of the three ROIs over the 18 cardiac phases of the two mice is given in Figure 7-6. Stiffness and the wave amplitude changes from systole to diastole in the ROI of correlation map and infarct region.

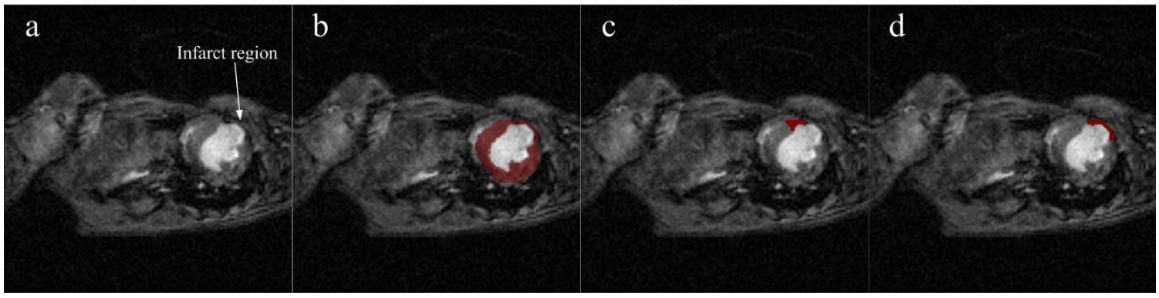

Figure 7-4: a) Magnitude image of one cardiac phase shows the infarction region is at the top right of the left ventricle; b) ROI of the left ventricle; c) ROI of the correlation map; d) ROI of the infarct region at this cardiac phase.

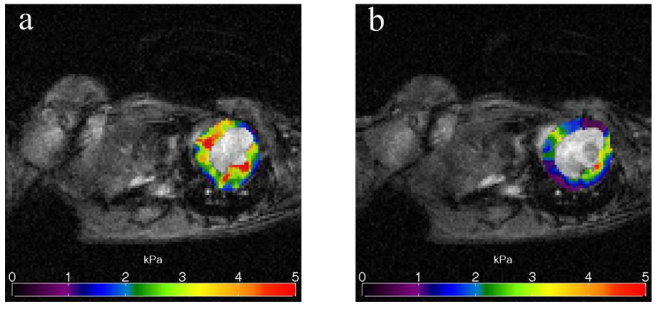

Figure 7-5: a) Stiffness map at the end of systole (cardiac phase 3) b) stiffness map at the end of diastole (cardiac phase 9).

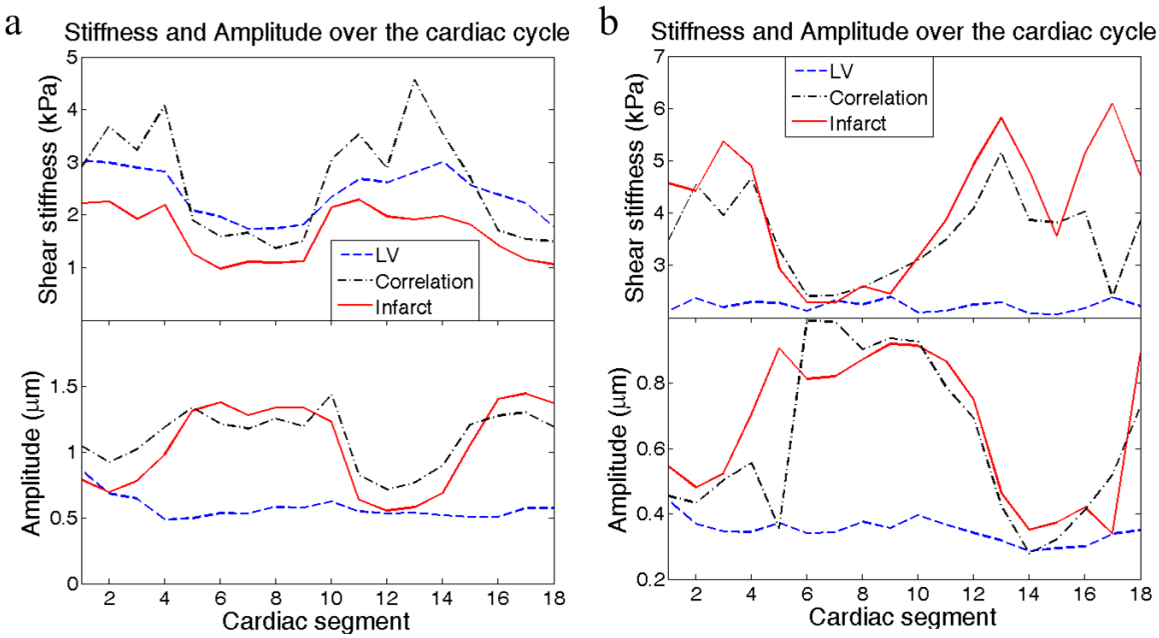

Figure 7-6: Stiffness versus amplitude of the three ROI over the cardiac phase. a) result of mouse ID#37; b) result of mouse ID#39. The stiffness and wave amplitude changes over the cardiac phase over the ROI of correlation map and ROI of infarct region in this scan.

7.3.1.2. Histology

Pictures of the entire heart with the infarct region was taken after the perfusion as an alternative method to estimate the size of infarct region. Figure 7-7 shows the pictures of the heart at different angles of mouse ID#37. It can be found by eye that a large area (~30%) are nonviable.

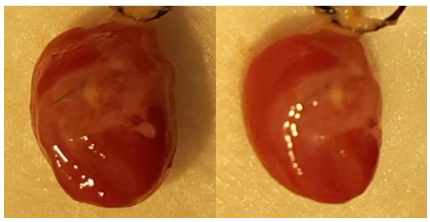

Figure 7-7: Pictures of the entire heart with the infarction region of the same mouse. The infarct region can be observed clearly by eye.

Figure 7-8 shows the stained heart sections of the mouse ID#37. Pictures were taken from both sides of each section (picture from one side of section 2 was missing in this figure). The stain of vital dye (Evans blue) failed and the entire remote area was not stained. The nonviable area can be found pale and unstained. Since the infarct region has lost its elasticity and was thin, it's unfair to estimate the AON size from the picture. Thus, the size of the infarct region would be estimated from the pictures of the entire heart.

7.3.2. Sham-Operated Mice

Five mice had sham-operation, two of them were scanned with MRE, and it was found that no wave propagated into the left ventricle in these two mice, due to the change position of the heart. The experiment was then ceased. The wave image on the three motion directions of one sham-operated mouse can be found in Figure 7-9a-c, and the excitation affected map is shown in Figure 7-9d.

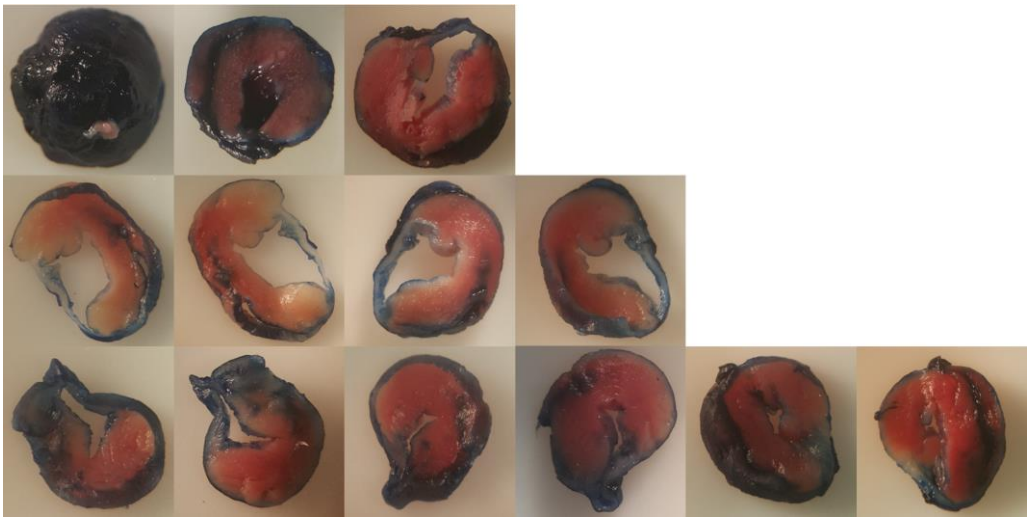

Figure 7-8: Pictures of seven stained heart sections from both sides. The mouse had surgery six weeks ago; a large region of the left ventricle was nonviable. The vital stain was unsuccessful in this mouse; thus, the remote area wasn't stained. And the nonviable can be found pale in these pictures.

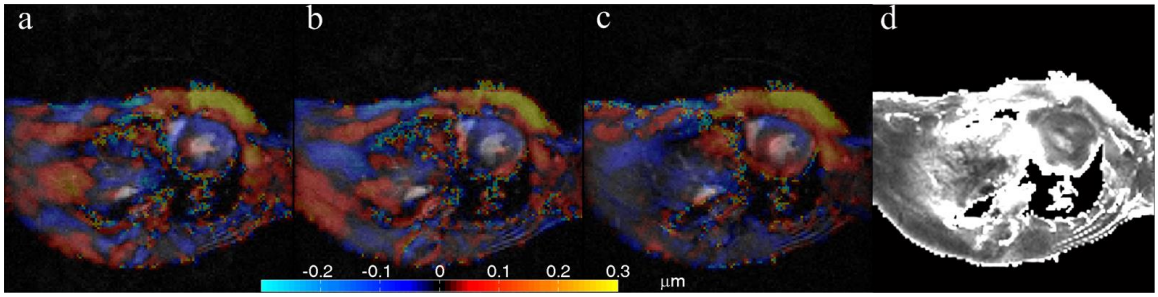

Figure 7-9: a-c) Wave images on three motion directions for one sham-operated mouse. Wave wasn't able to propagate into the left ventricle. d) Excitation affected map of the same scan.

7.4 Discussion

In myocardial infarction, the infarct region loss elasticity due to the loss of contractile mass, and scar formation would be induced which would result in adverse LV remodeling and subsequent severe dysfunction. However, when examining the left ventricle stiffness change in MI, conflicting results of the left ventricular compliance after myocardial ischemia have been reported to be both increased and decreased [117-119]. A group at the University of Tucson has done a follow up study in rat after the coronary artery ligation to determine the time courses of changes in left ventricular diastolic properties [117], and found out the LV diastolic functions in the rat are dynamic during the acute and healing phases of MI. The changes in LV chamber stiffness are biphasic; the stiffness constants were increased at 3 and 24 Hr, and returned to normal at 3 days after coronary artery ligation. At more than 22 days, the stiffness constant for low filling pressure was decreased [117]. Thus, it would be interesting if we can use MRE to estimate the stiffness change of the LV and the infarct region in MI model.

This study failed because the MRE scan was not done in the correct time frame (10 days after the surgery) and the mouse model had become a completely different model. Several lessons can be learned from this failed study. First of all, the surgery date should be scattered for each mouse. The scanning time of MI mouse was longer than scans on normal mouse because the ECG

trigger threshold has to be sensitive due to the pathological Q wave and the weak ECG signal. Therefore, in order to make sure the scan is done in the correct time frame after the surgery, the time table of the surgery and scan should be scheduled carefully.

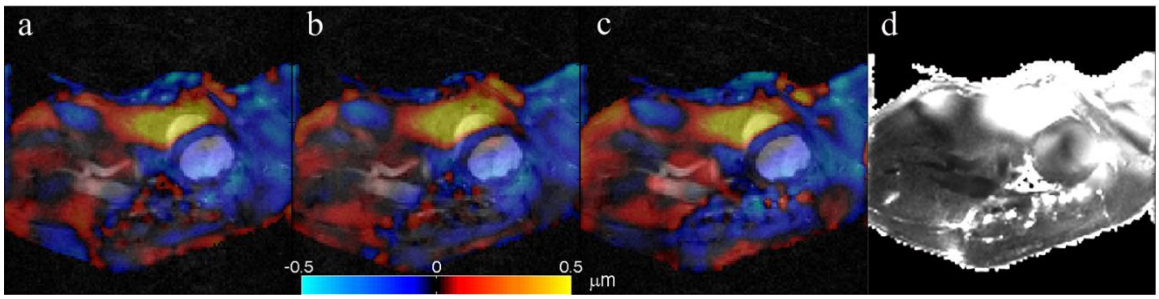

Figure 7-10: a-c) Wave images on three motion directions for a MI mouse (ID#49), which the wave failed to propagate into the left ventricle. d) Excitation affected map of the same scan.

Additionally, the pericardium, a connective tissue holding the heart in place inside the chest, was removed in both MI and sham-operated mice. The heart position then changed because of activity of the mouse after the surgery. In this study, several mice had the right ventricle facing the chest, and several mice had the coronary artery facing the chest. The blood in right ventricle or atrium reflected almost all the incoming waves, so that the wave could not induced into the left ventricle. Figure 7-10 is a typical example of a mouse (ID#49) with the right ventricle facing the chest in the MI group.

Finally, for the MI model, identifying the infarct region in the MRI scan for ROI determination is also important. In this study, the infarct region was identified by observing the region that had the least motion. However, when doing experiments at earlier stage of infarction, the motion of the infarct region might be more than it in this study. Thus, how to identify the infarct region is MRI needs to be considered, as well.

In summary, although this study failed, knowledge gained from the experiments should benefit future attempts.

8. CONCLUSIONS AND PERSPECTIVES

8.1 Summary and Contributions

The ultimate goal of this study is to develop an MRE technique to estimate the stiffness of the mouse heart, a special organ for which the stiffness changes during the cardiac cycle. Developing this technique is challenging due to the fast heart beating and respiration rate of the mouse, and the small dimension of the mouse heart. Thus, a series of pilot studies were done in silico and on phantoms before the costly cardiac MRE on experiment on the mouse.

Aim 1: The extended phantom study on the feasibility of MRE in viscoelasticity estimation in Chapter 3 not only explored the upper frequency limit of the soft tissue-like silicon gel in MRE, but also compared the performance and parameters of different integer order and fractional order viscoelastic models in representing soft tissue over a broad spectral band. This study demonstrated novel approaches in estimating viscoelastic parameters (which were also used in later Aims), and further justified the superiority of fractional over conventional integer order viscoelastic models in representing soft tissue-like materials.

Aim 2: The shell phantom study in Chapter 4 examined the wave propagation behavior in a shell geometry with fluid inside, mimicking the left ventricle. Reflection can be observed from the obtained wave images. By processing the wave images with different inversion algorithms, trying different numbers of directional filters and looking for an appropriate and efficient number of directional filters, this study provided useful information in selecting the directional filter and appropriate inversion algorithm for the in vivo cardiac MRE in later aims.

Aim 3: Finding an effective actuation method that can induce reliable excitation is, perhaps, the most challenging part of cardiac MRE in the mouse. Computational simulations in Chapter 5 on a 3D mouse thorax region were performed to examine the wave propagation behavior under different excitation methods in order to save the cost of numerous MRE experiments. The simulation results demonstrated how deep the wave can propagate into the mouse body, and how

large of an area in the left ventricle can be affected under each actuation method and vibration frequency. All of these results provided useful information, and saved time and cost in the *in vivo* cardiac MRE experiment.

Aim 4: The feasibility of in vivo cardiac MRE on mouse was proven and demonstrated in Chapter 6. Promising results successfully showed the stiffness change of the left ventricle during the cardiac cycle. For the first time, we compared the corresponding relation between the wave amplitude and stiffness over a reasonable ROI during the cardiac cycle. To our best knowledge, this is the first study applying MRE on a mouse heart. There are several innovations in this study. First of all, an excitation setup was developed that can induce an acoustic wave into the mouse heart effectively. Secondly, a pulse sequence was developed that decoupled the relationship between the frequencies of the mechanical excitation and the MEG in a fractional encoding method. This made it possible to use a frequency that is high enough to show at least one wavelength in the mouse and low enough to have the wave penetrate into the left ventricle, and maintain the TR long enough to overcome the long T1 under high magnetic field and thus kept a decent SNR of the image. Finally, an effective stiffness map generation method was developed based on a 2D direct inversion algorithm, which considered the motion on all directions when waves propagate in such a complicated geometry.

Aim 5: An extended study of applying *in vivo* cardiac MRE technique on a myocardial infarction mouse model in Chapter 7 failed primarily due to failing to scan the mouse at the appropriate time after surgery. However, the data still provided useful information if this type of study were to be conducted in the future.

8.2 Limitations

A few limitations of the studies in this dissertation should also be mentioned:

Aim 1: The feasibility of MRE in viscoelasticity estimation is demonstrated, and the fractional Voigt model was proven to have a best convergence. However, this model requires a

static stiffness value to be measured for the curve fitting, which is impossible in the *in vivo* study. Putting the static stiffness as an unknown parameter in the curve fitting can compromise this shortage in some way, but adding an unknown parameter will not only increase the estimation time, but also would potentially decrease the accuracy in the estimated result. On the other hand, the frequency range in clinical application is much narrower than the bandwidth in this study, and much lower than the frequency presented in this study. Whether estimation in such a limited frequency range would cause a big difference is unknown.

Aim 2: The shell phantom experiments provide insight of how waves are reflected at the fluid-solid boundary. However, the thickness of the left ventricle wall changes over the cardiac cycle, as well as the stiffness. Some groups have made a shell phantom with the volume of the fluid changing periodically [45]; however, the stiffness change of the wall changes in the opposite way because the pressure comes from the myocardium instead of the blood in the ventricle anatomically. So the shell phantom study can give some useful information for the *in vivo* cardiac MRE experiment, but won't be able to mimic the left ventricle unless a phantom with the same mechanics of the left ventricle can be made.

Aim 3: The simulation results reflected the wave propagation behavior in the mouse body. However, there is not enough information in the literature regarding mechanical properties of the various components within the mouse chest; so, most of the material property valued that were used were defined either by analogy to other animal models, or by assumptions based on phantom studies. Even if the material properties were measured in some cases, the soft tissue behaves differently when the mouse is in different positions or stages. So the simulations can only provide a prediction or estimation of the tissue response under excitation, but won't be able to mimic the experiment identically, and MRE experiment trials are still necessary.

Aim 4: Although a promising result has been presented, limitations exists. Since motion on the three directions should be encoded in three separate scans, keeping the mouse heart rate stable

during the scan is important otherwise it can cause misregistration of scans. Furthermore, cardiac mouse MRE is restricted to single slice acquisitions due to the elongated scanning time with ECG and respiration gating at the current stage of development, and this meant that the inversion was limited to 2D assumptions. Although the effective stiffness method presented can combine the motion on the three directions, either faster 3D motion encoding techniques or a more accurate algorithm should be derived in future studies.

Aim 5: Although this study failed, the application of the cardiac MRE on a MI mouse model showed some limitations of the *in vivo* cardiac MRE. The MRE on the sham-operated mice showed the heart position was changed during recovery after the surgery, and the right ventricle was facing the chest on the short axis scan. Due to this the wave was reflected by the blood in the right ventricle, and wasn't able to propagate into the left ventricle in some of the animals. So the failed scan showed the limitation of the in vivo cardiac MRE in that this technique is sensitive to the heart position. And one speculation of why the heart position was changed is the pericardium was removed in the operation. The pericardium is the connective tissue holding the heart in place inside the chest. Thus, in future studies, this situation needs to be taken into consideration.

8.3 Recommendations for Future Work

There are some future directions that can be considered:

Aim 1: an extended study on the clinical frequency range can be performed, to see if the result would have a big difference with the wide frequency range in this study. Also, the results of measuring the static stiffness as the parameter and treating it as an unknown parameter can also be compared for a narrow frequency range.

Aim 2: if possible, a shell phantom having similar mechanics to the left ventricle, where the stiffness and the thickness of the phantom can be altered cyclically, should be made. This would provide more useful information of the wave propagation patterns and can be utilized to improve future cardiac MRE experiments.

Aim 3: a 3D mouse model with larger region that includes the abdomen should be reconstructed, because the short axis slice can extend to the region of liver and kidney. Using a small region model as in this study, reflection appears at the bottom of the model, which does not exist in vivo. Although the wave has attenuated when it reaches to that end, a full size model can provide a more accurate simulation. Also, material properties of each organ need to be optimized. And simulations on different cardiovascular disease can also be done so that it provides more information on application of this technique in more pathology studies.

Aim 4: the technique presented in this study is limited to encoding motion in one direction on one slice in each scan. A faster 3D motion encoding technique or a faster multi-slice ECG gated scan needs to be developed in the future for more accurate scanning. Although the effective stiffness method presented can combine the motion on the three directions, a more accurate algorithm should be derived in future studies.

Aim 5: the study presented in this dissertation failed due to failing to scan at the right time after surgery. This study needs to be repeated if possible, also taking into consideration other challenging factors like the repositioning of the heart after the surgery.

APPENDICES

APPENDIX A

DERIVATIVE OF THE RELATION BETWEEN THE SHEAR STIFFNESS AND THE COMPLEX SHEAR MODULUS

When a planar shear wave at frequency f propagates in a linear, isotropic, viscoelastic medium, the exponential part of the propagating wave can be written as:

$$e^{j(\omega t - kx)} = e^{j(\omega t - k_R x)} e^{-k_I x} \quad [1]$$

where $k = k_R - jk_I$ is the complex wave number. The part $e^{-k_I x}$ represents the wave attenuation property. And the part $e^{j(\omega t - k_R x)}$ represents the wave propagation property, which derives the phase speed of the wave propagation is:

$$c_{ph} = \frac{\omega}{k_R} \quad [2]$$

For planar wave propagates in a viscoelastic material, the wave speed c has a relation with the complex shear moduls G and the medium density ρ as:

$$c = \sqrt{\frac{G}{\rho}} = \sqrt{\frac{G_R + jG_I}{\rho}} \quad [2]$$

Thus, the wave number will be:

$$k = \frac{\omega}{c} = \omega \sqrt{\frac{\rho}{G_R + jG_I}} = \omega \sqrt{\frac{\rho}{G_R^2 + G_I^2}} \sqrt{G_R - jG_I} \quad [4]$$

since:

$$G_R - jG_I = \sqrt{G_R^2 + G_I^2} e^{j\theta}, \theta = \tan^{-1}\left(\frac{G_I}{G_R}\right) \quad [5]$$

APPENDIX A (CONTINUED)

$$\cos\left(\frac{\tan^{-1}(x)}{2}\right) = \pm\sqrt{\frac{1+\cos(\tan^{-1}(x))}{2}} = \pm\sqrt{\frac{1+\frac{1}{\sqrt{1+x^2}}}{2}} \quad [6]$$

$$\sin\left(\frac{\tan^{-1}(x)}{2}\right) = \pm\sqrt{\frac{1-\cos(\tan^{-1}(x))}{2}} = \pm\sqrt{\frac{1-\frac{1}{\sqrt{1+x^2}}}{2}} \quad [7]$$

Substitute equation 5, 6 and 7 to equation 4:

$$k = k_R - jk_I = \omega\sqrt{\frac{\rho}{\sqrt{G_R^2+G_I^2}}}\left(\cos\left(\frac{\theta}{2}\right) - jsin\left(\frac{\theta}{2}\right)\right)$$
$$= \omega\sqrt{\frac{\rho}{2}\frac{G_R+\sqrt{G_R^2+G_I^2}}{G_R^2+G_I^2}} - j\omega\sqrt{\frac{\rho}{2}\frac{\sqrt{G_R^2+G_I^2}-G_I}{G_R^2+G_I^2}} \quad [8]$$

Thus, the wave phase speed is:

$$c_{ph} = \frac{\omega}{k_R} = \sqrt{\frac{2}{\rho}\frac{G_R^2+G_I^2}{G_R+\sqrt{G_R^2+G_I^2}}} \quad [9]$$

On the other hand, the shear stiffness μ obtained from Local Frequency Estimation (LFE) was calculated from the relation as below:

$$c_{ph} = \frac{\omega}{k_R} = \sqrt{\frac{\mu}{\rho}} \quad [10]$$

So the shear stiffness μ from the LFE has a relationship with the shear modulus:

$$\mu = \sqrt{\frac{2(G_R^2+G_I^2)}{G_R+\sqrt{G_R^2+G_I^2}}} \quad [11]$$

APPENDIX B

UNIVERSAL INTERFACE DESIGN FOR MRE PULSE SEQUENCE

Pulse sequence development is one of the most important part in MRE. With the development of MRE technique, there are various method to optimize the MRE acquisition as described in Chapter 2. For example, fractional encoding MRE method can use lower mechanical vibration frequency and higher MEG frequency so that to ensure a shorter TE for better SNR. SLIM MRE [65], SDP MRE[61] and ULTIMAte MRE [60] can decrease the scanning time by fully usage of gradients on all directions and the frequency information in the FFT data of the wave images. Almost all of these techniques can be developed from any MRI pulse sequence, such as gradient echo, spin echo, fast spin echo, etc.

Also, even with the same MRE acquisition method, different approach to eliminate static field inhomogeneity can be applied. For example, most group eliminate the gradient noise by subtracting phase images from opposite polarization of MEG [8], some group subtract the phase image of the scan with the excitation turned on and the "baseline" image acquired with the excitation turned off [120]. And in the *in vivo* Cardiac MRE on mouse technique presented in this dissertation Chapter 6, phase images acquired with relative trigger shifts of $\frac{\tau_v}{2}$ were subtracted to reduce the scanning time.

Furthermore, different MEG shape can be applied for almost all MRE experiment. Sinusoidal and trapezoidal shape are the two most popular MEG shape, flow compensate gradient shape is good for imaging organs have blood flow so that it can filter out the flow velocity because of 1st gradient moment nulling technique.

Any combination of the MRE acquisition method, static field inhomogeneity elimination approach and MEG shape can be utilized during the research stage of MRE. Develop pulse sequence for each combination will not only increase the effort to develop different pulse sequences, but will also increase pulse sequence number, and potentially confuse the user. So in

APPENDIX B (CONTINUED)

this dissertation, an optimized universal interface of MRE pulse sequence was developed, which combined all of the MRE techniques would be used in our current MRE research, and makes the MRE pulse sequences clean and also makes the development of MRE pulse sequence from any MRI sequence more efficiently.

Since most of the MRE experiment in this study was done on a 9.4 Tesla Agilent horizontal bore preclinical MR scanner. The optimized universal interface was developed on VnmrJ 4.0. The pulse sequences in VnmrJ 4.0 are written in C, and it makes it possible to make the MEG shape generation to be a separate function. So that when developing a MRE pulse sequence from a basic MRI pulse sequence, we can simply call this MEG shape generation function to create MEG shapes and return the essential MEG parameters such as phase shift time and MEG duration for each phase offset. This makes the development of MEG pulse sequences much more efficiently.

In the MEG shape generation function, MEG shape files for each phase offset on each of the three gradients were generated based on the MRE method, static field inhomogeneity elimination approach and MEG shape defined from the universal pulse sequence interface. MEG duration, and the time shift of MEG on each gradient and time shift of the triggering of the synchronized mechanical excitation at each phase offset, were also calculated and returned to the main pulse sequence function.

The universal MRE interface is shown in Figure 1. Encoding type has the option of regular encoding where the frequencies of the MEG and mechanical excitation are the same, and fraction encoding when the frequencies are different. MRE type includes regular MRE, SLIM MRE and ULTIMAte MRE. The MRE parameter panel on the right would be changed when choosing different MRE type. MRE method is to choose the static field inhomogeneity elimination approach. Different MEG shape including sinusoidal and flow compensate shape can be chosen as well for each sequence. Other MRE parameter can also be defined in this interface, such as pre-run time,

APPENDIX B (CONTINUED)

actuator trigger on or off, number of MEG cycles, MEG strength on each direction, vibration and MEG frequencies, etc.

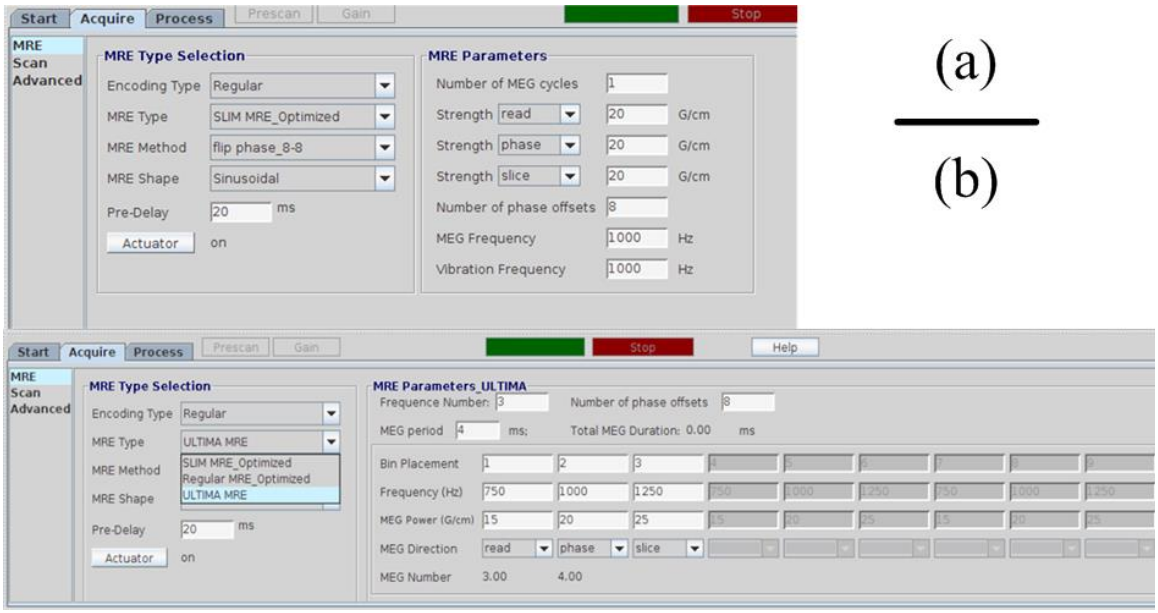

Figure 1: Interface of the MRE pulse sequence developed in VnmrJ 4.0. All the MRE methods can be selected in this universal interface, and the MEG shapes on each gradient at each phase offset can be generated correspondingly. a) the interface when choosing SLIM MRE b) the interface when choosing ULTIMAte MRE. Different MRE parameter panels will be appeared when choosing different MRE type.

APPENDIX C

MRE POST-PROCESSING TOOL: MRELASTO

Post processing is another important factor in MRE study. To make the post processing more efficiently, a graphic user interface written in Matlab was also developed in this dissertation, and the software was named as MRElasto. The compiled software is also available to download from our lab website at:

http://avl-server.mie.uic.edu/AHP/htdocs/MRElasto_downloadpage.php.

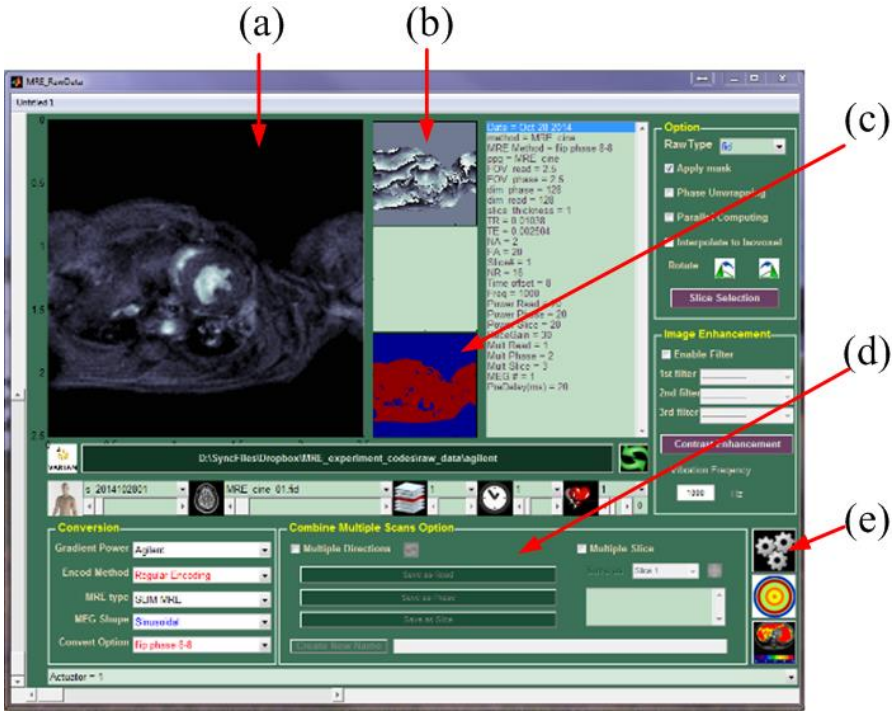

Figure 1: Raw data module of the MRElasto. With this module, we can review the MRE and MRI scans, generate mask for the scans, combine MRE scans of different motion direction encoding into one data file, and convert the MRE scans to wave images. a) displaying magnitude image; b) displaying phase image; c) displaying mask applied on the magnitude image for converting to wave image; d) buttons to select different MRE scans for combination to one single wave date; e) buttons to convert raw data to wave image.

APPENDIX C (CONTINUED)

There are four main modules in MRElasto: Raw data module, Wave image module, ROI selection module and Stiffness map module. The interface of the Raw data module is shown in Figure 1. With this module, we can review the MRE and MRI scans along with the scan parameters. We can also generate mask from the magnitude image. Also, since in some cases, separate MRE scans would be done to encoding different motion directions on one sample, we can combine the scans for different direction into one data file in this module as well. And finally, we can use this module to convert the MRE scan into wave images.

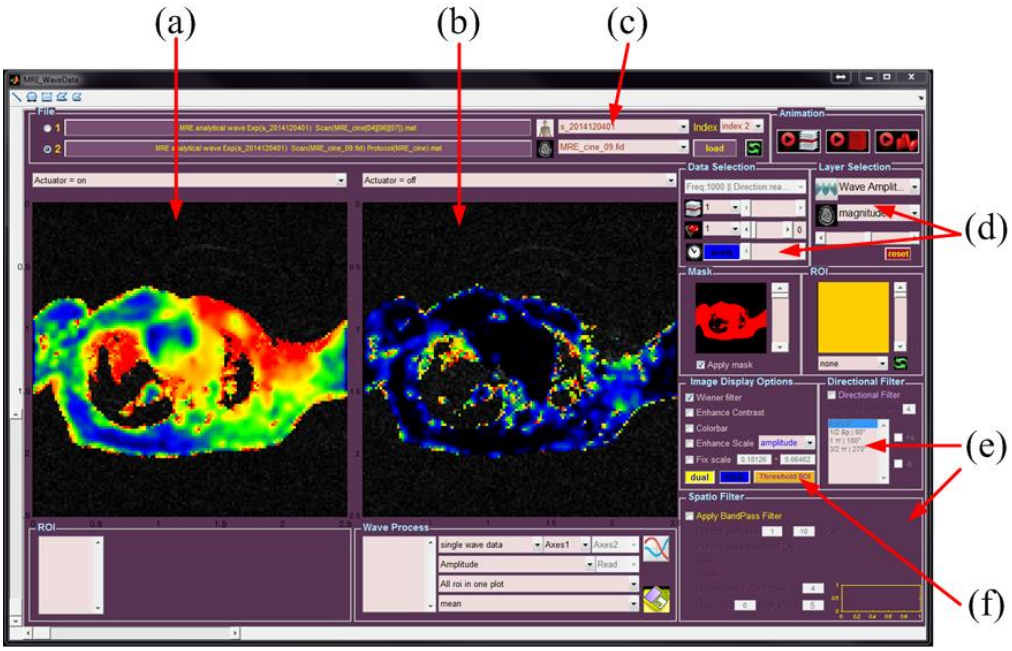

Figure 2: Wave image module. This module can compare two wave data at the same time, which is good for comparing MRE wave data with the external mechanical actuation on and off. a) and b) are displaying the wave images of the corresponding two data; c) is another option to load a data from the list of existing data in the default directory; d) are the options to show different images, such as motion on different directions, slice, cardia phase, or images of real or imaginary part of the wave, or wave amplitude of the wave data; e) is panel to apply spatial filters such as directional filter to eliminate reflection or butterworth bandpass filter to eliminate high frequency noise and low frequency compressional wave. The filtered images will be displayed in a) or b); f) button to open "ROI selection module"

APPENDIX C (CONTINUED)

The Wave image module is shown in Figure 2. In this module, two images from two different wave data can be compared together. In some experiments, especially in cardiac MRE, a control scan with the external actuator turned off is always taken, so that comparing the MRE scan and the control scan can confirm the wave is propagated into the mouse body, such as the wave amplitude images shown in the figure. In MRE, spatial filters such as directional filter and spatial filters are usually applied to eliminate the reflection, high frequency noise or low frequency compressional waves. This module also has an interactive selection of the filters, and preview the wave images with different filters.

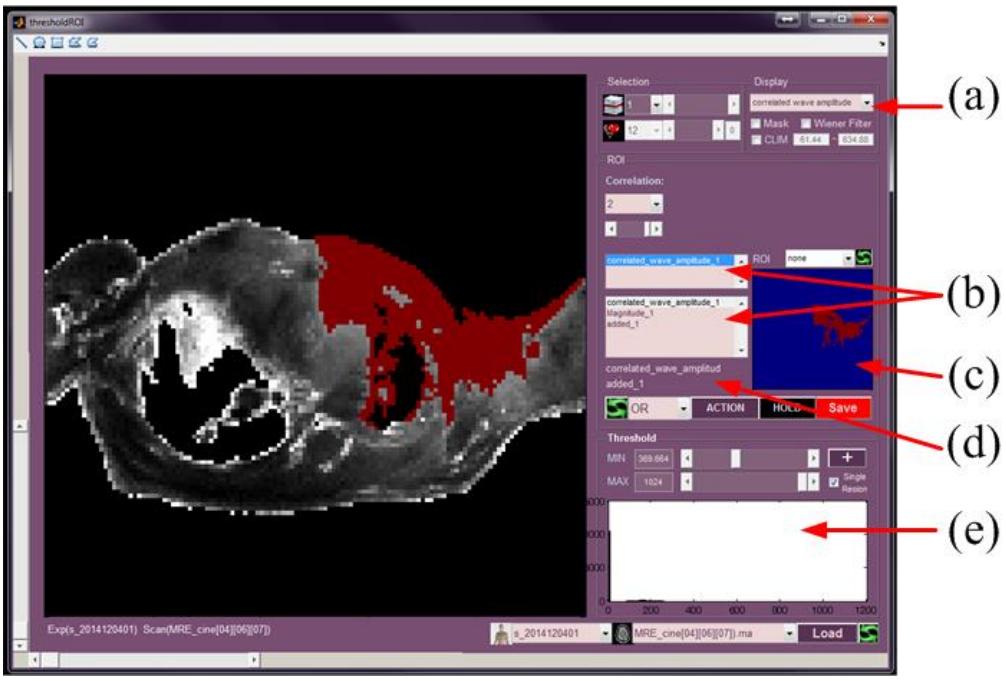

Figure 3: ROI selection module. In this module, the threshold on the intensity of the corresponding images can be adjusted interactively. And multiple masks can be pre-selected to highlight one geometry, and Boolean operations can be then applied to obtain the desired ROI. a) display options on wave amplitude, correlation map, or amplitude summation map (excitation affected map); b) list for different mask; c) geometry of the selected mask; d) Boolean operation panel; e) interactive threshold adjustment panel.

APPENDIX C (CONTINUED)

ROI selection is important in MRE data post-processing, especially in *in vivo* studies. So an ROI selection module is created in MRElato as shown in Figure 3. In this module, the mask can be semi-automatically selected by adjusting the threshold on the intensity of the corresponding image. And multiple masks can be created for each image to highlight different region. Boolean operations can then be applied on masks to obtain the desired ROI. Images including wave amplitude image, excitation affected image (summation of wave amplitude image in different cardiac phase for cardiac MRE), and correlation map (see Equation 6-6) can be displayed for mask selection. An example of how a reasonable ROI be selected in cardiac MRE is shown in Figure 4.

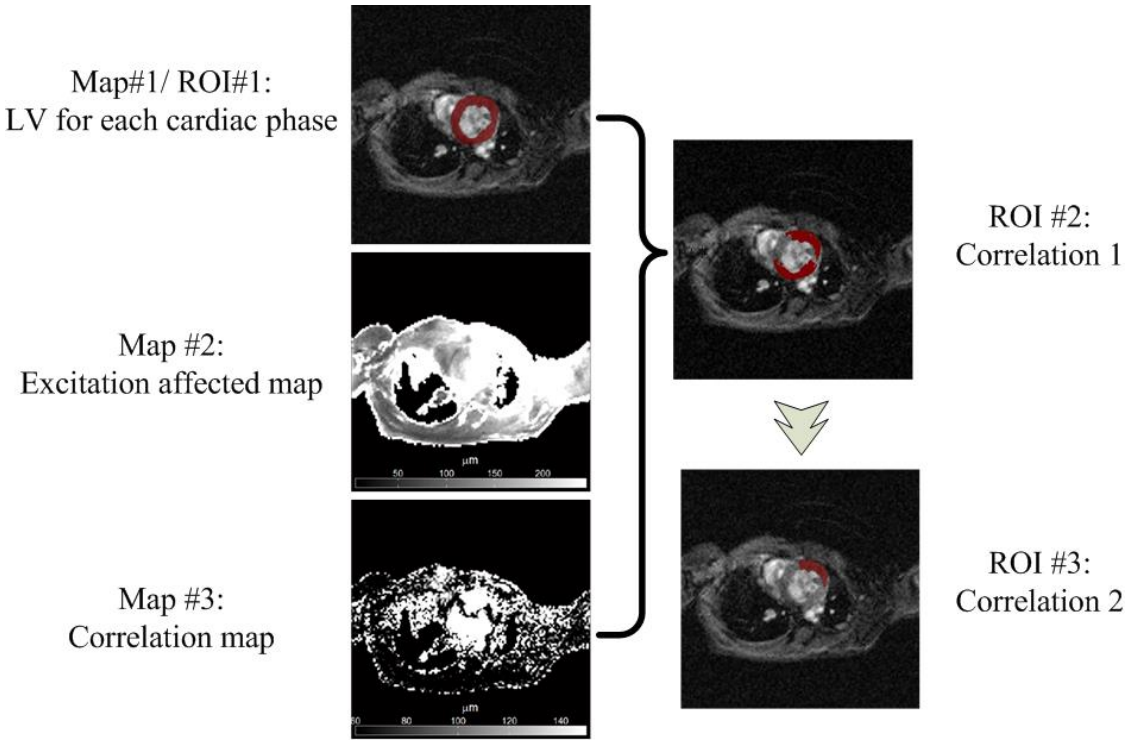

Figure 4: The ROI selection procedure of cardiac MRE technique. In cardiac MRE, three maps were obtained by adjusting the threshold of corresponding image, and a reasonable ROI can be then obtained by using Boolean operation on the maps.

APPENDIX C (CONTINUED)

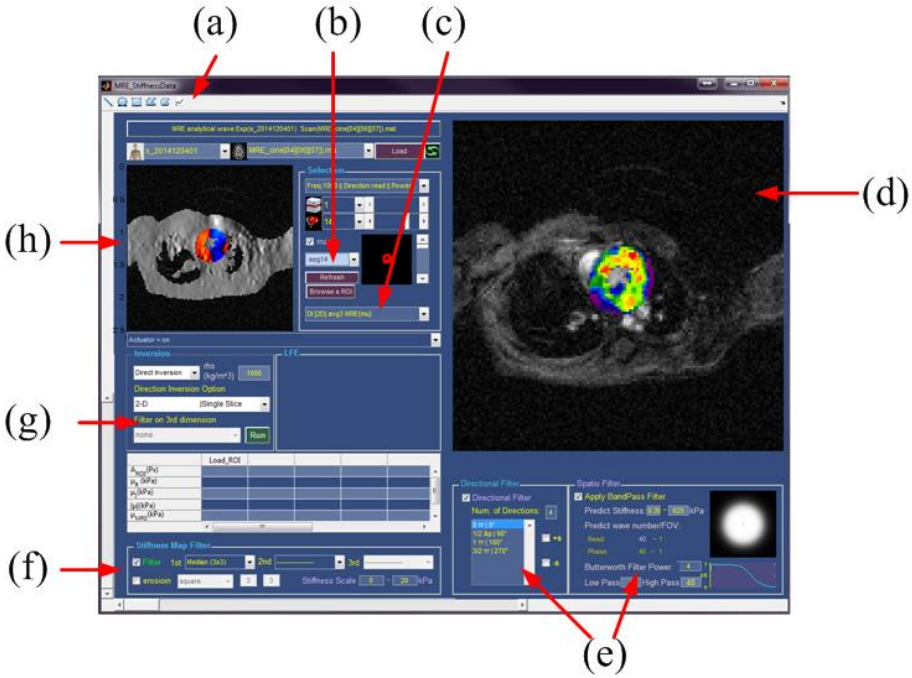

Figure 5: Stiffness map module. a) buttons to drawn ROI on the stiffness map with different shape and button to draw curves of stiffness and wave amplitude over a selected ROI over cardiac phases (for cardiac MRE only); c) popup menu to select stiffness map calculated from different inversion algorithm to display; d) display of stiffness map; e) panels to apply directional and bandpass filter, with adjustable filter parameters; f) panels for displaying parameter of the stiffness map, including image filter selection, erosion on the ROI, and stiffness range to display; g) panel to select inversion algorithm, including LFE, 2D direction inversion, 3D inversion with suppressing the compression wave, and 3D full inversion; h) display of wave image.

The stiffness map can be generated in the Stiffness map module shown in Figure 5. In this module, the directional filter and butterworth bandpass filter can be applied before converting the wave image to stiffness map, and the parameters for these filters can be interactively adjusted. Inversion algorithm available in this module including: LFE, 2D directional inversion (DI), 3D DI with suppressing compression wave, and 3D full inversion. And stiffness map from each inversion algorithm can be stored in the same data file, and can be displayed as wish be select the corresponding item in the popup menu in Figure 5d if available. Boundary condition happens in

APPENDIX C (CONTINUED)

some inversion algorithm result, so erosion with adjustable parameter is also available in this module. ROI for stiffness calculus can either imported from the pre-defined ROI in the ROI selected module, or can re-draw with the buttons on top of the module. And finally, for cardiac MRE case only, curves of stiffness and wave amplitude over the select ROI changes over the cardiac phase can be plot with the button on top of the module (the one on the right in Figure 5a).

APPENDIX D

APPROVAL OF ACC ANIMAL CARE PROTOCOLS

Approval of ACC # 12-108:

UIC UNIVERSITY OF ILLINOIS AT CHICAGO

December 3, 2014

Thomas Royston
Mechanical Engineering
M/C 251

Office of Animal Care and Institutional
Biosafety Committee (M/C 672)
Office of the Vice Chancellor for Research
206 Administrative Office Building
1737 West Polk Street
Chicago, Illinois 60612

Dear Dr. Royston:

The modifications requested in modification indicated below pertaining to your approved protocol indicated below have been reviewed and approved in accordance with the Animal Care Policies of the University of Illinois at Chicago on ***12/3/14.***

Title of Application: Mouse Lung Magnetic Resonance Elastography

ACC Number: 12-108

Modification Number: *3*

Nature of Modification: ***Personnel Addition: Vidyani Suryadevara and Yidei Liu***
Addition of MRE of heart in same living animals as MRE of lungs and MRE of lungs and heart post-mortem.

Protocol Approved: *9/25/2012*

Current Approval Period: *6/19/2014* to *6/19/2015.*

Current Funding: ***"Currently protocol NOT matched to specific funding source. Modification will need to be submitted prior to Just in time or acceptance of award to match protocol to external funding source. All animal work proposed in the funding application must be covered by an approved protocol. UIC is the only performance site currently approved for this protocol.***

This institution has Animal Welfare Assurance Number A3460.01 on file with the Office of Laboratory Animal Welfare, NIH. **This letter may only be provided as proof of IACUC approval for those specific funding sources listed above in which all portions of the grant are matched to this ACC protocol.**

Thank you for complying with the Animal Care Policies and Procedures of UIC.

Sincerely yours,

Bradley Merrill, PhD
Chair, Animal Care Committee

BM/*mbb*
cc: BRL, ACC File

APPENDIX D (CONTINUED)

Approval of ACC # 13-147:

UIC UNIVERSITY OF ILLINOIS AT CHICAGO

Office of Animal Care and Institutional
Biosafety Committee (M/C 672)
Office of the Vice Chancellor for Research
206 Administrative Office Building
1737 West Polk Street
Chicago, Illinois 60612

February 25, 2015

E. Douglas Lewandowski
Physiology & Biophysics
M/C 901

Dear Dr. Lewandowski:

The modifications requested in modification indicated below pertaining to your approved protocol indicated below have been reviewed and approved in accordance with the Animal Care Policies of the University of Illinois at Chicago on ***2/25/15.***

Title of Application: High-Magnetic Field MR Myocardial Tagging and Spectroscopy

ACC Number: 13-147

Modification Number: ***2***

Nature of Modification: ***Personnel Addition: Yifei Liu***
Addition of 13 mice to conduct left anterior descending coronary artery ligation to induce myocardial infection for testing MRI on assessing regions of scar, border zone, and remote areas and to distinguish viable from nonviable myocardium.

Condition of Initiation: ***New personnel added must complete facility orientation/zoonotic training and enter the UIC Occupational Health Program for Individuals with Animal Contact prior to initiation of any work with animals. For rodents, contact Dr. Jeanette Purcell (996-7051 for BRL, BBC, MBRB, COD, SES, COMRB barrier and all satellites), or Ms. Kelly Pavlik for BSB (996-7810). For large animal areas of the BRL and COMRB, contact Dr. Kelly Garcia (996-8619). For primates, contact Dr. Lisa Halliday (996-9453). Facility access will not be granted until this condition is completed.***

Protocol Approved: ***11/5/2013***

Current Approval Period: ***10/15/2014*** to ***10/15/2015. Protocol is eligible for 1 additional year of renewal prior to expiration and resubmission.***

Current Funding: ***Portions of this protocol are supported by the funding sources indicated in the table below.***
Number of funding sources: 2

Funding Agency	**Funding Title**			**Portion of Funding Matched**
NIH	*Magnetic Resonance of Cardiac C13 Flux and Metabolic Rate*			*Other* *Tied to 13-147 & 14-141; and Linked to Form G 14-061*
Funding Number	**Current Status**	**UIC PAF NO.**	**Performance Site**	**Funding PI**

APPENDIX D (CONTINUED)

Approval of ACC # 13-147 (continued):

R37 HL49244	*Funded*	*200704501*	*UIC*	*E. Douglas Lewandowski*
Funding Agency	**Funding Title**			**Portion of Funding Matched**
NIH	*Gender Effects on Remodeling of Lipid and Sarcomere Dynamics in Hypertrophy*			*Other* *Linked with 14-142*
Funding Number	**Current Status**	**UIC PAF NO.**	**Performance Site**	**Funding PI**
RO1 HL113057 (years 1-5 A1 version)	*Funded*	*201204710*	*UIC*	*E. Douglas Lewandowski*

This institution has Animal Welfare Assurance Number A3460.01 on file with the Office of Laboratory Animal Welfare, NIH. **This letter may only be provided as proof of IACUC approval for those specific funding sources listed above in which all portions of the grant are matched to this ACC protocol.**

Thank you for complying with the Animal Care Policies and Procedures of UIC.

Sincerely yours,

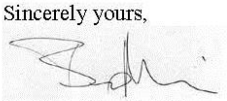

Bradley Merrill, PhD
Chair, Animal Care Committee

BM/*mbb*
cc: BRL, ACC File, Susan Kay Fischer, Jian Bi, Joseph Goldenberg, Natasha Banke

APPENDIX D (CONTINUED)

Approval of ACC # 10-188:

UIC UNIVERSITY OF ILLINOIS AT CHICAGO

Office of Animal Care and Institutional
Biosafety Committee (M/C 672)
Office of the Vice Chancellor for Research
206 Administrative Office Building
1737 West Polk Street
Chicago, Illinois 60612

July 23, 2013

E. Douglas Lewandowski
Physiology & Biophysics
M/C 901

Dear Dr. Lewandowski:

The modifications requested in modification indicated below pertaining to your approved protocol indicated below have been reviewed and approved in accordance with the Animal Care Policies of the University of Illinois at Chicago on *7/23/13.*

Title of Application: High-Magnetic Field MR Myocardial Tagging and Spectroscopy

ACC Number: 10-188

Modification Number: *6*

Nature of Modification: *Addition of Personnel: Yifei Liu*

Condition of Initiation: ***New personnel added must complete facility orientation/zoonotic training and enter the UIC Occupational Health Program for Individuals with Animal Contact prior to initiation of any work with animals. For rodents, contact Dr. Jim Artwohl (996-1217 for BRL, BBC, MBRB, COD, SES, and all satellites), Dr. Jeanette Purcell for the mouse barrier in COMRB (996-7051), or Ms. Kelly Pavlik for BSB (996-7810). For large animal areas of the BRL and COMRB, contact Dr. Kelly Garcia (996-8619). For primates, contact Dr. Lisa Halliday (996-9453). Facility access will not be granted until this condition is completed.***

Protocol Approved: *11/24/2010*

Current Approval Period: *11/16/2012* to *11/16/2013.*

Current Funding: ***Portions of this protocol are supported by the funding sources indicated in the table below.***
Number of funding sources: 3

Funding Agency	**Funding Title**			**Portion of Funding Matched**
NIH	*Magnetic Resonance of Cardiac C13 Flux and Metabolic Rate (Tied to Form G- 08-192)*			*Protocol is linked to form G G08-192*
Funding Number	**Current Status**	**UIC PAF NO.**	**Performance Site**	**Funding PI**
R37HL49244	*Funded*	*200704501*	*UIC*	*Douglas Lewandowski*

Phone (312) 996-1972 • Fax (312) 996-9088

APPENDIX D (CONTINUED)

Approval of ACC # 10-188 (continued):

Funding Agency	Funding Title			Portion of Funding Matched
NIH	*Magnetic Resonance of Cardiac C13 Flux and Metabolic Rate*			*All matched*
Funding Number	**Current Status**	**UIC PAF NO.**	**Performance Site**	**Funding PI**
R37HL49244	*Funded*	*200305814*	*UIC*	*Douglas Lewandowski*
Funding Agency	**Funding Title**			**Portion of Funding Matched**
NIH	*NMR of Mitochondrial Transporters in Cardiac Hypertrophy*			*All matched*
Funding Number	**Current Status**	**UIC PAF NO.**	**Performance Site**	**Funding PI**
RO1HL62702	*Funded*	*200502583*	*UIC*	*Douglas Lewandowski*

This institution has Animal Welfare Assurance Number A3460.01 on file with the Office of Laboratory Animal Welfare, NIH. **This letter may only be provided as proof of IACUC approval for those specific funding sources listed above in which all portions of the grant are matched to this ACC protocol.**

Thank you for complying with the Animal Care Policies and Procedures of UIC.

Sincerely yours,

Bradley Merrill, PhD
Chair, Animal Care Committee

BM/*mbb*
cc: BRL, ACC File, Janusz Hankiewicz, Susan Kay Fischer, Jian Bi, Vonaire Daly

APPENDIX D (CONTINUED)

Approval of ACC # 13-172 (continued):

UIC UNIVERSITY OF ILLINOIS AT CHICAGO

Office of Animal Care and
Institutional Biosafety Committees (MC 672)
Office of the Vice Chancellor for Research
206 Administrative Office Building
1737 West Polk Street
Chicago, Illinois 60612-7227

October 22, 2013

Dieter Klatt
Bioengineering
M/C 063

Dear Dr. Klatt:

The protocol indicated below was reviewed at a convened ACC meeting in accordance with the Animal Care Policies of the University of Illinois at Chicago on **10/15/2013**. *The protocol was not initiated until final clarifications were reviewed and approved on* **10/22/2013**. *The protocol is approved for a period of* ***3*** years with annual continuation.

Title of Application: 3D SLIM MRE of Mouse Brain

ACC Number: 13-172

Initial Approval Period: 10/22/2013 to 10/15/2014

Current Funding: ***Currently protocol NOT matched to specific funding source. Modification will need to be submitted prior to Just in time or acceptance of award to match protocol to external funding source. All animal work proposed in the funding application must be covered by an approved protocol. UIC is the only performance site currently approved for this protocol.***

This institution has Animal Welfare Assurance Number A3460.01 on file with the Office of Laboratory Animal Welfare (OLAW), NIH. **This letter may only be provided as proof of IACUC approval for those specific funding sources listed above in which all portions of the funding proposal are matched to this ACC protocol.**

In addition, all investigators are responsible for ensuring compliance with all federal and institutional policies and regulations related to use of animals under this protocol and the funding sources listed on this protocol. Please use OLAW's "*What Investigators Need to Know about the Use of Animals*" (http://grants.nih.gov/grants/olaw/InvestigatorsNeed2Know.pdf) as a reference guide. Thank you for complying with the Animal Care Policies and Procedures of UIC.

Sincerely yours,

Bradley Merrill, PhD
Chair, Animal Care Committee

BM/*mbb*
cc: BRL, ACC File, Steven Kearney

APPENDIX E

COPYRIGHT PERMISSION LETTERS AND COPYRIGHT FORMS

Copyright permission letter from ASME (corresponding to Chapter 4)

Yifei Liu

From: Beth Darchi <DarchiB@asme.org>
Sent: Thursday, March 19, 2015 1:19 PM
To: 'Yifei Liu'
Subject: RE: Inquiry of reuse my technical paper published in IMECE 2013 in my PhD dissertation

Dear Prof. Liu,
It is our pleasure to grant you permission to publish **any part or all of** the ASME paper Interpreting Microscopic Magnetic Resonance Elastography Measurements Using Finite Element Analysis," by Yifei Liu, Temel Yasar and Thomas J. Royston, Paper No. IMECE2013-63355, as cited in your letter in the thesis entitled High Resolution Magnetic Resonance Elastography -- From Phantom to Mouse Heart to be published by University of Illinois of Chicago.

Permission is granted for the specific use as stated herein and does not permit further use of the materials without proper authorization. Proper attribution must be made to the author(s) of the materials. **Please note**: if any or all of the figures and/or Tables are of another source, permission should be granted from that outside source or include the reference of the original source. ASME does not grant permission for outside source material that may be referenced in the ASME works.

As is customary, we request that you ensure proper acknowledgment of the exact sources of this material, the authors, and ASME as original publisher. Acknowledgment must be retained on all pages printed and distributed.

Unfortunately, we do not allow for web access of your full paper on ProQuest or any website. However ProQuest can list the article as a reference and/or post the **Abstracts only**. We request that ProQuest point its visitors to ASME's Digital Collection on how to obtain the article.

Many thanks for your interest in ASME publications.

Sincerely,

Beth Darchi
Publishing Administrator
ASME
2 Park Avenue, 6th Floor
New York, NY 10016-5990
Tel 1.212.591.7700
darchib@asme.org

From: Yifei Liu [mailto:yfliu.918@gmail.com]
Sent: Wednesday, March 18, 2015 12:12 PM
To: Beth Darchi

APPENDIX E (CONTINUED)

Copyright permission letter and copyright form from IOP Publishing (corresponding to Chapter 3)

Yifei Liu

From: Zora Catterick <Zora.Catterick@iop.org> on behalf of Permissions <permissions@iop.org>
Sent: Monday, March 23, 2015 6:40 AM
To: Yifei Liu
Subject: Re: Fw: inquiry of using my published article in my dissertation

Dear Yifei Liu,

Thank you for your email and for taking the time to seek this permission.

When you assigned the copyright in your article to IOP, we granted back to you certain rights, including the right to include the article within any thesis or dissertation.

Therefore, please go ahead and make what use you wish of the content of the article.

The only restriction is that if, at a later date, your thesis were to be published commercially, further permission would be required.

Please let me know if you have any further questions.

In the meantime, I wish you the best of luck with the completion of your dissertation.

Kind regards,

Zora Catterick

Publishing Assistant

IOP Publishing

Please note: We do not usually provide signed permission forms as a separate attachment. Please print this email and provide it to your publisher as proof of permission.

From: Copyright/IOPP
To: Permissions/IOPP@IOPP,
Date: 23/03/2015 08:13
Subject: Fw: inquiry of using my published article in my dissertation
Sent by: Lucy Evans

--- Forwarded by Lucy Evans/Journals/IOPP on 23/03/2015 08:13 ---

From: Yifei Liu <yfliu.918@gmail.com>
To: copyright@iop.org,
Date: 11/03/2015 17:51
Subject: inquiry of using my published article in my dissertation

---

APPENDIX E (CONTINUED)

Copyright permission letter and copyright form from IOP Publishing (corresponding to Chapter 3) (continued)

Assignment of copyright and publication agreement

IOP Publishing Limited ("IOP") agrees on behalf of the Institute of Physics and Engineering in Medicine ("IPEM") to publish:

Manuscript Title: Ultra wideband (0.5 – 16 kHz) MR elastography for robust shear viscoelasticity model identification (the "Article") written by

Names of all authors: Liu, Yifei; Yasar, Temel; Royston, Thomas ("the Named Authors") in the following journal Physics in Medicine and Biology ("the Journal")

Name of copyright owner(s) (if not the Named Author(s) – see Important Information above):
("the Institution")

IOP Ref: PMB-101267.R1

Part 1 - Subscription Copyright Assignment

Assignment of copyright
1.1 In consideration for acceptance and publication of the Article, the Named Authors of the Article and/or the Institution hereby assign, where necessary by present assignment of future copyright, to IPEM with full title guarantee the entire copyright in all original material published as part of the Article (which expression includes but is not limited to the text, abstract, tables, figures and graphs, related corrigenda or "comments" and multimedia content but excludes any other item referred to as supplementary material) throughout the world for the full term of copyright (including any extensions or renewals thereof) for all media and formats, whether known or unknown. Such assignment shall be effective only if the Article (or any resubmission of the Article) is accepted for publication. For the avoidance of doubt, copyright does not subsist in any fundamental data underlying the Article and nothing in this agreement is intended to limit access to or use of such data.

1.2 If the Article, or any part of it, is protected by Crown Copyright, in consideration for acceptance and publication of the Article, the relevant Named Authors and the relevant originating department or agency hereby grant IOP and IPEM a royalty-free worldwide freely-transferrable licence for the full term of copyright (including any extensions or renewals thereof) for all media and formats, whether known or unknown, to do in relation to the Article all acts restricted by copyright worldwide including, but not limited to, the right of action under section 101A of the Copyright Designs and Patents Act 1988. Such licence shall be effective only if the Article is accepted for publication and shall be exclusive to IOP and IPEM for a period of twelve calendar months following the date of online publication of the Article. Thereafter, the licence shall be non-exclusive.

1.3 In consideration for acceptance and publication of the Article, the Named Authors and/or the Institution hereby grant IOP and IPEM a royalty-free non-exclusive worldwide freely transferrable licence for the full term of copyright (including any extensions or renewals thereof) to do in relation to any supplementary material not deemed to be part of the Article and/or any video abstract all acts restricted by copyright worldwide. This shall include, but not be limited to, making the material available under any licence that IOP or IPEM deems appropriate for purposes including, but not limited to, the maximisation of visibility and the long term preservation of the content.

1.4 Each of the Named Authors consents to the publication and processing by IOP and IPEM of their email addresses.

Representations and warranties

APPENDIX E (CONTINUED)

Copyright permission letter and copyright form from IOP Publishing (corresponding to Chapter 3) (continued)

2.1 The Institution and/or the Submitting Author on behalf of the Named Authors (as appropriate) represent and warrant that:

2.1.1 the Article is the original work of the Named Authors;

2.1.2 the Article has not been published previously in any form, other than as part of the Named Authors' research theses or dissertations (which fact has been notified to IOP in writing) or as a preprint, for example on the arXiv.org service;

2.1.3 each of the Named Authors has made a material contribution to the conception and/or writing of the Article, has received the final version of the Article, has agreed to its submission on the terms contained herein and takes responsibility for it and submission has been approved as necessary by the authorities at the establishment where the research was carried out;

2.1.4 the Submitting Author completes and returns this agreement as authorised agent for and on behalf of all the Named Authors and has the full power to enter into this agreement and to make the grants and assignments it contains;

2.1.5 the Article has not been and shall not be submitted to another publisher prior to withdrawal or rejection by IOP;

2.1.6 the Article does not infringe any third party rights, it contains nothing libellous or unlawful, all factual statements are to the best of the Named Authors' knowledge true or based on valid research conducted according to accepted norms and all required permissions have been obtained in writing;

2.1.7 the Article expressly acknowledges any third party funding and/or potential conflicts of interest; and

2.1.8 any supplementary material or video abstract is the original work of the Named Authors, or is the property of the Institution, or permission has been obtained from its owner(s) for its publication by IOP and/or IPEM and permission has been obtained for the inclusion of any third party content (including music).
2.2 The Named Authors and/or the Institution (as appropriate) indemnify and will keep indemnified IOP and IPEM against all costs and expenses suffered or incurred by IOP or IPEM as a result of and/or arising out of any breach of the representations and/or warranties in this section 2.

The Named Authors' rights

3.1 IPEM grants the Named Authors the rights specified in paragraphs 3.2 and 3.3. All such rights must be exercised solely for non-commercial purposes. Where possible, any use should display citation information and IPEM's copyright notice, and, for electronic use, best efforts must be made to include a link to the online abstract in the Journal.

Exercise of the rights in paragraph 3.2 may use the version of the Article published in the Journal ("Final Published Version").

Exercise of the rights referred to in paragraph 3.3 must not use the Final Published Version and extend only to the Named Authors' own format (which may include amendments made following peer review but not any editing, typesetting or other changes made by IOP) (the "Accepted Manuscript") and must be accompanied by the following statement of provenance:

'This is an author-created, un-copyedited version of an article accepted for publication in Physics in Medicine and Biology.
The publisher is not responsible for any errors or omissions in this version of the manuscript or any version derived from it. The Version of Record is available online at [insert DOI].'

APPENDIX E (CONTINUED)

Copyright permission letter and copyright form from IOP Publishing (corresponding to Chapter 3) (continued)

3.2 The rights are:

3.2.1 To make copies of the Article (all or part) for teaching purposes;

3.2.2 To include the Article (all or part) in a research thesis or dissertation;

3.2.3 To make oral presentation of the Article (all or part) and to include a summary and/or highlights of it in papers distributed at such presentations or in conference proceedings; and

3.2.4 To use figures and text from the Article falling within the quota outlined in the STM Permissions Guidelines (http://www.stm-assoc.org/permissions-guidelines/) at the relevant time in force.
For the avoidance of doubt, the Named Authors retain all proprietary rights in the Article other than copyright.

3.3 Additional rights of the Named Authors are to:

3.3.1 Use the Accepted Manuscript (all or part) without modification in personal compilations of the Named Authors' own works (provided not created by a third party publisher); and

3.3.2 Include the Accepted Manuscript (all or part) on the Named Authors' own personal website(s), institutional website(s) and third party websites in accordance with the Author Rights set out at the following url legal.ioppublishing.org/author-rights on the date of submission of this agreement.
Miscellaneous

4. To the extent that there are moral rights in the Article, all the Named Authors expressly reserve and assert their moral rights to be identified as the authors of the Article.

5. The Named Authors and/or the Institution shall execute such further documents, and take such actions and do such things, as may be requested by IOP at IPEM's reasonable expense to give full effect to the terms of this agreement.

6. For the avoidance of doubt, the grants and assignment envisaged herein shall become effective only upon acceptance of the Article for publication. In the event that the Article is withdrawn prior to acceptance, or is rejected, this agreement shall have no effect and no party shall be bound by it.

7. This agreement shall be governed by English Law and subject to the non-exclusive jurisdiction of the English courts.

Confirmation

8. By typing the Submitting Author's name into the box at Part 3 below and clicking "Submit", the Named Authors agree to these terms. Authorised signatories of any third party copyright owner(s) agree, on behalf of such owner(s), to these terms by typing the owner's name into the "Institution" box at the top of the page.

Part 2 - Open Access Copyright Assignment
Assignment of copyright

1.1 In consideration for acceptance and publication of the Article, the Named Authors of the Article and/or the Institution hereby assign, where necessary by present assignment of future copyright, to IPEM with full title guarantee the entire copyright in all original material published as part of the Article (which expression includes but is not limited to the text, abstract, tables, figures and graphs, related corrigenda or "comments" and multimedia content but excludes any other item referred to as

APPENDIX E (CONTINUED)

Copyright permission letter and copyright form from IOP Publishing (corresponding to Chapter 3) (continued)

supplementary material) throughout the world for the full term of copyright (including any extensions or renewals thereof) for all media and formats, whether known or unknown. Such assignment shall be effective only if the Article (or any resubmission of the Article) is accepted for publication. For the avoidance of doubt, copyright does not subsist in any fundamental data underlying the Article and nothing in this agreement is intended to limit access to or use of such data.

1.2 If the Article, or any part of it, is protected by Crown Copyright, in consideration for acceptance and publication of the Article, the relevant Named Authors and/or the relevant originating department or agency hereby grant IOP and IPEM a royalty-free worldwide licence for the full term of copyright (including any extensions or renewals thereof) for all media and formats, whether known or unknown, to do in relation to the Article all acts restricted by copyright worldwide.

1.3 In consideration for acceptance and publication of the Article, the Named Authors and/or the Institution hereby grant IOP and IPEM a royalty-free non-exclusive worldwide freely transferrable licence for the full term of copyright (including any extensions or renewals thereof) to do in relation to any supplementary material not deemed to be part of the Article and/or any video abstract all acts restricted by copyright worldwide. This shall include, but not be limited to, making the material available under any licence that IOP or IPEM deems appropriate for purposes including, but not limited to, the maximisation of visibility and the long term preservation of the content.

1.4 Each of the Named Authors consents to the publication and processing by IOP and IPEM of their email addresses.

1.5 Each of the Named Authors and, where relevant, the Institution consents to the publication of the Article under the Creative Commons Attribution 3.0 Unported licence (https://creativecommons.org/licenses/by/3.0/) or any successor to that licence.

Representations and warranties

2.1 The Institution and/or the Submitting Author, on behalf of the Named Authors (as appropriate) represent and warrant that:

2.1.1 the Article is the original work of the Named Authors;

2.1.2 the Article has not been published previously in any form, other than as part of the Named Authors' research theses or dissertations (which fact has been notified to IOP in writing) or as a pre-print, for example on the arXiv.org service;

2.1.3 each of the Named Authors has made a material contribution to the conception and/or writing of the Article, has received the final version of the Article, has agreed to its submission on the terms contained herein and takes responsibility for it and submission has been approved as necessary by the authorities at the establishment where the research was carried out;

2.1.4 the Submitting Author completes and returns this agreement as authorised agent for and on behalf of all the Named Authors and has the full power to enter into this agreement and to make the grants and assignments it contains;

2.1.5 the Article has not been and shall not be submitted to another publisher prior to withdrawal or rejection by IOP;

2.1.6 the Article does not infringe any third party rights, it contains nothing libellous or unlawful, all factual statements are to the best of the Named Authors' knowledge true or based on valid research conducted according to accepted norms and all required permissions have been obtained in writing;

2.1.7 the Article explicitly acknowledges any third party funding and/or potential conflicts of interest; and

2.1.8 any supplementary material or video abstract is the original work of the Named Authors, or is the

APPENDIX E (CONTINUED)

Copyright permission letter and copyright form from IOP Publishing (corresponding to Chapter 3) (continued)

property of the Institution, or permission has been obtained from its owner(s) for its publication by IOP and/or IPEM and permission has been obtained for the inclusion of any third party content (including music).
2.2 The Named Authors and/or the Institution indemnify and will keep indemnified IOP and IPEM against all costs and expenses suffered or incurred by IOP or IPEM as a result of and/or arising out of any breach of the representations and/or warranties in this section 2.

The Named Authors' rights

3.1 The Named Authors and all third parties will have the rights to use the Article as described in the licence applied to the Article pursuant to paragraph 1.5, above, which shall include the right to copy, distribute and display the published version of the Article and create derivative works, subject to appropriate attribution.

3.2 Where the Article is used in accordance with paragraph 3.1 above, the following attribution shall be included:
Article title
Named Author(s)
DOI
Journal citation

Miscellaneous

4. To the extent that there are moral rights in the Article, all the Named Authors expressly reserve and assert their moral rights to be identified as the authors of the Article.

5. The Named Authors and/or the Institution shall execute such further documents, and take such actions and do such things, as may be requested by IOP at IPEM's reasonable expense to give full effect to the terms of this agreement.

6. For the avoidance of doubt, the grants and assignment envisaged herein shall become effective only upon acceptance of the Article for publication. In the event that the Article is withdrawn prior to acceptance, or is rejected, this agreement shall have no effect and no party shall be bound by it.

7. This agreement shall be governed by English Law and subject to the non-exclusive jurisdiction of the English courts.

Confirmation

8. By typing the Submitting Author's name into the box at Part 3 below and clicking "Submit", the Named Authors agree to all these terms. Authorised signatories of any third party copyright owner(s) agree, on behalf of such owner(s), to these terms by typing the owner's name into the "Institution" box at the top of the page.

Part 3 – Confirmation and Execution

Please tick the box below to confirm the basis upon which you are submitting the Article.
Subscription Copyright Assignment – Part 1 Applies

APPENDIX E (CONTINUED)

Copyright permission letter and copyright form from IOP Publishing (corresponding to Chapter 3) (continued)

Type your name here:

Yifei Liu (the "Submitting Author")

Date:

24-Sep-2014

By clicking "Submit" and typing your name above, you shall be assumed to have read and understood all of the terms and conditions of the relevant part of this agreement and you will be agreeing to all of the terms and conditions and assignment (as the case may be) detailed above.

LAST UPDATED June 2014

CITED LITERATURE

1. Othman, S.F., et al., *Microscopic magnetic resonance elastography (μMRE).* Magnetic Resonance in Medicine, 2005. **54**(3): p. 605-615.
2. Sewell, C.W., *Pathology of benign and malignant breast disorders.* Radiologic Clinics of North America, 1995. **33**(6): p. 1067-80.
3. von Gierke, H.E., et al., *Physics of Vibrations in Living Tissues*. Vol. 4. 1952. 886-900.
4. Ophir, J., et al., *Elastography: A quantitative method for imaging the elasticity of biological tissues.* Ultrasonic Imaging, 1991. **13**(2): p. 111-134.
5. Zerhouni, E.A., et al., *Human heart: tagging with MR imaging--a method for noninvasive assessment of myocardial motion.* Radiology, 1988. **169**(1): p. 59-63.
6. Axel, L. and L. Dougherty, *MR imaging of motion with spatial modulation of magnetization.* Radiology, 1989. **171**(3): p. 841-845.
7. Plewes, D.B., et al., *Visualizing tissue compliance with MR imaging.* Journal of Magnetic Resonance Imaging, 1995. **5**(6): p. 733-738.
8. Muthupillai, R., et al., *Magnetic resonance elastography by direct visualization of propagating acoustic strain waves.* Science, 1995. **269**(5232): p. 1854-1857.
9. Manduca, A., et al., *Magnetic resonance elastography: non-invasive mapping of tissue elasticity.* Medical Image Analysis, 2001. **5**(4): p. 237-54.
10. Manduca, A., et al., *Image processing for magnetic-resonance elastography*, in *SPIE Proceedings*. 1996. p. 616-623.
11. Papazoglou, S., et al., *Algebraic Helmholtz inversion in planar magnetic resonance elastography.* Physics in Medicine and Biology, 2008. **53**(12): p. 3147.
12. Yin, M., et al., *Assessment of Hepatic Fibrosis With Magnetic Resonance Elastography.* Clinical Gastroenterology and Hepatology, 2007. **5**(10): p. 1207-1213.e2.
13. Klatt, D., et al., *Viscoelastic properties of liver measured by oscillatory rheometry and multifrequency magnetic resonance elastography.* Biorheology, 2010. **47**(2): p. 133-141.
14. McKnight, A.L., et al., *MR Elastography of Breast Cancer: Preliminary Results.* American Journal of Roentgenology, 2002. **178**(6): p. 1411-1417.
15. Sack, I., J. Bernarding, and J. Braun, *Analysis of wave patterns in MR elastography of skeletal muscle using coupled harmonic oscillator simulations.* Magnetic Resonance Imaging, 2002. **20**(1): p. 95-104.
16. Klatt, D., et al., *Viscoelasticity-based MR elastography of skeletal muscle.* Physics in Medicine and Biology, 2010. **55**(21): p. 6445.
17. Xu, L., et al., *Magnetic resonance elastography of the human brain: a preliminary study.* Acta Radiologica, 2007. **48**(1): p. 112-115.

CITED LITERATURE (CONTINUED)

18. Klatt, D., et al., *Noninvasive assessment of the rheological behavior of human organs using multifrequency MR elastography: a study of brain and liver viscoelasticity.* Physics in Medicine and Biology, 2007. **52**(24): p. 7281.

19. Hamhaber, U., et al., *In vivo magnetic resonance elastography of human brain at 7 T and 1.5 T.* Journal of Magnetic Resonance Imaging, 2010. **32**(3): p. 577-583.

20. Goss, B.C., et al., *Magnetic resonance elastography of the lung: Technical feasibility.* Magnetic Resonance in Medicine, 2006. **56**(5): p. 1060-1066.

21. Mariappan, Y.K., et al., *Magnetic resonance elastography of the lung parenchyma in an in situ porcine model with a noninvasive mechanical driver: Correlation of shear stiffness with trans-respiratory system pressures.* Magnetic Resonance in Medicine, 2012. **67**(1): p. 210-217.

22. Litwiller, D.V., et al., *MR Elastography of the Eye: Initial Feasibility* in *Proceedings of the 15th Annual Meeting of ISMRM*. 2007.

23. Litwiller, D.V., et al., *MR elastography of the ex vivo bovine globe.* Journal of Magnetic Resonance Imaging, 2010. **32**(1): p. 44-51.

24. Kolipaka, A., et al., *MR Elastography as a Method for the Assessment of Myocardial Stiffness: Comparison with an Established Pressure–Volume Model in a Left Ventricular Model of the Heart.* Magnetic Resonance in Medicine, 2009(62): p. 135–140.

25. Elgeti, T., et al., *Cardiac Magnetic Resonance Elastography: Initial Results.* Investigative Radiology, 2008. **43**(11): p. 762-772.

26. Gaasch, W.H., et al., *Left ventricular compliance: Mechanisms and clinical implications.* The American Journal of Cardiology, 1976. **38**(5): p. 645-653.

27. Jr., N.B.I., et al., Systolic and Diastolic Function of the Heart. Studies in Health Technology and Informatics. Vol. 21. 1996: IOS press.

28. Diamond, G., et al., Dlastolic Pressure-Volume Relationship in the Canine Left Ventricle. Circulation Research, 1971. 29(3): p. 267-275.

29. Mirsky, i. and w.w. Parmley, *Assessment of Passive Elastic Stiffness for Isolated Heart Muscle and the Intact Heart.* Circulation Research, 1973. **33**(2): p. 233-243.

30. Segura, A., O.H. Frazier, and L.M. Buja, *Fibrosis and heart failure.* Heart Failure Reviews, 2014. **19**(2): p. 173-185.

31. Benech, J.C., et al., *Diabetes increases stiffness of live cardiomyocytes measured by atomic force microscopy nanoindentation*. Vol. 307. 2014. C910-C919.

32. Borbély, A., et al., *Cardiomyocyte Stiffness in Diastolic Heart Failure.* Circulation, 2005. **111**(6): p. 774-781.

33. Harvey, P.A. and L.A. Leinwand, *Cellular mechanisms of cardiomyopathy.* The Journal of Cell Biology, 2011. **194**(3): p. 355-365.

CITED LITERATURE (CONTINUED)

34. Burkhoff, D., I. Mirsky, and H. Suga, *Assessment of systolic and diastolic ventricular properties via pressure-volume analysis: a guide for clinical, translational, and basic researchers*. Vol. 289. 2005. H501-H512.

35. Axel, L., *Tagged MRI-Based Studies of Cardiac Function*, in *Functional Imaging and Modeling of the Heart*, I. Magnin, et al., Editors. 2003, Springer Berlin Heidelberg. p. 1-7.

36. Shehata, M., et al., *Myocardial tissue tagging with cardiovascular magnetic resonance.* Journal of Cardiovascular Magnetic Resonance, 2009. **11**(1): p. 55.

37. Acton, Q.A., *Catheterization: New Insights for the Healthcare Professional: 2013 Edition: ScholarlyBrief*. 2013: ScholarlyEditions.

38. Schuijf, J.D., et al., *Cardiac imaging in coronary artery disease: differing modalities.* Heart, 2005. **91**(8): p. 1110-1117.

39. Bom, N., *Echocardiology: with Doppler applications and Real time imaging*. 2012: Springer Netherlands.

40. Musani, M.H., E.J. Feldmann, and M. Poon, *Clinical Pearls in Diagnostic Cardiac Computed Tomographic Angiography*. 2015: Springer International Publishing.

41. Pelberg, R., *Cardiac CT Angiography Manual*. 2015: Springer London.

42. Di Carli, M.F. and M.J. Lipton, *Cardiac PET and PET/CT Imaging*. 2007: Springer New York.

43. Heller, G.V. and R.C. Hendel, *Handbook of Nuclear Cardiology: Cardiac SPECT and Cardiac PET*. 2012: Springer London.

44. Bogaert, J., et al., *Clinical Cardiac MRI*. 2012: Springer Berlin Heidelberg.

45. Kolipaka, A., et al., *Evaluation of a Rapid, Multiphase MRE Sequence in a Heart-Simulating Phantom.* Magnetic Resonance in Medicine, 2009(62): p. 691-698.

46. Kolipaka, A., et al., *MR elastography as a method for the assessment of myocardial stiffness: Comparison with an established pressure–volume model in a left ventricular model of the heart.* Magnetic Resonance in Medicine, 2009. **62**(1): p. 135-140.

47. Kolipaka, A., et al., *Magnetic resonance elastography: Inversions in bounded media.* Magnetic Resonance in Medicine, 2009. **62**(6): p. 1533-1542.

48. Kolipaka, A., et al., *Magnetic Resonance Elastography as a Method for the Assessment of Effective Myocardial Stiffness Throughout the Cardiac Cycle.* Magnetic Resonance in Medicine, 2010(64): p. 862-870.

49. Kolipaka, A., et al., *In vivo assessment of MR elastography-derived effective end-diastolic myocardial stiffness under different loading conditions.* Journal of Magnetic Resonance Imaging, 2011. **33**(5): p. 1224-1228.

CITED LITERATURE (CONTINUED)

50. Kolipaka, A., et al., *Magnetic Resonance Elastography as a Method to Estimate Myocardial Contractility.* Journal of Magnetic Resonance Imaging, 2012. **36**: p. 120-127.

51. Kolipaka1, A., et al. *In Vivo Cardiac MR Elastography in a Single Breath Hold*. in *Proceedings of the 18th Annual Meeting of ISMRM*. 2010. Stockholm, Sweden.

52. Sack, I., et al., *MR Elastography of the Human Heart: Noninvasive Assessment of Myocardial Elasticity Changes by Shear Wave Amplitude Variations.* Magnetic Resonance in Medicine, 2009. **61**: p. 668-677.

53. Elgeti, T., et al., *Cardiac Magnetic Resonance Elastography: Toward the Diagnosis of Abnormal Myocardial Relaxation.* Investigative Radiology, 2010. **45**(12): p. 782-787 10.1097/RLI.0b013e3181ec4b63.

54. Liu, Y., T.K. Yasar, and T.J. Royston, *Ultra wideband (0.5–16 kHz) MR elastography for robust shear viscoelasticity model identification.* Physics in Medicine and Biology, 2014. **59**(24): p. 7717.

55. Yasar, T.K., T.J. Royston, and R.L. Magin, *Wideband MR elastography for viscoelasticity model identification.* Magnetic Resonance in Medicine, 2013. **70**(2): p. 479-489.

56. Liang, Z.P. and P.C. Lauterbur, *Principles of Magnetic Resonance Imaging: A Signal Processing Perspective*. 1999: Wiley.

57. Brown, M.A. and R.C. Semelka, *MRI: Basic Principles and Applications*. 2011: Wiley.

58. Webb, A.G., *Introduction to Biomedical Imaging*. 2002: Wiley.

59. Blumich, B., *NMR Imaging of Materials*. 2000: OUP Oxford.

60. Yasar, T.K., et al. *Optimal Motion Encoding Scheme for MR Elastography*. in *23rd ISMRM*. 2015. Toronto, Canada.

61. TK, Y., et al., *Selective spectral displacement projection for multifrequency MRE.* Physics in Medicine and Biology, 2013. **58**(16): p. 5771.

62. Moran, P.R., *A flow velocity zeugmatographic interlace for NMR imaging in humans.* Magn Reson Imaging, 1982. **1**: p. 197-203.

63. Mariappan, Y.K., K.J. Glaser, and R.L. Ehman, *Magnetic resonance elastography: A review.* Clinical Anatomy, 2010. **23**(5): p. 497-511.

64. Rump, J., et al., *Fractional encoding of harmonic motions in MR elastography.* Magnetic Resonance in Medicine, 2007. **57**(2): p. 388-395.

65. Klatt, D., et al., *Sample interval modulation for the simultaneous acquisition of displacement vector data in magnetic resonance elastography: theory and application.* Physics in medicine and biology, 2013. **58**(24).

66. Yasar, T.K., et al. *Unified Sampling Time Interval Modulation MR Elastography*. in *Proceedings of the 23rd Annual Meeting of ISMRM*. 2015. Toronto, CA.

CITED LITERATURE (CONTINUED)

67. Knutsson, H., C.-f. Westin, and G. Granlund. *Local multiscale frequency and bandwidth estimation*. in *Image Processing, 1994. Proceedings. ICIP-94., IEEE International Conference*. 1994.

68. Fung, Y.C., *Biomechanics: Mechanical Properties of Living Tissues*. 1993: Springer New York.

69. Van Houten, E.E.W., et al., *An overlapping subzone technique for MR-based elastic property reconstruction.* Magnetic Resonance in Medicine, 1999. **42**(4): p. 779-786.

70. Yin, Z., et al., *Mechanical characterization of tissue-engineered cartilage using microscopic magnetic resonance elastography.* Tissue Engineering Part C: Methods, 2013.

71. Sack, I., et al., *The impact of aging and gender on brain viscoelasticity*. Neuroimage, 2009. **46**(3): p. 652-7. Epub 2009 Mar 10.

72. Klatt, D., et al. *Wide Dynamic Range MR Elastography of Liver*. in *Proceedings of the 18th Annual Meeting of ISMRM*. 2010.

73. Sack, I., et al., *Observation of nonlinear shear wave propagation using magnetic resonance elastography.* Magnetic Resonance in Medicine, 2004. **52**(4): p. 842-850.

74. Yasar, T.K., T.J. Royston, and R.L. Magin. *Taking MR elastography (MRE) to the microscopic scale (uMRE)*. in *Biomedical Imaging: From Nano to Macro, 2011 IEEE International Symposium on*. 2011.

75. Royston, T.J., T.K. Yasar, and R.L. Magin. *Geometric focusing of high frequency shear waves for noninvasive high resolution MR elastography*. in *Proceedings of the 19th Annual Meeting of ISMRM*. 2011. Montreal, Canada.

76. Sneddon, I.N., *The relation between load and penetration in the axisymmetric boussinesq problem for a punch of arbitrary profile.* International Journal of Engineering Science, 1965. **3**(1): p. 47-57.

77. Gutierrez-Lemini, D., *Engineering Viscoelasticity*. 2014, New York: Springer.

78. Schiessel, H., et al., *Nonnenmacher, Generalized viscoelastic models: Their fractional equations with solutions.* J. Phys. A Mathemat, 1995. **Gen. 28**.

79. Magin, R.L., *Fractional calculus in bioengineering.* Critical reviews in biomedical engineering, 2004. **32**: p. 1-104.

80. Bagley, R.L. and J. Torvik, *Fractional calculus - A different approach to the analysis of viscoelastically damped structures.* AIAA Journal, 1983. **21**(5): p. 741-748.

81. Akaike, H., *A new look at the statistical model identification.* Automatic Control, IEEE Transactions, 1974. **19** (6): p. 716 - 723

82. Bochud, N. and G. Rus, *Probabilistic inverse problem to characterize of tissue-equivalent material mechanical properties.* IEEE Transactions on Ultrasonics Ferroelectrics and Frequency Control, 2012. **59**(7): p. 1443-1456.

CITED LITERATURE (CONTINUED)

83. Royston, T.J., et al., *Estimating material viscoelastic properties based on surface wave measurements: A comparison of techniques and modeling assumptions.* Journal of the Acoustical Society of America, 2011. **130**(6): p. 4126–4138.

84. Riek, K., et al., *Magnetic resonance elastography reveals altered brain viscoelasticity in experimental autoimmune encephalomyelitis.* NeuroImage: Clinical, 2012. **1**(1): p. 81-90.

85. Freimann, F.B., et al., *Alteration of brain viscoelasticity after shunt treatment in normal pressure hydrocephalus.* Neuroradiology, 2011. **54**(3): p. 189-196.

86. Manduca, A., et al., *Spatio-temporal directional filtering for improved inversion of MR elastography images.* Medical Image Analysis, 2003. **7**(4): p. 465-473.

87. Murphy, M.C., et al., *Measuring the Characteristic Topography of Brain Stiffness with Magnetic Resonance Elastography.* PLoS ONE, 2013. **8**(12): p. e81668.

88. Sewell-Loftin, M.K., et al., *Novel technique for quantifying mouse heart valve leaflet stiffness with atomic force microscopy.* The Journal of heart valve disease, 2012. **21**(4): p. 513-520.

89. Nordbø, Ø., et al., *A computational pipeline for quantification of mouse myocardial stiffness parameters.* Computers in Biology and Medicine, 2014. **53**(0): p. 65-75.

90. Yin, M., et al., *Quantitative assessment of hepatic fibrosis in an animal model with magnetic resonance elastography.* Magnetic Resonance in Medicine, 2007. **58**(2): p. 346-353.

91. Royston, T.J., et al., *Modeling sound transmission through the pulmonary system and chest with application to diagnosis of a collapsed lung.* The Journal of the Acoustical Society of America, 2002. **111**(4): p. 1931-1946.

92. Dai, Z., et al., *Comparison of Poroviscoelastic Models for Sound and Vibration in the Lungs.* Journal of Vibration and Acoustics, 2014. **136**: p. 051012-1-051012-11.

93. Abe, H., K. Hayashi, and M. Sato, *Data Book on Mechanical Properties of Living Cells, Tissues, and Organs*. 2013: Springer Japan.

94. Zile, M.R., C.F. Baicu, and W.H. Gaasch, *Diastolic Heart Failure -- Abnormalities in Active Relaxation and Passive Stiffness of the Left Ventricle.* New England Journal of Medicine, 2004. **350**(19): p. 1953-1959.

95. Sinning, D., et al., *Increased Left Ventricular Stiffness Impairs Exercise Capacity in Patients with Heart Failure Symptoms Despite Normal Left Ventricular Ejection Fraction.* Cardiology Research and Practice, 2011.

96. Benech, J.C., et al., *Diabetes increases stiffness of live cardiomyocytes measured by atomic force microscopy nanoindentation.* American Journal of Physiology: Cell Physiology, 2014. **307**(10): p. C910-C919.

CITED LITERATURE (CONTINUED)

97. Conrad, C.H., et al., *Myocardial Fibrosis and Stiffness With Hypertrophy and Heart Failure in the Spontaneously Hypertensive Rat.* Circulation, 1995. **91**: p. 161-170.

98. Hankiewicz, J.H., et al., *Early impairment of transmural principal strains in the left ventricular wall after short-term, high-fat feeding of mice predisposed to cardiac steatosis.* Circulation: Cardiovascular Imaging, 2010. **3**: p. 710-717

99. Burkhoff, D., I. Mirsky, and H. Suga, *Assessment of systolic and diastolic ventricular properties via pressure-volume analysis: a guide for clinical, translational, and basic researchers.* American Journal of Physiology: Heart and Circulatory Physiology, 2005. **289**(2): p. H501-H512.

100. Mirsky, I. and A. Pasipoularides, *Clinical assessment of diastolic function.* Progress in Cardiovascular Diseases, 1990. **32**(4): p. 291-318.

101. Bluemke, D.A., et al., *Segmented K-Space Cine Breath-Hold Cardiovascular MR Imaging: Part 1. Principles and Technique.* AJR American journal of Roentgenology, 1997. **169**(2): p. 395-400.

102. Achenbach, S., et al., *CV Imaging: What Was New in 2012?* JACC: Cardiovascular Imaging, 2013. **6**(6): p. 714-734.

103. Dandel, M., et al., *Strain and Strain Rate Imaging by Echocardiography - Basic Concepts and Clinical Applicability.* Current Cardiology Reviews, 2009. **5**(2): p. 133-148.

104. Elgeti, T. and I. Sack, *Magnetic Resonance Elastography of the Heart.* Current Cardiovascular Imaging Reports, 2014. **7**(2): p. 1-9.

105. Elgeti, T., et al., *Shear-wave Amplitudes Measured with Cardiac MR Elastography for Diagnosis of Diastolic Dysfunction.* Radiology, 2014. **271**(3): p. 681-687.

106. Kolipaka, A., et al., *A Feasibility Study: MR Elastography as a Method to Compare Stiffness Estimates in Hypertrophic Obstructive Cardiomyopathy and in Normal Volunteers*, in *19th ISMRM*. 2011: Montreal. p. 274.

107. Zaragoza, C., et al., *Animal Models of Cardiovascular Diseases.* Journal of Biomedicine and Biotechnology, 2011. **2011**.

108. Russell, J.C. and S.D. Proctor, *Small animal models of cardiovascular disease: tools for the study of the roles of metabolic syndrome, dyslipidemia, and atherosclerosis.* Cardiovascular Pathology, 2006. **15**(6): p. 318-330.

109. Clayton, E.H., J.R. Garbow, and P.V. Bayly, *Frequency-Dependent Viscoelastic Parameters of Mouse Brain Tissue Estimated by MR Elastography.* Physics in medicine and biology, 2011. **56**(8): p. 2391-2406.

110. Elgeti, T., et al., *Cardiac MR Elastography: Comparison with left ventricular pressure measurement.* Journal of Cardiovascular Magnetic Resonance, 2009. **11**(1): p. 44.

CITED LITERATURE (CONTINUED)

111. Achenbach, J.D., *Wave Propagation in Elastic Solids*. 1973: North-Holland Publishing Company.

112. Pantely, G.A. and J. David Bristow, *Ischemic cardiomyopathy.* Progress in Cardiovascular Diseases, 1984. **27**(2): p. 95-114.

113. Pacher, P., et al., *Measurement of cardiac function using pressure–volume conductance catheter technique in mice and rats.* Nature protocols, 2008. **3**(9): p. 1422-1434.

114. Kusumoto, F.M., *ECG Interpretation: From Pathophysiology to Clinical Application*. 2009: Springer US.

115. Bohl, S., et al., *Refined approach for quantification of in vivo ischemia-reperfusion injury in the mouse heart.* American Journal of Physiology - Heart and Circulatory Physiology, 2009. **297**(6): p. H2054-H2058.

116. Banke, N.H., et al., *Preferential Oxidation of Triacylglyceride-Derived Fatty Acids in Heart Is Augmented by the Nuclear Receptor PPARα.* Circulation Research, 2010. **107**(2): p. 233-241.

117. Raya, T.E., et al., *Serial changes in left ventricular relaxation and chamber stiffness after large myocardial infarction in rats.* Circulation, 1988. **77**(6): p. 1424-31.

118. Forrester, J.S., et al., *Early Increase in Left Ventricular Compliance after Myocardial Infarction.* Journal of Clinical Investigation, 1972. **51**(3): p. 598-603.

119. Hood, W.B., Jr., et al., *Experimental myocardial infarction: IV. Reduction of left ventricular compliance in the healing phase.* The Journal of Clinical Investigation, 1970. **49**(7): p. 1316-1323.

120. Atay, S.M., et al., *Measurement of the Dynamic Shear Modulus of Mouse Brain Tissue In Vivo By Magnetic Resonance Elastography.* Journal of biomechanical engineering, 2008. **130**(2): p. 021013-021013.

VITA

EDUCATION

Doctor of Philosophy (Mechanical Engineer), *August 2015*

University of Illinois at Chicago, Chicago, IL

Dissertation: High Resolution Cardiac Magnetic Resonance Elastography, from phantom to mouse heart

Advisor: Thomas J. Royston

Master of Science (Mechanical Engineering), *August 2010*

University of Illinois at Chicago, Chicago, IL

Thesis: In silico Investigation of the Fluid Structure Interaction in Spinal Cord and Subarachnoid Space

Advisor: Thomas J. Royston

Bachelor of Science (Mechanical Engineering), *July 2002*

Donghua University, Shanghai, China

Thesis: On-line Detection of Electrical Discharge Machining (EDM) Spark Locations Research

Advisor: Qiang Han

RESEARCH EXPERIENCE

Research Assistant: *2009-2015*

Acoustics and Vibrations Lab (AVL), University of Illinois at Chicago, Chicago, IL

PROFESSIONAL MEMBERSHIP:

American Society of Mechanical Engineers (ASME)

Biomedical Engineering Society (BMES)

IEEE

VITA (CONTINUED)

ISMRM

HONORS:

ISMRM Educational Stipend Award,

Graduate College Travel Awards, UIC, 2010,2011,2012,2015.

PUBLICATION:

Journal Articles:

Yifei Liu, Thomas J. Royston, Dieter Klatt, E. Douglas Lewandowski, "*Cardiac MRE on mouse heart: initial results*", Magn. Reson. Med, under review

Yifei Liu, Temel K. Yasar, Thomas J. Royston, "*Ultra wideband (0.5 – 16 kHz) MR elastography for robust shear viscoelasticity model identification*", Physics in Medicine and Biology, 2014. 59(24): p. 7717.

Benjamin L. Schwartz, Ziying Yin, Temel K. Yasar, **Yifei Liu**, Altaf A. Khan, Allen Q. Ye, and Richard L. Magin, "*Scattering and Diffraction of Elastodynamic Waves in a Concentric Cylindrical Phantom for MR Elastography*". IEEE Trans. Biomed. Eng, 2015, under review

Benjamin Schwartz, **Yifei Liu**, Thomas Royston, and Richard Magin, "*Diffraction of a cylindrical transverse wave by an elastic spherical inclusion: an axisymmetric problem*", J. Sound Vib. submitted.

Ziying Yin, Thomas L. Schmid, Temel K. Yasar, **Yifei Liu**, Thomas J. Royston and Richard L. Magin, "*Mechanical Characterization of Tissue-Engineered Cartilage Using Microscopic Magnetic Resonance Elastography (μMRE)*", Tissue Engineering Part C: Methods. August 2014, 20(8): 611-619. doi:10.1089/ten.tec.2013.0408.

Thomas J. Royston, Zoujun Dai, Rajesh Chaunsali, **Yifei Liu**, Ying Peng, Richard L. Magin, "*Estimating material viscoelastic properties based on surface wave measurements: A*

VITA (CONTINUED)

comparison of techniques and modeling assumptions", Journal of the Acoustical Society of America 130 (6), 4126 – 4138 (2011).

Conference Paper:

Yifei Liu, Temel K. Yasar, Thomas J. Royston, "*Interpreting Microscopic Magnetic Resonance Elastography Measurements using Finite Element Analysis*", Proceedings of the ASME 2013 International Mechanical Engineering

Conference presentations:

Yifei Liu, Thomas J Royston, and E Douglas Lewandowski "*In vivo Cardiac MR Elastography on mouse*", Proceedings of the 23rd Annual Meeting of ISMRM (Toronto, CA, May 30-June 5, 2015), ***accepted as E-poster***

Yifei Liu, Julia Zelenakova, Kejia Cai, Robert Kleps, Thomas J Royston, Richard L Magin, Andrew Larson, and Weiguo Li, "*Assessment of the stiffness of intervertebral disk in rat model with Magnetic Resonance Elastography*", Proceedings of the 23rd Annual Meeting of ISMRM (Toronto, CA, May 30-June 5, 2015). ***accepted as traditional poster***

Temel K. Yasar, **Yifei Liu**, Dieter Klatt, Richard L. Magin, Thomas J. Royston, "*Unified Sampling Time Interval Modulation MR Elastography*", Proceedings of the 23rd Annual Meeting of ISMRM (Toronto, CA, May 30-June 5, 2015). ***accepted as oral presentation***

Yifei Liu, Temel K. Yaşar, Thomas J. Royston , "*Wideband MR Elastography up to 15 kHz for robust shear viscoelasticity model identification*", Symposium of Frontiers in Elastography (Urbana, Illinois, USA, June 2-3, 2014). ***accepted as traditional poster***

Ziying Yin, **Yifei Liu**, Temel K. Yasar, Thomas J. Royston, Richard L. Magin, " *Evaluation of Tissue Engineered Cartilage Using Microscopic Magnetic Resonance Elastography (μMRE)*", 54th ECN Conference (Pacific Grove, CA, April 14-19, 2013). ***accepted as oral presentation***

VITA (CONTINUED)

Yifei Liu, Temel K. Yasar, Thomas J. Royston, Richard L. Magin, "*A finite element simulation for wave propagation in magnetic resonance elastography*", BMES 2012 Annual Meeting (Atlanta, GA, October 24 – 27, 2012). ***accepted as traditional poster***

Yifei Liu, Bryn A. Martin, Thomas J. Royston, Frank Loth, "*A fluid structure interaction simulation of the cerebrospinal fluid, spinal cord, and spinal stenosis present in syringomylia*," Proceedings of the ASME 2010 Summer Bioengineering Conference (Naples, FL, June 16 – 19, 2010). ***accepted as oral presentation***